The Distribution of Wave Heights and Periods for Seas with Unimodal and Bimodal Power Density Spectra

by

Matthew Michael Sharpe

B.S., Electrical Engineering
United States Naval Academy (1982)

Submitted in partial fulfillment of the
requirements for the degree of

Ocean Engineer

at the

MASSACHUSETTS INSTITUTE OF TECHNOLOGY

and the

WOODS HOLE OCEANOGRAPHIC INSTITUTION

September 1990

Signature of Author .....
Joint Program In Oceanographic Engineering
Massachusetts Institute of Technology
Woods Hole Oceanographic Institution
10 August 1990

Certified by .....
Dr. Hans C. Graber
Assistant Scientist, Woods Hole Oceanographic Institution
Thesis Supervisor

Certified by .....
Dr. Ole S. Madsen
Professor of Civil Engineering, Massachusetts Institute of Technology
Thesis Supervisor

Certified by .....
Dr. Henrik Schmidt
Associate Professor of Ocean Engineering, Massachusetts Institute of Technology
Thesis Reader

Accepted by .....
W. Kendall Melville
Chairman, Joint Committee for Oceanographic Engineering
Massachusetts Institute of Technology / Woods Hole Oceanographic Institution

The Distribution of Wave Heights and Periods for Seas with Unimodal and Bimodal Power Density Spectra

by

Matthew Michael Sharpe

Submitted to the Massachusetts Institute of Technology/
Woods Hole Oceanographic Institution
Joint Program In Oceanographic Engineering
on 10 August 1990, in partial fulfillment of the
requirements for the degree of
Ocean Engineer

Abstract

Observed distributions of wave heights and periods taken from one year of surface wave monitoring near Martha's Vineyard are compared to distributions based on narrow-band theory. The joint distributions of wave heights and periods and the marginal height distributions are examined. The observed significant wave heights and the heights and periods of the extreme waves are also studied.

Seas are classified by the shapes of their power density spectra. Spectra with a single peak are designated as unimodal and spectra with two peaks as bimodal. Seas are further classified by spectral width, a function of the three lowest spectral moments.

The joint distributions of wave heights and periods from seas with narrow spectral widths take the general shape predicted by narrow-band theory and the statistics of extreme waves for these seas are well described. As spectral width increases, agreement between the theoretical and observed distributions diminishes and the significant wave heights and statistics of extreme waves show increasing variability. Bimodal seas with wide-banded spectra are found to have larger significant and extreme wave heights and shorter extreme wave periods than unimodal seas of the same width.

Thesis Supervisor: Dr. Hans C. Graber
Assistant Scientist, Woods Hole Oceanographic Institution

Thesis Supervisor: Dr. Ole S. Madsen
Professor of Civil Engineering, Massachusetts Institute of Technology

Acknowledgements

I dedicate this thesis to my wife, Carole, and baby girl, Lauren. Their love and support have been invaluable.

I am indebted to my thesis advisors, Dr. Hans Graber of WHOI and Prof. Ole Madsen of MIT, for their instruction and guidance, and will always remember their standards of academic and scientific excellence.

I also thank Prof. Paul Sclavounos of MIT for his valuable comments and suggestions.

Maxine Jones and Mike Caruso, fine programmers and system administrators at WHOI, provided much appreciated training in UNIX and the operation of a Sun workstation.

I thank the U. S. Navy for allowing me to pursue this course of instruction in the MIT/WHOI Joint Program in Oceanographic Engineering.

Finally, I thank God for a life filled with academic, professional, and spiritual challenges.

Contents

List of Figures

List of Tables

Chapter 1

Objectives

The relationship between a sea's energy spectrum and the joint distribution of wave heights and periods is of significant engineering interest. This relationship is not well understood for most spectral shapes.

The sea state is often described in the frequency domain by an energy spectrum. Much wave hindcasting and forecasting is carried out in this domain (Forristall 1978). Design engineers are more interested in a probability domain description of the sea surface.

A formulation of the joint distribution of wave heights and periods expressed as a function of the power density spectrum (or selected spectral moments) is needed. This function, and other distributions derived from it, provide the engineer with information about the wave heights, periods and wave orbital velocities which may be encountered by a ship or structure.

Developing a joint distribution valid for all spectral shapes is very difficult. Longuet-Higgins (1975,1983) applies to the ocean environment the theory of Gaussian noise studied by Rice (1944,1945). He proposes a joint distribution of wave heights and periods valid for seas with spectra of narrow bandwidth.

Woods Hole Oceanographic Institution's Telemetry Project operated a Waverider buoy southwest of Martha's Vineyard during 1987–1988. The time series and power density spectra from this project are used here to check the agreement between the wave height and period distribution given by narrow-band theory and those observed at sea. Particular attention is paid to observed values of significant wave height, and height and period of

the extreme wave during each 20 minute monitoring interval.

Seas are often assumed to have spectra with single peaks. The Martha's Vineyard Buoy data set provided many spectra with two distinct peaks. During analysis, two spectral types, identified as unimodal and bimodal, are segregated to determine how their height and period distributions differ.

In the work which follows, a progressive wave of permanent, sinusoidal form is shown to solve the linearized equations of motion. Many sinusoidal wave trains of independent amplitudes and phases are then superimposed. When the spectrum of the resulting process is assumed to be narrow-banded, the theoretical joint distribution of wave heights and periods is developed.

The joint distribution and other distributions derived from it are compared with wave heights and periods observed by the Waverider buoy. The characteristics of unimodal and bimodal seas are noted. A possible application of the result is presented.

Chapter 2

Theoretical Height and Period Distributions

2.1 Linear Theory for Periodic Waves

Study of wind waves requires an understanding of the allowable profiles of progressive waves on the sea surface. The basic equations of motion are exceedingly difficult to solve when applied to the ocean environment. Certain simplifications can be made to linearize the governing equations and their boundary conditions. The resulting system may be solved in closed form and produces a plane, progressive wave with a sinusoidal profile. This derivation requires the following assumptions

- Sea water is an incompressible and inviscid fluid.
- Flows are irrotational.
- All forces are conservative.
- Waves are of constant period.
- Depth is constant.
- The problem is two dimensional.

The conditions listed above may seem unrealistic and one might discount the utility of the resulting linear wave theory. Despite its approximate nature, linear theory agrees well with observations of actual waves. Linearity also allows for superposition, so simple sinusoidal waves may be combined to yield complex sea surface profiles. One must remain mindful of linear theory's approximations and the conditions under which they are valid.

This derivation proceeds in the following sequence:

- Identification of governing equations.
- Specification of boundary conditions.
- System linearization.
- Solution for the surface profile.

This follows closely the treatment of basic wave theory given in the MIT graduate course "Introduction to Coastal Engineering" taught by Prof. Ole S. Madsen.

2.1.1 Conservation of Mass and Momentum

Mass conservation is represented by

$$\frac{D\rho}{Dt} + \rho(\nabla \cdot \mathbf{q}) = 0 \tag{2.1}$$

where

$$\frac{D\rho}{Dt} \equiv \frac{\partial \rho}{\partial t} + \mathbf{q} \cdot \nabla \rho$$

is the material or total derivative, and

$$\nabla \equiv (\frac{\partial}{\partial x}, \frac{\partial}{\partial y}, \frac{\partial}{\partial z})$$

is the divergence operator. Mass conservation simplifies to

$$\nabla \cdot \mathbf{q} = 0 \tag{2.2}$$

under the assumption that the fluid is incompressible.

Newton's second law requires that momentum be conserved when viewed in an inertial frame of reference. When a coordinate system is fixed to the Earth's surface, Coriolis

correction terms must be used to account for angular acceleration of the non-inertial frame. The wind seas considered here have periodic motions with periods of less than one minute. For these periods, the Coriolis terms are small and may be neglected. Momentum conservation becomes

$$\rho\frac{D\mathbf{q}}{Dt} = -\nabla p - \rho g\hat{\mathbf{k}} + \text{“viscous stresses”} \tag{2.3}$$

with “viscous stresses” including both viscous and turbulent effects. Viscous stresses will be neglected in the present problem where they are important only in thin surface and bottom boundary layers. This gives Euler's equation

$$\rho\frac{D\mathbf{q}}{Dt} = -\nabla p - \rho g\hat{\mathbf{k}} \tag{2.4}$$

a simplification of conservation of momentum.

Introduction of a velocity potential, ϕ, will simplify obtaining a solution. The velocity potential and velocity are related by

$$\nabla\phi = \mathbf{q} \tag{2.5}$$

This reduces three unknowns, the components of $\mathbf{q}$, to one scalar. This simplification also reduces the number of boundary conditions that must (or may) be satisfied. In particular, the flow is restricted to be irrotational. As a result, it is not possible to enforce a no-slip condition at the solid boundaries. This restriction is consistent with the neglect of viscous stresses in the boundary layers. Introducing the velocity potential into mass conservation, (2.2) gives the Laplace equation

$$\nabla\cdot\mathbf{q} = \nabla^2\phi = 0 \tag{2.6}$$

where

$$\nabla^2 \equiv \left(\frac{\partial^2}{\partial x^2} + \frac{\partial^2}{\partial y^2} + \frac{\partial^2}{\partial z^2}\right) \tag{2.7}$$

is the Laplacian operator.

Expressing Euler's equation in terms of the velocity potential gives the generalized Bernoulli equation

$$\frac{\partial\phi}{\partial t} + \frac{1}{2}(\nabla\phi)^2 + \frac{p}{\rho} + gz = f(t) \tag{2.8}$$

with $f(t)$ an arbitrary time function. This time function may be incorporated into the velocity potential without affecting the resulting velocity field $\mathbf{q}$. After this manipulation, the generalized Bernoulli equation becomes

$$\frac{\partial \phi}{\partial t} + \frac{1}{2}(\nabla \phi)^2 + \frac{p}{\rho} + gz = C \tag{2.9}$$

where C is a constant and may be set equal to zero by selecting the appropriate datum from which to measure z.

The problem has been reduced to two equations, (2.6) and (2.9), in two scalar unknowns, ϕ and p. The Laplace equation with boundary conditions describes the kinematics of the problem and is solved for the velocity potential, ϕ. The dynamics of the system are then satisfied by selecting the pressure field which solves the Bernoulli equation for the ϕ found above.

2.1.2 Bottom and Surface Boundary Conditions

The sea bottom is considered to be a fixed, impenetrable boundary. The general mathematical expression for a surface

$$S_b(x, y, z)|_{z=-h} = 0 \tag{2.10}$$

may describe the bottom. Fluid particles in contact with the boundary will remain in contact with it. They move along the bottom but may have no component of velocity normal to it. Equation (2.10) may be rewritten

$$S_b(x_p(t), y_p(t), z_p(t))|_{z=-h} = 0 \tag{2.11}$$

where the fluid particle's coordinates, $x_p(t), y_p(t), z_p(t)$, always lie on the bottom. The function S_b thus behaves as a property which is conserved by water in contact with the bottom. Expressing this conservation as

$$\frac{DS_b}{Dt} = \frac{\partial S_b}{\partial t} + \mathbf{q} \cdot \nabla S_b = 0 \tag{2.12}$$

and noting that $\frac{\partial S_b}{\partial t} = 0$ for a fixed surface, the result

$$\mathbf{q} \cdot \nabla S_b = 0 \Rightarrow \frac{\partial \phi}{\partial n} = 0 \tag{2.13}$$

is obtained, formalizing the earlier restriction on normal velocities. Tangential velocities are unrestricted and there is no enforcement of a no-slip condition.

The sea surface may be defined by

$$z = \eta(x, y, t) \tag{2.14}$$

where η has a time dependence to allow the surface to move. As at the bottom boundary, the surface is expressed as a function of the three spatial coordinates,

$$S_s = \eta(x, y, t) - z = 0 \tag{2.15}$$

but there is now a temporal dependence as well. Assuming that fluid elements on the surface remain on the surface, conservation of S for these elements gives the kinematic free surface boundary condition

$$\frac{DS_s}{Dt} = \frac{\partial S_s}{\partial t} + \mathbf{q} \cdot \nabla S_s = 0 \tag{2.16}$$

$$\frac{\partial \eta}{\partial t} + \frac{\partial \phi}{\partial x}\frac{\partial \eta}{\partial x} + \frac{\partial \phi}{\partial y}\frac{\partial \eta}{\partial y} - \frac{\partial \phi}{\partial z} = 0 \tag{2.17}$$

evaluated at $z = \eta(x, y, t)$, the free surface. A second boundary condition is obtained by coupling the kinematics and dynamics of the problem. If the effect of surface tension on fluid pressure is ignored, the pressure on a fluid element just below the surface is atmospheric pressure, p_a, and the Bernoulli equation becomes the dynamic free surface boundary condition

$$\frac{\partial \phi}{\partial t} + \frac{1}{2}(\nabla \phi)^2 + g\eta = 0 \tag{2.18}$$

evaluated at $z = \eta(x, y, t)$. Wind waves of interest here have periods longer than two seconds and lengths greater than six meters. These waves are sufficiently long to justify neglecting surface tension. A study of gravity-capillary waves would need to consider surface tension effects.

2.1.3 Linearizing the Boundary Conditions

The two free surface boundary conditions are non-linear. They are directly non-linear in ϕ and η due to terms of the form $\frac{\partial \phi}{\partial x_i}\frac{\partial \eta}{\partial x_i}$ and $\frac{\partial \phi}{\partial x_i}\frac{\partial \phi}{\partial x_i}$. The boundary conditions are enforced at $z = \eta(x, y, t)$ instead of $z = 0$, producing an additional non-linearity.

Provided the wave height is small compared to the wave length and the water depth, the non-linearities will be small compared to the linear effects. If the wave height is of order H, wave length is of order L, and water depth is of order h, it can be shown that the non-linear terms are small compared to the linear terms in both boundary conditions if the wave steepness is small, i.e., $H/L << 1$. The non-linearities resulting from applying the boundary conditions at $z = \eta$ are removed by expanding the velocity potential in a Taylor series about $z = 0$. If the wave height is small compared to the water depth, $H << h$, then second and higher order terms in the expansion may be neglected. Therefore, the boundary conditions may be applied at $z = 0$.

The linearized free surface boundary conditions become

$$\frac{\partial \eta}{\partial t} - \frac{\partial \phi}{\partial z} = 0 \tag{2.19}$$

$$\frac{\partial \phi}{\partial t} + g\eta = 0 \tag{2.20}$$

at $z = 0$. Solving (2.20) for η

$$\eta = -\frac{1}{g}\frac{\partial \phi}{\partial t} \qquad \text{at } z = 0 \tag{2.21}$$

and substituting the result into (2.19) gives a boundary condition in the velocity potential only. The linear problem becomes

$$\nabla^2 \phi = 0 \tag{2.22}$$

$$\frac{\partial \phi}{\partial z} = 0 \qquad \text{at } z = -h \tag{2.23}$$

$$\frac{\partial^2 \phi}{\partial t^2} + g\frac{\partial \phi}{\partial z} = 0 \qquad \text{at } z = 0 \tag{2.24}$$

This system is solved for the velocity potential, then η is found from (2.21), and the pressure is given by

$$p + \rho g z = -\rho \frac{\partial \phi}{\partial t} \tag{2.25}$$

the linearized Bernoulli equation.

2.1.4 Finding the Surface Profile

A solution giving the surface profile for a progressive periodic wave of permanent form may be found using separation of variables. For a wave moving in the positive x direction

with phase speed c, the velocity potential may be expressed as

$$\phi = Z(z)F(\theta) \tag{2.26}$$

where

$$\theta = x - ct \tag{2.27}$$

Substituting this into (2.6) gives

$$\frac{Z''(z)}{Z(z)} = \frac{-F''(\theta)}{F(\theta)} = k^2 \tag{2.28}$$

where k is an arbitrary separation constant.

This may be rearranged into two ordinary differential equations

$$\frac{d^2Z}{dz^2} - k^2 Z = 0 \tag{2.29}$$

$$\frac{d^2F}{d\theta^2} + k^2 F = 0 \tag{2.30}$$

with general solutions

$$Z(z) = A_1 \exp^{kz} + A_2 \exp^{-kz} \tag{2.31}$$

and

$$F(\theta) = B_1 \cos k(x - ct) + B_2 \sin k(x - ct) = B_3 \sin(k(x - ct) + \delta) \tag{2.32}$$

where A_i and B_i are arbitrary constants and δ is an arbitrary phase angle. The bottom boundary condition, (2.13), reduces (2.31) to the form

$$Z = A_3 \cosh k(z + h) \tag{2.33}$$

and gives a resulting velocity potential of

$$\phi = A_3 B_3 \cosh k(z + h) \sin k(x - ct) \tag{2.34}$$

where the phase term δ has been eliminated by choosing an appropriate origin for x. The associated surface profile given by (2.21) is

$$\begin{aligned} \eta &= \frac{A_3 B_3 kc}{g} \cosh kh \cos k(x - ct) \\ &= a \cos(kx - \sigma t) \end{aligned} \tag{2.35}$$

a sinusoidal wave of amplitude $a = \frac{A_3 B_3 kc}{g} \cosh kh$ and radian frequency $\sigma = kc$ where the wavenumber, k, is the separation constant.

By introducing the velocity potential given by (2.34) in the free surface boundary condition, (2.24), a relationship among wavenumber, radian frequency and water depth, known as the dispersion relationship,

$$\sigma^2 = kg \tanh kh \tag{2.36}$$

is obtained.

2.1.5 Orbital Velocities

The velocity potential for a linear, progressive wave may be expressed as

$$\phi = \frac{ag}{\sigma} \frac{\cosh k(z+h)}{\cosh kh} \sin(kx - \sigma t) \tag{2.37}$$

where a is the wave amplitude. The horizontal component of velocity is found from the potential

$$\mathbf{u} = \frac{\partial \phi}{\partial x} = \frac{agk}{\sigma} \frac{\cosh k(z+h)}{\cosh kh} \cos(kx - \sigma t) \tag{2.38}$$

Using the dispersion relationship, (2.38) becomes

$$\mathbf{u} = a\sigma \frac{\cosh k(z+h)}{\sinh kh} \cos(kx - \sigma t) \tag{2.39}$$

For waves in deep water, this reduces to

$$\mathbf{u} = a\sigma \cos(kx - \sigma t) \tag{2.40}$$

for the near-surface horizontal velocities. Similarly, the near-surface vertical velocities are

$$\mathbf{w} = a\sigma \sin(kx - \sigma t) \tag{2.41}$$

The horizontal and vertical velocities have a maximum value of $a\sigma = \frac{H\pi}{\tau}$ where $H = 2a$ is the crest-to-trough height and τ is the wave period. Knowing the wave height and period is sufficient to determine the maximum horizontal and vertical velocities.

2.2 Development of Wave Height and Period Distributions for Narrow-Band Seas

The work of the previous section described that a progressive wave of permanent, sinusoidal form is a solution to the linearized equations of motion. This section will build on this result by superimposing many sinusoidal wave trains of independent amplitudes and phases. The resulting sea surface profile will then be represented as a carrier wave of fixed frequency modulated by a complex wave envelope function. The behavior of the envelope's amplitude and phase will be analyzed to find the statistics of wave heights and periods.

2.2.1 Superposition of Sinusoidal Wave Trains

Equation (2.35) showed that a sinusoidal wave

$$\eta(t) = a\cos k(x - ct) = a\cos(kx - \sigma t) \tag{2.42}$$

with radian frequency $\sigma = kc$ solves the linearized equations of motion. A real sea surface may be represented as the sum of a large number of simple sinusoids with independent amplitudes and phases. This is shown graphically by Figure 2-1. Such a superposition is valid only for small amplitude waves when the linearizing assumptions of Section 2.1.4 hold. It is not valid for waves approaching maximum height nor for waves of moderate height entering shallow water when amplitudes and phases of harmonics are correlated with those of the fundamental frequencies. This situation complicates the analysis and will not be considered here.

The time history of sea surface heights viewed at a fixed location and expressed as a combination of sinusoids may be written as

$$\eta(t) = \sum_n C_n \cos(\sigma_n t + \delta_n) \tag{2.43}$$

where the frequencies σ_n are densely spaced in the interval $(0, \infty)$. Amplitudes, C_n, are real independently distributed random variables with finite variances. Phases, δ_n, are independent and uniformly distributed in the interval $(0, 2\pi)$. This sea surface height is

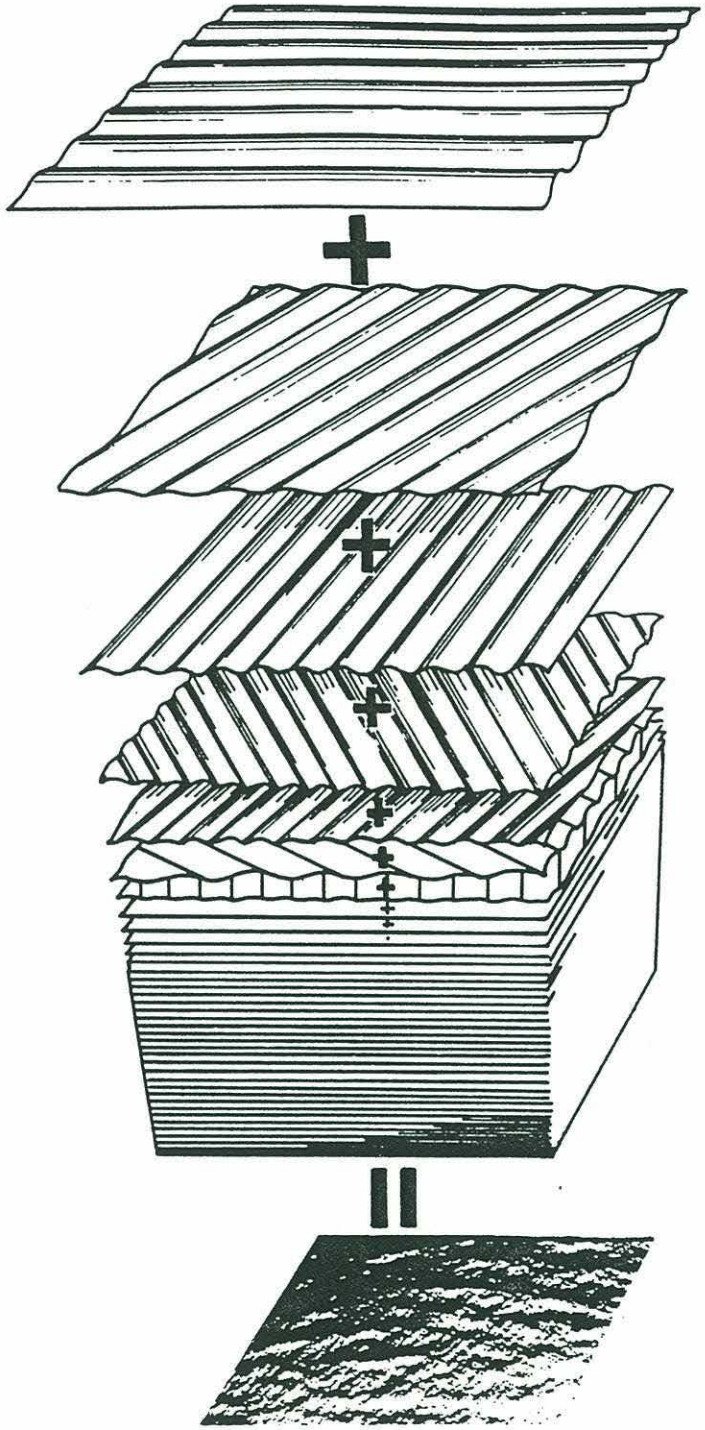

Figure 2-1: Superposition of long-crested, sinusoidal wave trains gives a random sea surface. From Pierson, Neuman, and James (1958).

the sum of a large number of zero-mean independent random variables of finite variance. Analysis based on a central limit theorem shows the probability distribution of sea surface heights thus obtained is normally distributed with zero mean.

Another representation of sea surface height is

$$\eta(t) = \Re\{\sum_n C_n \exp[i(\sigma_n t + \delta_n)]\} \tag{2.44}$$

where $\Re$ symbolizes the real part of a complex quantity. Each Fourier series coefficient, C_n, shows the energy present at its associated frequency, σ_n. These coefficients are related to the energy spectrum, $S(\sigma)$,

$$S(\sigma)d\sigma = \sum_n \frac{1}{2} C_n^2 \tag{2.45}$$

where the summation includes only those values of n such that the frequencies corresponding to C_n fall in the interval $(\sigma, \sigma + d\sigma)$. The product on the left side of the equation and the summation on the right are two ways of expressing the energy in the same narrow band of wave frequencies.

2.2.2 Carrier-Envelope Representation

In order to express $\eta(t)$ as a modulated carrier wave, it is useful to define a mean frequency, $\bar{\sigma}$, in terms of the moments of $S(\sigma)$. The spectral moments, m_r, are defined as

$$m_r = \int_0^\infty \sigma^r S(\sigma) d\sigma \tag{2.46}$$

or as central moments

$$\begin{aligned} \mu_r &= \int_0^\infty (\sigma - \bar{\sigma})^r S(\sigma) d\sigma \\ &= \sum_{n=0}^\infty \frac{1}{2} (\sigma_n - \bar{\sigma})^r c_n^2 \end{aligned} \tag{2.47}$$

When the mean frequency is defined by

$$\bar{\sigma} = \frac{m_1}{m_0} \tag{2.48}$$

then the following relationships hold

$$\mu_0 = m_0 \tag{2.49}$$

$$\mu_1 = 0 \tag{2.50}$$

$$\mu_2 = \frac{m_0 m_2 - m_1^2}{m_0} \tag{2.51}$$

Some authors prefer to call $\bar{\sigma}$ the centroid frequency (Nath and Yeh 1987) because it is defined in terms of the moments of an energy spectrum instead of a probability distribution and is not a mean in the statistical sense. Both terms refer to the same quantity and mean frequency, the more commonly used of the two, will be used here.

Equation (2.44) may be expressed in terms of the mean frequency and a deviation from the mean frequency

$$\eta(t) = \Re\{\sum_n c_n \exp[i(\sigma_n' t + \delta_n)] \exp(i\bar{\sigma}t)\} \tag{2.52}$$

where

$$\sigma_n' \equiv \sigma_n - \bar{\sigma}$$

is the frequency deviation from its mean value. If the complex envelope is defined as

$$\rho e^{i\phi} = \sum_n c_n \exp[i(\sigma_n' t + \delta_n)] \tag{2.53}$$

then

$$\eta(t) = \Re\{ \underbrace{\rho e^{i\phi}}_{envelope} \underbrace{\exp(i\bar{\sigma}t)}_{carrier}\} \tag{2.54}$$

is a carrier of fixed frequency modulated by a complex wave envelope of amplitude ρ and phase ϕ. The amplitude and phase are time-varying random variables and are functions of c_n and δ_n.

2.2.3 Statistical Behavior of the Complex Envelope

The joint distributions of ρ and $\dot{\phi}$ will be a key to understanding the distribution of wave heights and periods. Following the approach used by Longuet-Higgins (1975) and Rice (1944,1945), the envelope

$$\rho e^{i\phi} = \rho \cos\phi + i\rho \sin\phi \tag{2.55}$$

may be expressed as

$$\rho e^{i\phi} = \xi_1 + i\xi_2 \tag{2.56}$$

where

$$\xi_1 = \sum_n c_n \cos(\sigma_n' t + \delta_n) \tag{2.57}$$

$$\xi_2 = \sum_n c_n \sin(\sigma_n' t + \delta_n) \tag{2.58}$$

Since the time derivative of phase, $\dot{\phi}$, is also of interest, define the time derivatives of ξ_1 and ξ_2 as

$$\begin{aligned} \xi_3 &= \dot{\xi}_1 \\ &= -\sum \sigma'_n c_n \sin(\sigma'_n t + \delta_n) \qquad (2.59) \\ \xi_4 &= \dot{\xi}_2 \\ &= \sum \sigma'_n c_n \cos(\sigma'_n t + \delta_n) \qquad (2.60) \end{aligned}$$

The four variables, ξ_i, are found through application of a central limit theorem to be normally distributed random variables. Their joint distribution may be completely described by their means and correlation matrix. The mean of ξ_1 is

$$\overline{\xi_1} = \overline{\sum_n c_n \cos(\sigma'_n t + \delta_n)} \qquad (2.61)$$

where the overline represents an ensemble average. Equation (2.61) may be written as

$$\overline{\xi_1} = \sum_n \overline{c_n} \overline{\cos(\sigma'_n t + \delta_n)} \qquad (2.62)$$

because c_n and δ_n are independent. The cosine term has phase uniformly distributed in the interval $(0, 2\pi)$ and therefore has zero mean. This gives

$$\overline{\xi_1} = 0 \qquad (2.63)$$

Through identical arguments one finds

$$\overline{\xi_1} = \overline{\xi_2} = \overline{\xi_3} = \overline{\xi_4} = 0 \qquad (2.64)$$

The correlation matrix

$$\mathbf{R} = \begin{pmatrix} \overline{\xi_1\xi_1} & \overline{\xi_1\xi_2} & \overline{\xi_1\xi_3} & \overline{\xi_1\xi_4} \\ \overline{\xi_2\xi_1} & \overline{\xi_2\xi_2} & \overline{\xi_2\xi_3} & \overline{\xi_2\xi_4} \\ \overline{\xi_3\xi_1} & \overline{\xi_3\xi_2} & \overline{\xi_3\xi_3} & \overline{\xi_3\xi_4} \\ \overline{\xi_4\xi_1} & \overline{\xi_4\xi_2} & \overline{\xi_4\xi_3} & \overline{\xi_4\xi_4} \end{pmatrix} \qquad (2.65)$$

is simplified by the orthogonality of sinusoids. Terms of the form

$$\overline{\cos(\sigma'_n t + \delta_n) \sin(\sigma'_m t + \delta_m)} \qquad (2.66)$$

vanish for all m, n. Terms of the form

$$\overline{\cos(\sigma_n' t + \delta_n)\cos(\sigma_m' t + \delta_m)} \tag{2.67}$$

or

$$\overline{\sin(\sigma_n' t + \delta_n)\sin(\sigma_m' t + \delta_m)} \tag{2.68}$$

vanish for $m \neq n$. This reduces the correlation matrix to

$$\mathbf{R} = \begin{pmatrix} \overline{\xi_1\xi_1} & 0 & 0 & \overline{\xi_1\xi_4} \\ 0 & \overline{\xi_2\xi_2} & \overline{\xi_2\xi_3} & 0 \\ 0 & \overline{\xi_3\xi_2} & \overline{\xi_3\xi_3} & 0 \\ \overline{\xi_4\xi_1} & 0 & 0 & \overline{\xi_4\xi_4} \end{pmatrix} \tag{2.69}$$

Solving for $\overline{\xi_1\xi_1}$

$$\overline{\xi_1\xi_1} = \overline{\sum_n \sum_n c_n c_m \cos(\sigma_n' t + \delta_n)\cos(\sigma_m' t + \delta_m)} \tag{2.70}$$

simplifies to

$$\overline{\xi_1\xi_1} = \sum_n \overline{c_n^2 \cos^2(\sigma_n' t + \delta_n)} \tag{2.71}$$

using independence of the coefficients and phases and the orthogonality expressed in (2.67). Since

$$\overline{\cos^2(\sigma_n' t + \delta_n)} = \frac{1}{2} \tag{2.72}$$

using (2.47) gives

$$\overline{\xi_1\xi_1} = \sum_n \frac{1}{2} c_n^2 = \mu_0 \tag{2.73}$$

The same procedure gives

$$\overline{\xi_2\xi_2} = \sum_n \frac{1}{2} c_n^2 = \mu_0 \tag{2.74}$$

The solutions for $\overline{\xi_3\xi_3}$ and $\overline{\xi_4\xi_4}$ are similar and show

$$\begin{aligned} \overline{\xi_3\xi_3} &= \overline{\sum_n \sum_m \sigma_n' \sigma_m' c_n c_m \sin(\sigma_n' t + \delta_n)\sin(\sigma_m' t + \delta_m)} \\ &= \overline{\sum_n \sigma_n'^2 c_n^2 \sin^2(\sigma_n' t + \delta_n)} \\ &= \sum_n \sigma_n'^2 \frac{1}{2} \overline{c_n^2} \\ &= \mu_2 \end{aligned} \tag{2.75}$$

The four non-zero off-diagonal elements of $\mathbf{R}$ are found using a method similar to that which follows for $\overline{\xi_1\xi_4}$

$$\begin{aligned}
\overline{\xi_1\xi_4} &= \overline{\sum_n \sum_m \sigma'_m c_n c_m \cos(\sigma'_n t + \delta_n)\cos(\sigma'_m t + \delta_m)} \\
&= \overline{\sum_n \sigma'_n c_n^2 \cos^2(\sigma'_n t + \delta_n)} \\
&= \sum_n \sigma'_n \frac{1}{2}\overline{c_n^2} \\
&= \mu_1
\end{aligned} \tag{2.76}$$

The resulting correlation matrix

$$\mathbf{R} = \begin{pmatrix} \mu_0 & 0 & 0 & \mu_1 \\ 0 & \mu_0 & -\mu_1 & 0 \\ 0 & -\mu_1 & \mu_2 & 0 \\ \mu_1 & 0 & 0 & \mu_2 \end{pmatrix} \tag{2.77}$$

simplifies to a diagonal matrix

$$\mathbf{R} = \begin{pmatrix} \mu_0 & 0 & 0 & 0 \\ 0 & \mu_0 & 0 & 0 \\ 0 & 0 & \mu_2 & 0 \\ 0 & 0 & 0 & \mu_2 \end{pmatrix} \tag{2.78}$$

because $\mu_1 = 0$ with $\bar{\sigma}$ as defined in (2.48). Therefore, $\xi_1, \xi_2, \xi_3, \xi_4$ are zero-mean, uncorrelated Gaussian random variables and are described by the following multivariate normal distribution

$$p(\xi_1, \xi_2, \xi_3, \xi_4) = \frac{1}{(2\pi)^2 \mu_0 \mu_2} \exp[-\frac{\xi_1^2 + \xi_2^2}{2\mu_0}] \exp[-\frac{\xi_3^2 + \xi_4^2}{2\mu_2}] \tag{2.79}$$

The transformation

$$p(\rho, \phi, \dot{\rho}, \dot{\phi}) = \frac{\partial(\xi_1, \xi_2, \xi_3, \xi_4)}{\partial(\rho, \phi, \dot{\rho}, \dot{\phi})} p(\xi_1, \xi_2, \xi_3, \xi_4) \tag{2.80}$$

gives the joint density of the envelope amplitude, phase, and their time derivatives. Since

$$\xi_1 = \rho \cos\phi \tag{2.81}$$

$$\xi_2 = \rho \sin\phi \tag{2.82}$$

$$\xi_3 = \dot{\rho}\cos\phi - \dot{\phi}\rho\sin\phi \tag{2.83}$$

$$\xi_4 = \dot{\rho}\sin\phi + \dot{\phi}\rho\cos\phi \tag{2.84}$$

then

$$\frac{\partial(\xi_1,\xi_2,\xi_3,\xi_4)}{\partial(\rho,\phi,\dot{\rho},\dot{\phi})} = \rho^2 \tag{2.85}$$

Making the substitutions given by

$$\begin{aligned} \xi_1^2+\xi_2^2 &= \rho^2(\cos^2\phi+\sin^2\phi) \\ &= \rho^2 \qquad (2.86) \\ \xi_3^2+\xi_4^2 &= (\dot{\rho}^2+\rho^2\dot{\phi}^2)(\cos^2\phi+\sin^2\phi) \\ &\quad +(\dot{\rho}\rho\dot{\phi}-\dot{\rho}\rho\dot{\phi})\cos\phi\sin\phi \\ &= \dot{\rho}^2+\rho^2\dot{\phi}^2 \qquad (2.87) \end{aligned}$$

gives the density

$$p(\rho,\phi,\dot{\rho},\dot{\phi}) = \frac{\rho^2}{(2\pi)^2\mu_0\mu_2}\exp(-\frac{\rho^2}{2\mu_0})\exp(-\frac{\dot{\rho}^2+\rho^2\dot{\phi}^2}{2\mu_2}). \tag{2.88}$$

Integrating with respect to $\dot{\rho}$ over $(-\infty,\infty)$ and with respect to ϕ over $(0,2\pi)$, the resulting density for $\rho,\dot{\phi}$ is

$$p(\rho,\dot{\phi}) = \frac{\rho^2}{(2\pi)^{\frac{1}{2}}(\mu_0^2\mu_2)^{\frac{1}{2}}}\exp(-\frac{\rho^2}{2\mu_0})\exp(-\frac{\rho^2\dot{\phi}^2}{2\mu_2}) \tag{2.89}$$

or

$$p(\rho,\dot{\phi}) = \frac{\rho^2}{(2\pi)^{\frac{1}{2}}[m_0(m_0m_2-m_1^2)]^{\frac{1}{2}}}\exp(-\frac{\rho^2}{2m_0})\exp(-\frac{\rho^2\dot{\phi}^2m_0}{2(m_0m_2-m_1^2)}) \tag{2.90}$$

It is worthwhile to review the assumptions made up to this point. The hydrodynamic problem was linearized based on a set of assumptions valid only for small amplitude waves in deep water. This linearization allows for superposition. The wave spectrum is assumed to have energy at all frequencies with independent coefficients and phases for the different frequencies. This assumption is also restricted to small amplitude waves. No assumption has been made about the amount of energy at the various frequencies, i.e., the spectral shape. In particular, no narrow-band assumption has yet been needed.

The probability density given by (2.90) is a function of the second and lower moments of the energy spectrum. Would it be necessary to consider a distribution involving higher derivatives of ρ and ϕ, the density would be a function of higher order spectral moments. Two moments are needed for each additional time derivative. This is undesirable when

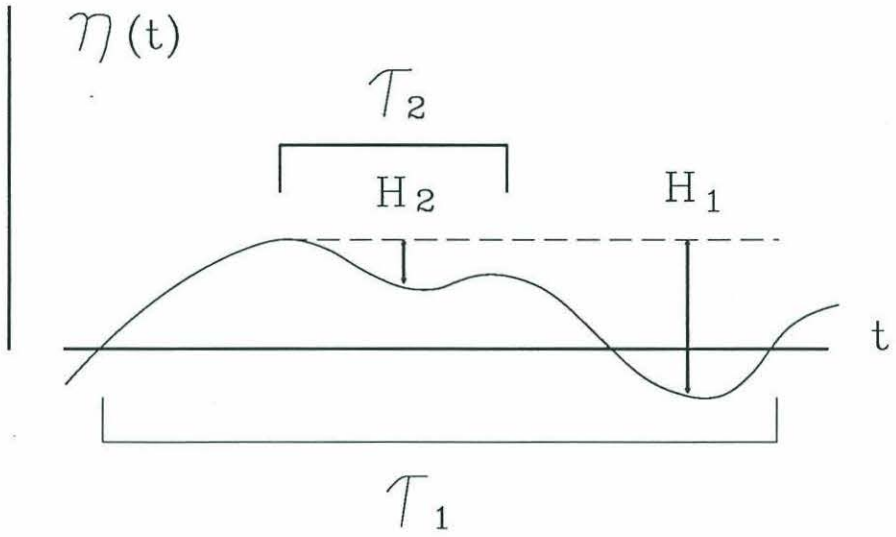

Figure 2-2: Definitions of wave height, H, and period, τ. H_1, and τ_1 are based on zero-up-crossings of $\eta(t)$. H_2, and τ_2 use crests to define the waves.

the resulting theory is to be applied to real data. The fourth moment, m_4, may depend critically on the behavior of the spectrum at high frequencies (Longuet-Higgins 1983). These frequencies are also likely to contain considerable noise (Nath and Yeh 1987).

2.2.4 Wave Height and Period Defined

There are two commonly used definitions for the wave heights and periods of a continuous function, $\eta(t)$. In the first, a wave is defined to extend from a time when $\eta(t)$ is increasing and crosses the mean level to the next time this happens. This time interval is called the zero-up-crossing period (τ_1 in Figure 2-2). The associated wave height, (H_1), is the difference between the maximum and minimum values of $\eta(t)$ in this interval. This is the definition to be used in the present work.

An alternate approach defines a wave as extending from one crest to the next (τ_2 in Figure 2-2). The wave height, H_2, may then be defined as the difference between a crest and its succeeding trough.

The zero-up-crossing period has been chosen because it is more appropriate for the

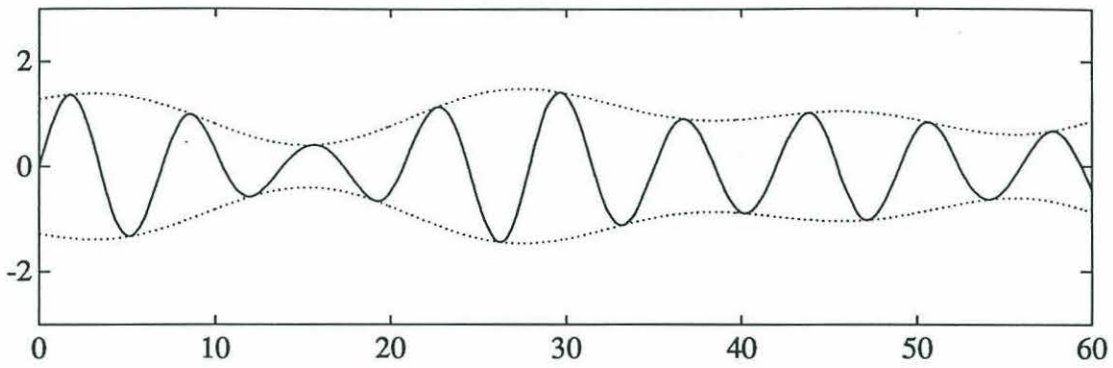

Figure 2-3: Narrow-band signal, $\eta(t)$, with its envelope function. The extrema of $\eta(t)$ lie nearly on the envelope.

distributions used here which depend on the second moment of the energy spectrum. The crest-to-crest definition may be more appropriate for distributions based on the fourth moment, m_4 (Longuet-Higgins 1983).

2.2.5 Finding the Wave Height and Period – The Narrow-Band Hypothesis

Equation 2.54 expressed the sea surface height as a modulated carrier wave

$$\eta(t) = \Re\{ \underbrace{\rho e^{i\phi}}_{envelope} \underbrace{\exp(i\bar{\sigma}t)}_{carrier}\} \tag{2.91}$$

If ϕ and ρ are slowly varying functions of time, then the maxima and minima of $\eta(t)$ lie nearly on the envelope function. There is one extremum for each maximum or minimum of the carrier. There are no additional extrema generated by rapid variation of the envelope. This is shown in Figure 2-3.

The definition of the envelope,

$$\rho e^{i\phi} = \sum_n c_n \exp[i(\sigma_n' t + \delta_n)] \tag{2.92}$$

$$\sigma_n' = \sigma_n - \bar{\sigma}$$

indicates ρ and ϕ will vary slowly when spectral energy is concentrated in a small band of frequencies near $\bar{\sigma}$, where σ_n' is small.

Under this assumption, wave height, H, is related simply to the magnitude of the envelope. With extrema lying nearly on the envelope, a wave amplitude, a, equals the magnitude of the envelope function, $a = \rho$. A wave height is twice the amplitude, or

$$H = 2a = 2\rho \tag{2.93}$$

and the probability densities of H and ρ differ only by a multiplicative constant.

The wave period, τ, is related to $\dot{\phi}$, the rate of change of the phase of the envelope. The total phase of $\eta(t)$,

$$\chi = \phi + \bar{\sigma}t \tag{2.94}$$

will be a strictly increasing function of time because ϕ varies slowly compared to $\bar{\sigma}t$. The rate of change of phase is

$$\dot{\chi} = \dot{\phi} + \bar{\sigma} \approx \bar{\sigma} \tag{2.95}$$

Zero-up-crossings of $\eta(t)$ will be spaced at intervals of 2π in χ. (The function, $\eta(t)$, will also go to zero if ρ vanishes but this is a statistically rare event.) The wave period is given by

$$\tau = \frac{2\pi}{\dot{\chi}} = \frac{2\pi}{\bar{\sigma} + \dot{\phi}} \tag{2.96}$$

It is useful to normalize the height and period. Write

$$R \equiv \frac{H}{(8m_0)^{\frac{1}{2}}} = \frac{\rho}{(2m_0)^{\frac{1}{2}}} \tag{2.97}$$

$$T \equiv \frac{\tau}{\bar{\tau}} = \frac{\bar{\sigma}}{\bar{\sigma} + \dot{\phi}} = \frac{m_1}{m_1 + m_0\dot{\phi}} \tag{2.98}$$

where

$$\bar{\tau} \equiv \frac{2\pi}{\bar{\sigma}} = \frac{2\pi m_0}{m_1} \tag{2.99}$$

These definitions allow the joint probability of the carrier amplitude and phase rate to be transformed to the joint density of wave height and period. The transformation follows

$$p(R,T) = p(\rho,\dot{\phi}) \left| \frac{\partial(\rho,\dot{\phi})}{\partial(R,T)} \right| \tag{2.100}$$

where

$$\left| \frac{\partial(\rho,\dot{\phi})}{\partial(R,T)} \right| = \begin{vmatrix} \sqrt{2m_0} & 0 \\ 0 & \frac{-m_1}{m_0 T^2} \end{vmatrix} = \sqrt{\frac{2}{m_0}} \frac{m_1}{T^2} \tag{2.101}$$

The resulting density is

$$p(R,T) = \frac{2}{\nu\sqrt{\pi}} \frac{R^2}{T^2} e^{-R^2[1+(1-1/T)^2/\nu^2]} \tag{2.102}$$

$$R \in (0, \infty)$$

$$T \in (-\infty, \infty)$$

where

$$\nu^2 \equiv \frac{m_0 m_2 - m_1^2}{m_1^2} \tag{2.103}$$

is a measure of the width of the energy spectrum. The distribution given by (2.102) above includes negative wave periods. This is not physically sensible and the narrow-band hypothesis restricts periods to be non-negative by requiring the phase of the envelope to increase monotonically. The probability density may be rescaled with a limited domain

$$p(R,T) = \frac{2}{\nu\sqrt{\pi}} \frac{R^2}{T^2} e^{-R^2[1+(1-1/T)^2/\nu^2]} L(\nu) \tag{2.104}$$

$$R \in (0, \infty)$$

$$T \in (0, \infty)$$

where $L(\nu)$ is a normalizing factor to correct the total probability to unity. Integration of (2.104) over its range shows

$$L(\nu) = \frac{2\sqrt{1+\nu^2}}{1+\sqrt{1+\nu^2}} \tag{2.105}$$

and $L(\nu) \approx 1$ for small values of ν. Longuet-Higgins (1983) defines a narrow spectrum as one for which $\nu^2 \leq 0.36$, or $\nu \leq 0.6$.

Contours of $p(R,T)/p_{max}$ for several values of ν are shown in Figure 2-4. Two features of the distributions are worthy of note. The highest waves are expected to be the most regular in period, with the conditional probability concentrated near $T = 1$. Also, the distribution is asymmetric in period which agrees with observation. Earlier work (Longuet-Higgins 1975) produced a distribution that used the same measure of spectral width but was symmetric in period and inconsistent with observed distributions. Cavanié proposed a distribution which was appropriately asymmetric but used a spectral width

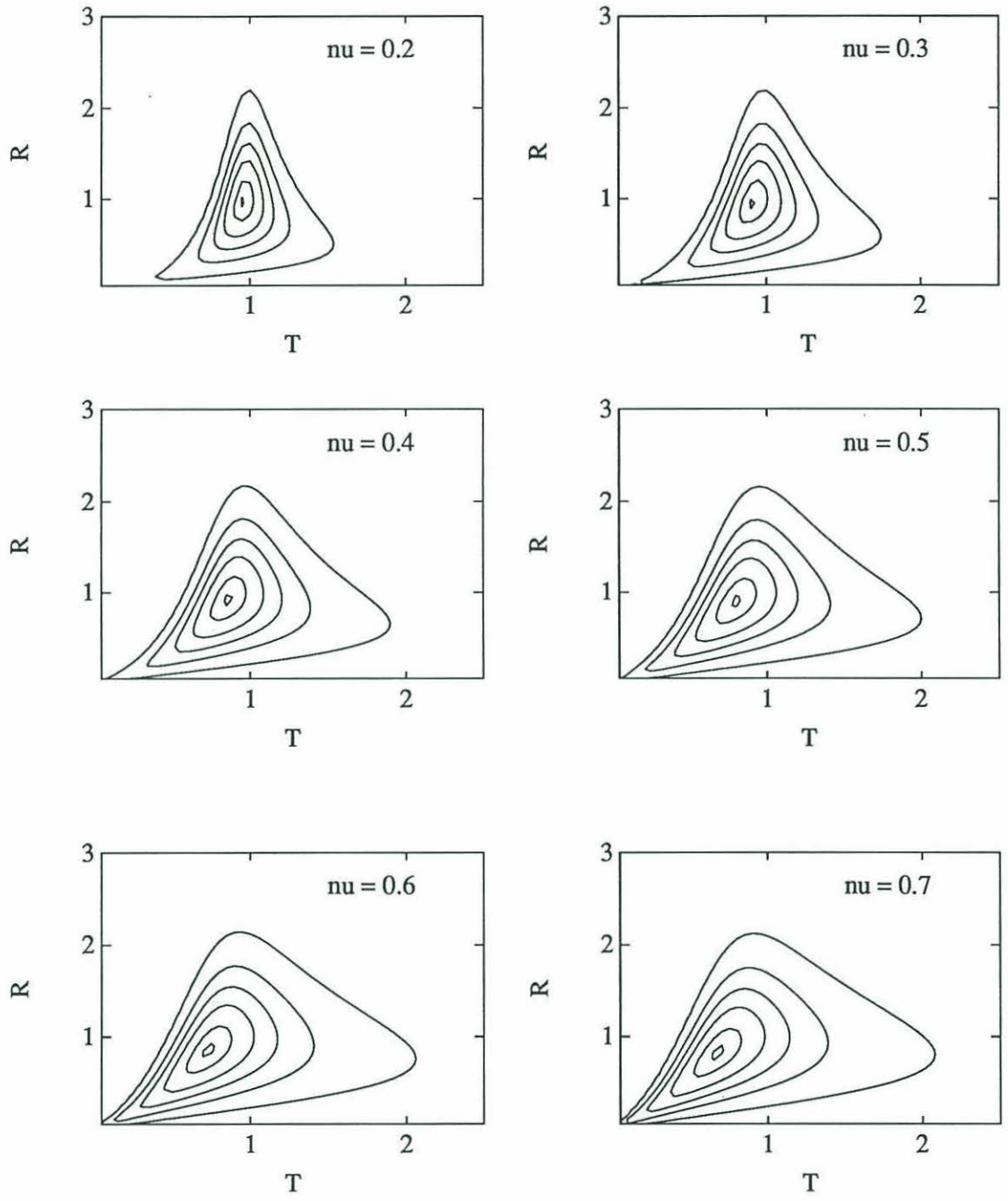

Figure 2-4: Contours of $p(R,T)/p_{max}$ for several spectral widths. Contours are shown for the values $(0.99, 0.9, 0.7, 0.5, 0.3, 0.1) \times p_{max}$ following Longuet-Higgins (1983).

parameter involving the fourth spectral moment, m_4. As discussed in Section 2.2.3, this is inconvenient when applied to real spectra.

Equation 2.104 provides a foundation from which to build the distributions which follow. These derived distributions, like (2.104), will be characterized by the single parameter, ν.

2.2.6 Marginal Density of Wave Heights

The marginal density of wave heights, $p(R)$, is found from $p(R,T)$ by integrating over all values of T in the interval $(0,\infty)$.

$$\begin{aligned} p(R) &= \int_0^\infty p(R,T)dT \\ &= \frac{2}{\nu\sqrt{\pi}} R^2 e^{-R^2} L(\nu) \int_0^\infty \frac{1}{T^2} e^{-R^2(1-1/T)^2/\nu^2} dT \end{aligned} \tag{2.106}$$

Making the substitution

$$\beta = \frac{R}{\nu}(1 - \frac{1}{T}) \tag{2.107}$$

gives the marginal density

$$p(R) = \underbrace{2Re^{-R^2}}_{Rayleigh} \underbrace{L(\nu)\frac{1}{\sqrt{\pi}} \int_{-\infty}^{R/\nu} e^{-\beta^2} d\beta}_{correction} \tag{2.108}$$

The wave height distribution is nearly Rayleigh but has a correction factor that depends on spectral width. The effect of this correction is to reduce the probability of small amplitude waves and increase the probability of waves near the mode, shifting the mode slightly to the higher values of T. The correction has an exponentially small effect on the tail of the Rayleigh density. The tail governs the probabilities of large waves and is the region of greatest engineering interest.

Figure 2-5 shows the Rayleigh density and $p(R)$ for various values of ν.

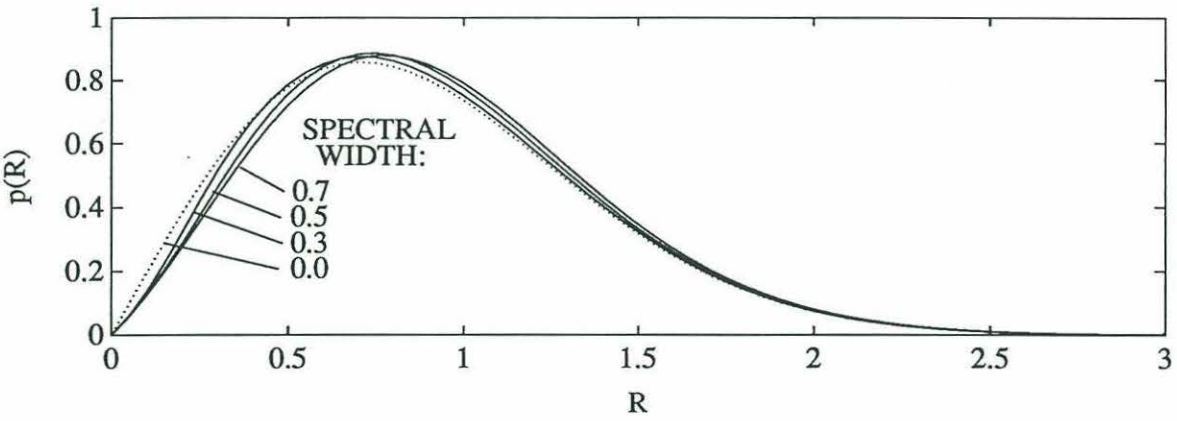

Figure 2-5: Marginal wave height densities, $p(R)$, for $\nu = (0, 0.3, 0.5, 0.7)$. The case with $\nu = 0$ is the Rayleigh distribution and is shown as the dotted curve.

2.2.7 Marginal Density of Wave Periods

The marginal density of wave periods, $p(T)$, is found by integrating $p(R,T)$ over all values of R in the interval $(0, \infty)$.

$$\begin{aligned} p(T) &= \int_0^\infty p(R,T)dR \\ &= \frac{2L(\nu)}{\nu T^2\sqrt{\pi}} \int_0^\infty R^2 e^{-R^2[1+(1-1/T)^2/\nu^2]} dR \\ &= \frac{2L(\nu)}{\nu T^2\sqrt{\pi}} [1+(1-1/T)^2/\nu^2]^{-\frac{3}{2}} \frac{\sqrt{\pi}}{4} \\ &= \frac{L(\nu)}{2\nu T^2} [1+(1-1/T)^2/\nu^2]^{-\frac{3}{2}} \end{aligned} \tag{2.109}$$

Figure 2-6 shows the marginal density, $p(T)$, for several values of spectral width.

2.2.8 Conditional Distribution of Wave Periods

The conditional distribution of periods for a given wave height is given by

$$\begin{aligned} p(T|R) &= \frac{p(R,T)}{p(R)} \\ &= \frac{1}{\nu}\frac{R}{T^2} e^{-R^2(1-1/T)^2/\nu^2} \left(\int_{-\infty}^{R/\nu} e^{-\beta^2} d\beta\right)^{-1} \end{aligned} \tag{2.110}$$

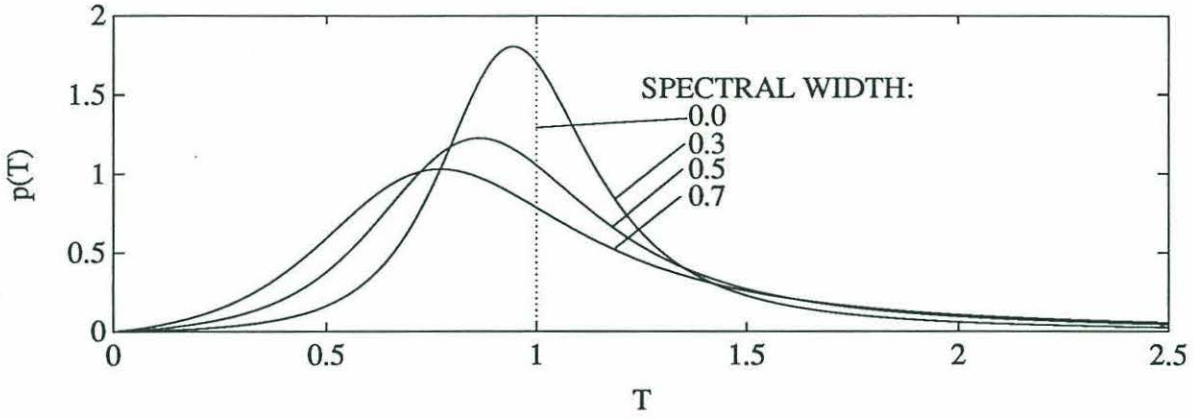

Figure 2-6: Marginal wave period densities, $p(T)$, for $\nu = (0, 0.3, 0.5, 0.7)$.

The mode, or peak, of this function is found where $\frac{\partial p(T|R)}{\partial T} = 0$. Differentiating (2.110) gives

$$\frac{\partial p(T|R)}{\partial T} = \frac{2R}{T^3\nu} e^{-R^2(1-1/T)^2/\nu^2} \left(\int_{-\infty}^{R/\nu} e^{-\beta^2} d\beta\right)^{-1} \left[\frac{2R^2}{\nu^2}\left(\frac{1}{T}\right)\left(1-\frac{1}{T}\right) - 1\right] \tag{2.111}$$

Then

$$\frac{\partial p(T|R)}{\partial T} = 0 \Rightarrow T = 2[1 + (1 + 4\nu^2/R^2)^{\frac{1}{2}}]^{-1} \tag{2.112}$$

gives the value of T at the mode.

The quartiles, Q_n, of the conditional distribution are found from

$$\int_0^{Q_n} p(T|R)dT = \frac{1}{4}n \tag{2.113}$$

$$n = 1, 2, 3$$

which is solved numerically for Q_n. For a fixed R, half the probability of $p(T|R)$ will lie in the interval $T \in (Q_1, Q_3)$. Figure 2-7 shows the quartiles and mode of $p(T|R)$ for various values of ν. Note how the highest waves are likely to have periods near 1.0.

2.2.9 Statistics of the Extreme Wave Heights

The distribution of R_{max}, the largest of N independent wave heights is of considerable interest. The marginal wave height density, (2.108), provides a base from which to derive $p(R_{max})$. The marginal density is very nearly equal to the Rayleigh density in the tail of

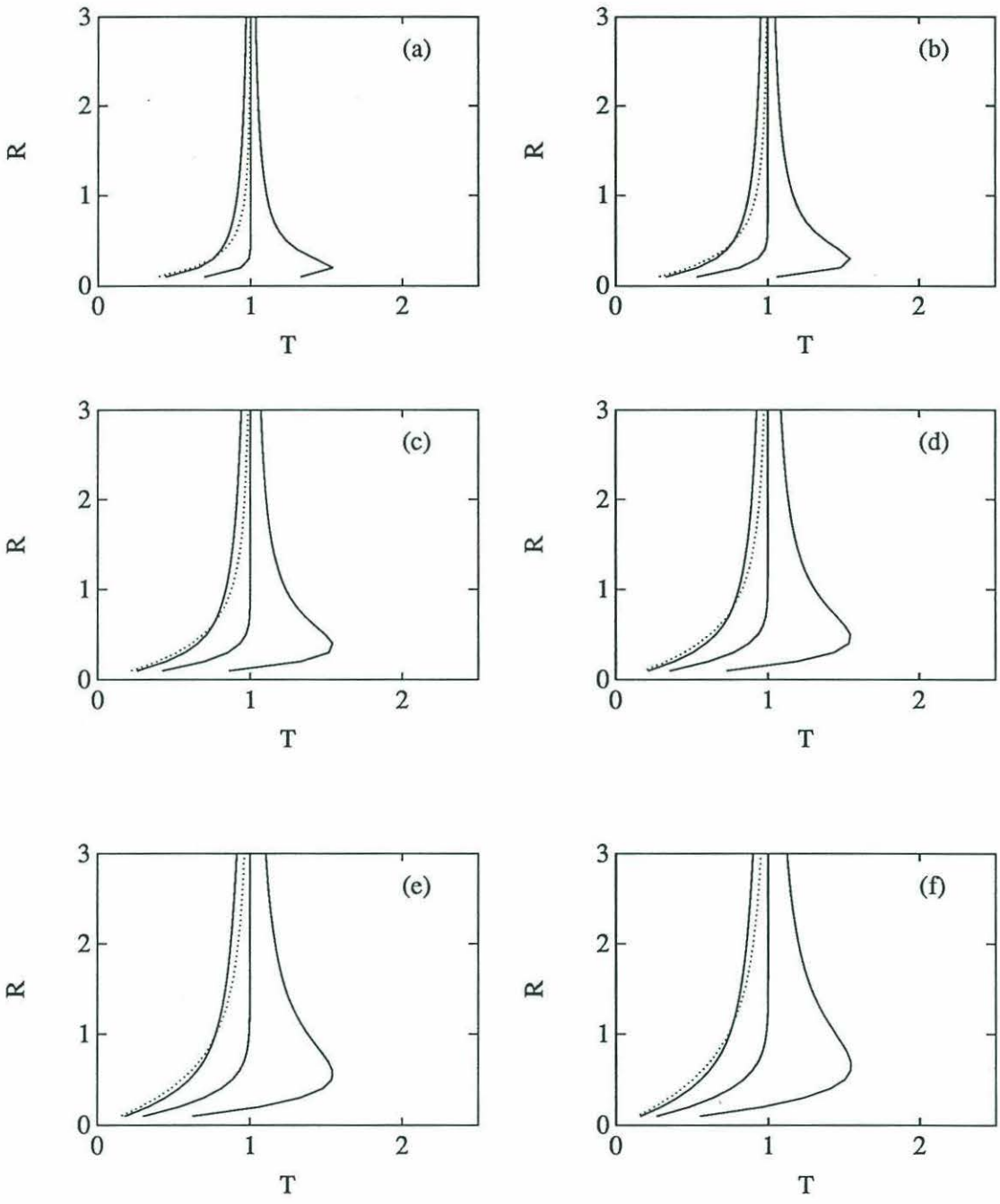

Figure 2-7: Quartiles (solid curves) and mode (dotted curve) of the conditional wave period distribution, $p(T|R)$.

the distribution. As noted in Section 2.2.6, it is the tail that controls the extreme value distribution. The following analysis is based on the simplification that $p(R)$ is Rayleigh.

$$p(R) = 2Re^{-R^2} \tag{2.114}$$

$$R \in (0, \infty)$$

Let $\Phi(R)$ represent the probability that a single realization of wave height exceeds the value R

$$\Phi(R) \equiv \int_R^\infty 2\beta e^{-\beta^2} d\beta = e^{-R^2} \tag{2.115}$$

The probability that a single realization is less than R is

$$1 - \Phi(R) = 1 - e^{-R^2} \tag{2.116}$$

N independent wave heights will all be less than R with probability

$$(1 - \Phi(R))^N \tag{2.117}$$

and the derivative of (2.117) gives the probability density for the maximum wave height

$$\begin{aligned} p(R_{max}) &= \frac{d}{dR_{max}}[(1 - \Phi(R_{max}))^N] \\ &= -N(1 - \Phi(R_{max}))^{N-1} \frac{\partial \Phi(R_{max})}{\partial R_{max}} \\ &= N(1 - e^{-R_{max}^2})^{N-1}(2R_{max}e^{-R_{max}^2}) \end{aligned} \tag{2.118}$$

Figure 2-8 shows $p(R)$ and $p(R_{max})$ for several values of N.

The expected value or mean of R_{max} is given by

$$\begin{aligned} E(R_{max}) &= \int_0^\infty R_{max} p(R_{max}) dR_{max} \\ &= \int_0^\infty R_{max} d[(1 - \Phi(R_{max}))^N] \\ &= -\int_0^\infty R_{max} d[1 - (1 - \Phi(R_{max}))^N] \end{aligned} \tag{2.119}$$

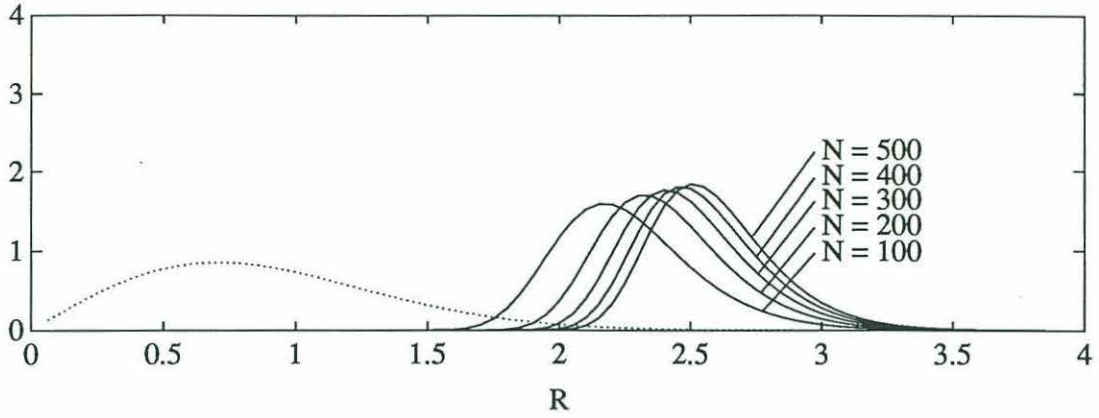

Figure 2-8: Wave height and extreme value probability distributions for groups of $N = (100, 200, 300, 400, 500)$ waves.

Integrating by parts produces

$$\begin{aligned} E(R_{max}) &= -R_{max}[1-(1-\phi(R_{max}))^N]|_0^\infty \\ &\quad + \int_0^\infty [1-(1-\Phi(R_{max}))^N] dR_{max} \\ &= \int_0^\infty [1-(1-\Phi(R_{max}))^N] dR_{max} \\ &= \int_0^\infty [1-(1-e^{-R_{max}^2})^N] dR_{max} \end{aligned} \tag{2.120}$$

Let $\theta \equiv R_{max}^2$.

$$E(R_{max}) = \frac{1}{2}\int_0^\infty [1-(1-e^{-\theta})^N]\theta^{-\frac{1}{2}} d\theta \tag{2.121}$$

This integral may be solved by employing the binomial theorem but the resulting expansion has terms involving $N!$ and is practical only for small N. The following approximation suggested by Longuet-Higgins (1952) proves useful. Substituting

$$\theta_0 \equiv \ln N \tag{2.122}$$

$$\theta \equiv \theta_0 + \theta' \tag{2.123}$$

leads to

$$\begin{aligned} (1-e^{-\theta})^N &= (1-e^{-(\theta_0+\theta')})^N \\ &= (1-\frac{e^{-\theta'}}{N})^N \end{aligned} \tag{2.124}$$

This function rises quickly from 0 to 1 in the vicinity of $\theta' = 0$. It may be simplified by letting $x = e^{-\theta'}$ and expanding in a Maclaurin series

$$(1 - \frac{x}{N})^N = 1 - x + \frac{x^2}{2!}\frac{(N-1)}{N} - \frac{x^3}{3!}\frac{(N-2)(N-1)}{N^2} + \cdots \tag{2.125}$$

For large N, this simplifies to

$$(1 - \frac{x}{N})^N \approx 1 - x + \frac{x^2}{2!} - \frac{x^3}{3!} + \cdots = e^{-x} \tag{2.126}$$

giving

$$(1 - e^{-\theta})^N \approx e^{-e^{-\theta'}} \tag{2.127}$$

$$1 - (1 - e^{-\theta})^N \approx 1 - e^{-e^{-\theta'}} \tag{2.128}$$

and

$$1 - (1 - e^{-\theta})^N \approx \begin{cases} 1 & \theta < \ln N \\ 0 & \theta > \ln N \end{cases} \tag{2.129}$$

Employing this approximation, the integral becomes

$$E(R_{max}) \approx \frac{1}{2}\int_0^{\theta_0} \theta^{-\frac{1}{2}} d\theta + C \tag{2.130}$$

where C is the approximation error. In fact, this error may be evaluated

$$\begin{aligned} C &= \frac{1}{2}\theta_0^{-\frac{1}{2}}[-\int_{-\infty}^{0} e^{-e^{-\theta'}} d\theta' + \int_0^{\infty}(1 - e^{-e^{-\theta'}})d\theta'] \\ &= \frac{1}{2}\theta_0^{-\frac{1}{2}}[-\int_1^{\infty} e^{-\alpha}\frac{d\alpha}{\alpha} + \int_0^1 (1 - e^{-\alpha})\frac{d\alpha}{\alpha}] \\ &= \frac{1}{2}\theta_0^{-\frac{1}{2}}[\int_0^{\infty}(\frac{1}{1+\alpha} - e^{-\alpha})\frac{d\alpha}{\alpha}] + C' \\ &\approx \frac{1}{2}\theta_0^{-\frac{1}{2}}\gamma \qquad (2.131) \\ \gamma &= 0.57722\ldots \text{Euler's constant} \end{aligned}$$

where C' is an error term of order $\theta_0^{-\frac{3}{2}}$. The expected value is therefore approximated as

$$E(R_{max}) \approx (\ln N)^{\frac{1}{2}} + \frac{1}{2}\gamma(\ln N)^{-\frac{1}{2}} \tag{2.132}$$

with an error of order $(\ln N)^{-\frac{3}{2}}$.

The expected value given by (2.132) is sometimes confused with the most probable value (Forristall 1978). The most probable value refers to that value of R_{max} for which

N	$E(R_{max})$	$\mu(R_{max})$	$\sigma_{R_{max}}$
100	2.2615	2.1779	0.2701
150	2.3502	2.2627	0.2607
175	2.3830	2.2910	0.2574
200	2.4111	2.3193	0.2546
225	2.4356	2.3476	0.2522
250	2.4573	2.3759	0.2501
275	2.4767	2.3900	0.2483
300	2.4944	2.4042	0.2467
325	2.5105	2.4183	0.2452
350	2.5253	2.4324	0.2439
500	2.5954	2.5032	0.2377

Table 2.1: Statistics of the extreme value of N independent wave heights.

$p(R_{max})$ takes its maximum value and is sometimes designated $\mu(R_{max})$. It is slightly smaller than $E(R_{max})$.

The variance of R_{max}

$$\sigma^2_{R_{max}} = \int_0^\infty R^2_{max} p(R_{max}) dR_{max} - E(R_{max})^2 \tag{2.133}$$

is difficult to find analytically. Representative values found numerically are listed in Table 2.1.

It will be more useful to have an expression for the distribution of the extreme wave height expected during a time interval of fixed length t as the number of waves will not be known *apriori*. The expected frequency of zero-up-crossings, $\overline{N_{0+}}$, is found by Rice (1945) to be

$$\overline{N_{0+}} = \frac{1}{2\pi}(\frac{m_2}{m_0})^{\frac{1}{2}} \tag{2.134}$$

which gives the expected number of waves in a time interval of length t to be

$$\overline{N} = \frac{t}{2\pi}(\frac{m_2}{m_0})^{\frac{1}{2}}. \tag{2.135}$$

This gives an expected maximum wave height during the interval

$$E(R_{max}) = (\ln \frac{t}{2\pi}\sqrt{\frac{m_2}{m_0}})^{\frac{1}{2}} + \frac{1}{2}\gamma(\ln \frac{t}{2\pi}\sqrt{\frac{m_2}{m_0}})^{-\frac{1}{2}} \tag{2.136}$$

2.2.10 Significant Wave Height

The significant wave height, H_s, is a commonly used measure of sea state. It is defined as the average of the highest one-third wave heights. Given a theoretical distribution for

the wave heights, H_s is found as the mean of the highest one-third of the distribution. The following is solved for H_c, the lower limit of the upper one-third of the heights

$$\Pr[H > H_c] = \int_{H_c}^{\infty} p(H)\, dH = \frac{1}{3} \tag{2.137}$$

Then H_s is given by

$$H_s = 3 \int_{H_c}^{\infty} H\, p(H)\, dH \tag{2.138}$$

A normalized significant wave height, R_s, may be similarly defined using the probability density $p(R)$ of normalized wave height. If wave height is normalized by

$$R = \frac{H}{\sqrt{8m_0}} \tag{2.139}$$

then

$$p(R) = p(H)\sqrt{8m_0} \tag{2.140}$$

Under the assumption that waves are Rayleigh distributed (equivalent to the assumption that in (2.108) $\nu = 0$), the normalized probability density is given by

$$p(R) = 2Re^{-R^2} \tag{2.141}$$

and the procedure described above yields

$$R_c = \sqrt{\ln 3} \tag{2.142}$$

$$R_s = 1.416\cdots \tag{2.143}$$

$$H_s = \sqrt{m_0} \times 4.004\cdots \tag{2.144}$$

Due to this result, significant wave height is often approximated $H_s \approx 4\sqrt{m_0}$.

When spectral width is non-zero, the normalized wave height distribution is given by the full (2.108). The following is solved for R_c,

$$\frac{1}{3} = \int_{R_c}^{\infty} \frac{2}{\sqrt{\pi}} Re^{-R^2} L(\nu) \int_{-\infty}^{R/\nu} e^{-\beta^2}\, d\beta\, dR \tag{2.145}$$

Changing the order of integration,

$$\frac{1}{3} = \frac{L(\nu)}{\sqrt{\pi}} \Big[\int_{-\infty}^{R_c/\nu} e^{-\beta^2}\, d\beta \int_{R_c}^{\infty} 2Re^{-R^2}\, dR \tag{2.146}$$

$$+ \int_{R_c/\nu}^{\infty} e^{-\beta^2}\, d\beta \int_{\beta\nu}^{\infty} 2Re^{-R^2}\, dR \Big] \tag{2.147}$$

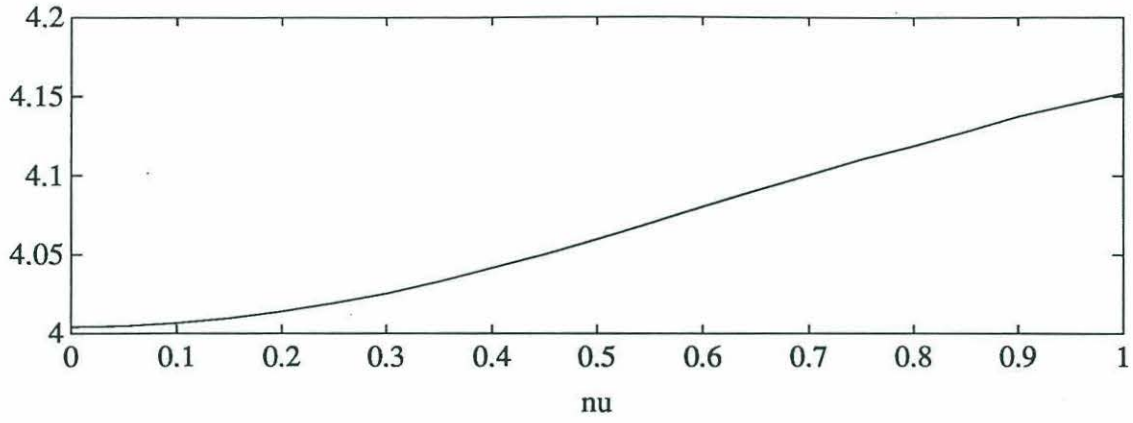

Figure 2-9: Expected value of $H_s/\sqrt{m_0} = R_s\sqrt{8}$ as a function of spectral width.

gives

$$\frac{1}{3} = \frac{L(\nu)}{2}[e^{-R_c^2}(1 + \text{erf}(R_c/\nu)) + \frac{1}{\sqrt{1+\nu^2}}(1 - \text{erf}(\frac{R_c}{\nu\sqrt{1+\nu^2}}))] \tag{2.148}$$

This is best solved numerically for R_c. Then R_s is found by integrating

$$R_s = 3\int_{R_c}^{\infty} 2R^2 e^{-R^2} L(\nu) \int_{-\infty}^{R/\nu} e^{-\beta^2} d\beta \, dR \tag{2.149}$$

Figure 2-9 shows $R_s\sqrt{8}$ for ν values from 0.0 to 1.0. Note the deviation from the approximate value of 4.0 at high spectral widths. The change is slight, with $\nu = 0.8$ giving a significant wave height only three percent larger than $\nu = 0.0$ for the same spectral energy.

2.3 Extension to Non-Narrow-Band Seas

The wave height and period distributions of Section 2.2 were derived based on the narrow-band hypothesis. This requires the spectral energy to be concentrated in a narrow range of frequencies. It is reasonable to assume that the sea may sometimes satisfy this requirement. The most satisfactory situation is a sea state dominated by waves from a distant storm of limited duration. Wind waves generated by the storm may have energy spread over a wide frequency band. Since gravity waves are dispersive, they will spread out according to frequency. The longest period waves (lowest frequencies) will arrive

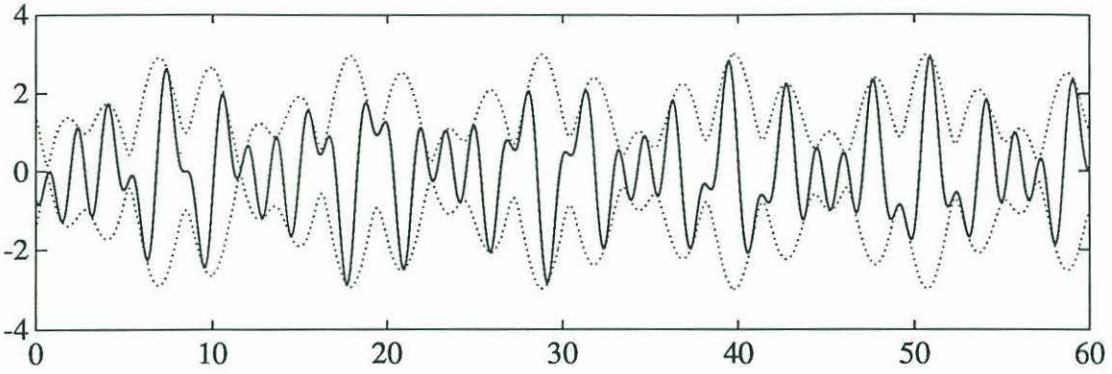

Figure 2-10: Non-narrow-band signal, $\eta(t)$, with its envelope function.

first in the area of interest. Therefore, a measurement interval that is not too long will include waves of nearly a single frequency. The associated power density spectrum will be narrow-banded.

Real seas often have spectra which are not characterized by the description above. Their spectra often deviate from the narrow-band case in two ways:

- There is a single peak but it is not sufficiently narrow ($\nu > 0.6$), or
- Energy is concentrated around two or more distinct peaks.

These spectral shapes do not support the preceding distributions of wave heights and periods. The joint probability density of the envelope amplitude and phase rate, (2.90), is unchanged, assuming the assumptions needed to linearize the equations of motion and superimpose the results are still satisfied. It is no longer possible, however, to find the wave height and period from the envelope amplitude and phase rate. It works for the narrow-band case because the envelope varies slowly compared to the carrier wave. For non-narrow-band seas, the amplitude and phase no longer vary slowly. As Figure 2-10 shows, there may be maxima and minima not associated with extrema of the carrier wave. There is no simple method to transform (2.90) to the joint distribution of wave height and period.

Cartwright and Longuet-Higgins (1956) present a theoretical distribution of sea surface height maxima that is valid for all spectral widths. This distribution is not used here for

two reasons.

The objective in studying the distribution of wave heights and periods is often to find the wave orbital velocities. For sinusoidal waves, (2.40) and (2.41) relate these velocities to crest-to-trough wave height and zero-crossing period. There is no simple relationship between orbital velocities and the distribution of sea surface height maxima.

The distribution of maxima depends on the fourth moment of the energy spectrum which is sensitive to the high frequency behavior of the spectrum. This is not desirable when applied to real sea surface height data.

Chapter 3

Sea Surface Height Data Set

3.1 Data Acquisition

Woods Hole Oceanographic Institution's Telemetry Project maintained a Waverider buoy southwest of Martha's Vineyard from Spring of 1987 until Autumn of 1988. The buoy sensed sea surface acceleration and generated a time history of sea surface height. The elevation record was then transmitted to WHOI where power density spectral estimates were computed. Data files were made available to interested users and archived in several formats.

A complete description of this data acquisition and dissemination project is available in Briscoe et al. (1988). Sharpe and Graber (1990) presents graphical and tabular summaries of wind and wave data collected over 16 months at five stations, including the Martha's Vineyard Waverider buoy.

3.1.1 Sea Surface Height Measurement

The Martha's Vineyard Buoy Telemetry Project was operated under the University Research Initiative Program at WHOI. A general goal of the project was to develop techniques for gathering *in situ* data from the ocean and disseminating them to users in a timely and efficient way. A secondary objective was to test the feasibility of a telemetering technique for long-term surface wave monitoring in coastal waters. The data collected provides a convenient record of sea surface elevation in the vicinity of Martha's Vineyard.

The Waverider buoy used in this project was moored 16 km southwest of Martha's Vineyard. The region is shown in Figure 3-1. Details of the mooring are depicted in Figure 3-2. The mooring is located in the Buoy Farm, an engineering test site operated by WHOI's Department of Applied Ocean Physics and Engineering.

The buoy, a 70 cm floating sphere, closely followed the ocean's surface. A gimbaled, gravity stabilized accelerometer measured vertical acceleration. This was integrated twice to get a continuous time history of sea surface height. The buoy was sensitive to acceleration at frequencies from 0.035 to 0.65 Hz (periods from 1.5 to 29 s).

Sea surface elevation was sampled at a rate of 2 Hz during 17 minute intervals centered on each hour and half hour. These records were transmitted to a station on Gay Head and from there to WHOI.

Processing at WHOI included computation of power spectral density estimates for each 17 minute record. Each record contains 2048 sea surface elevation values. These were divided into eight segments of 256 values each. The mean of each segment was found and removed and the spectral density estimates computed. Only the 60 estimates corresponding to frequencies from 4/128 to 63/128 Hz were retained.

3.1.2 Data Dissemination

After processing, the data were stored in three types of files.

- Raw data file:

  The 2048 sea surface elevation values.

- Spectral coefficient file:

  Contains the time, the spectral estimates, and three spectral moments, m_0, m_1, m_2 calculated using angular frequency.

- Computed product file:

  Contains date, time, sea surface variance (m_0), significant wave height ($4\sqrt{m_0}$), mean wave period (m_0/m_1), upcrossing wave period ($\sqrt{m_0/m_2}$), Waverider bias (a measure of transmission quality), maximum crest height, minimum trough height, and frequency of the spectral peak.

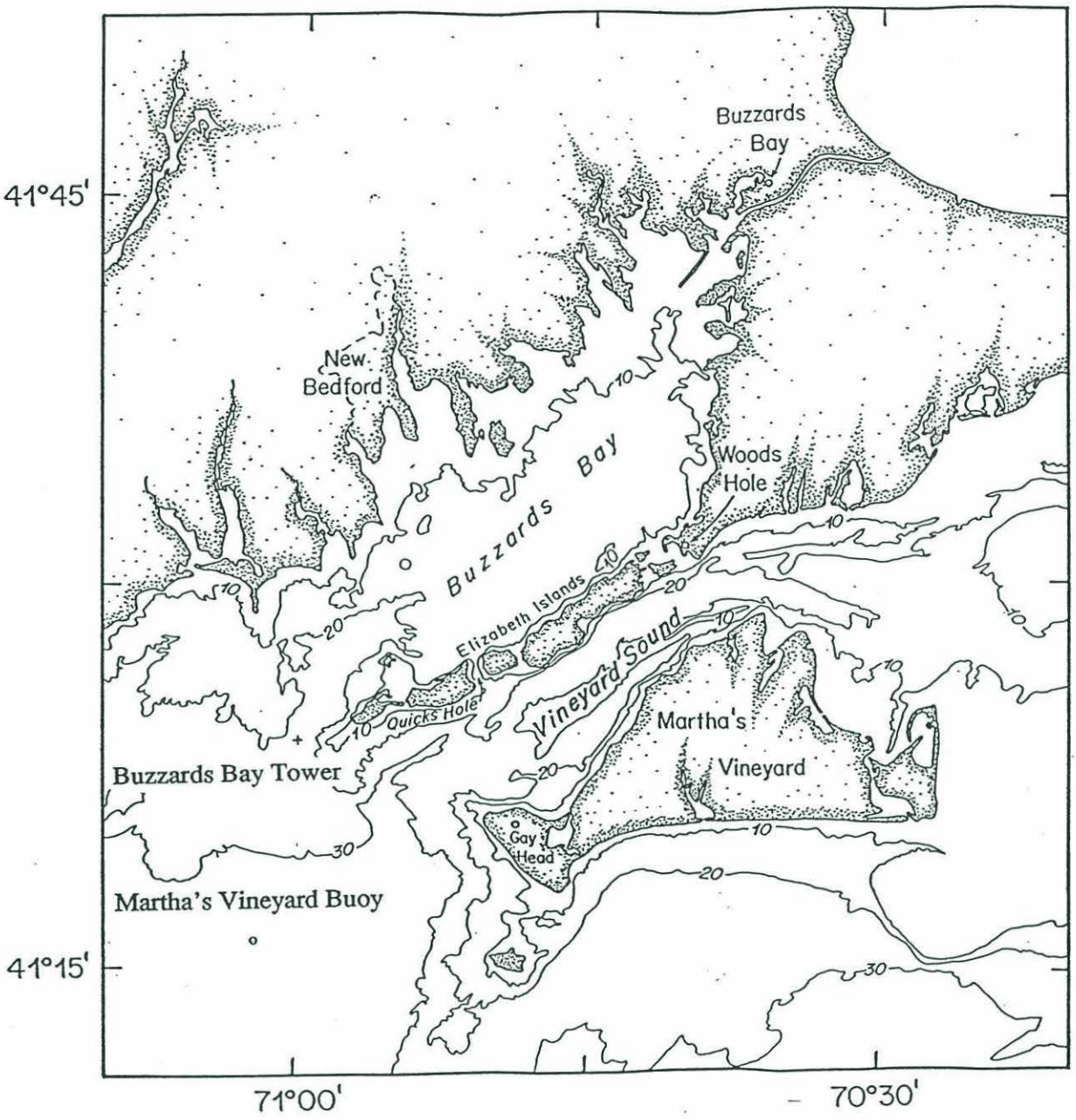

Figure 3-1: Waverider buoy and vicinity. From Sharpe and Graber (1990). The buoy is located at latitude 41° 16′ N and longitude 71° 02′ W in a water depth of 42 m.

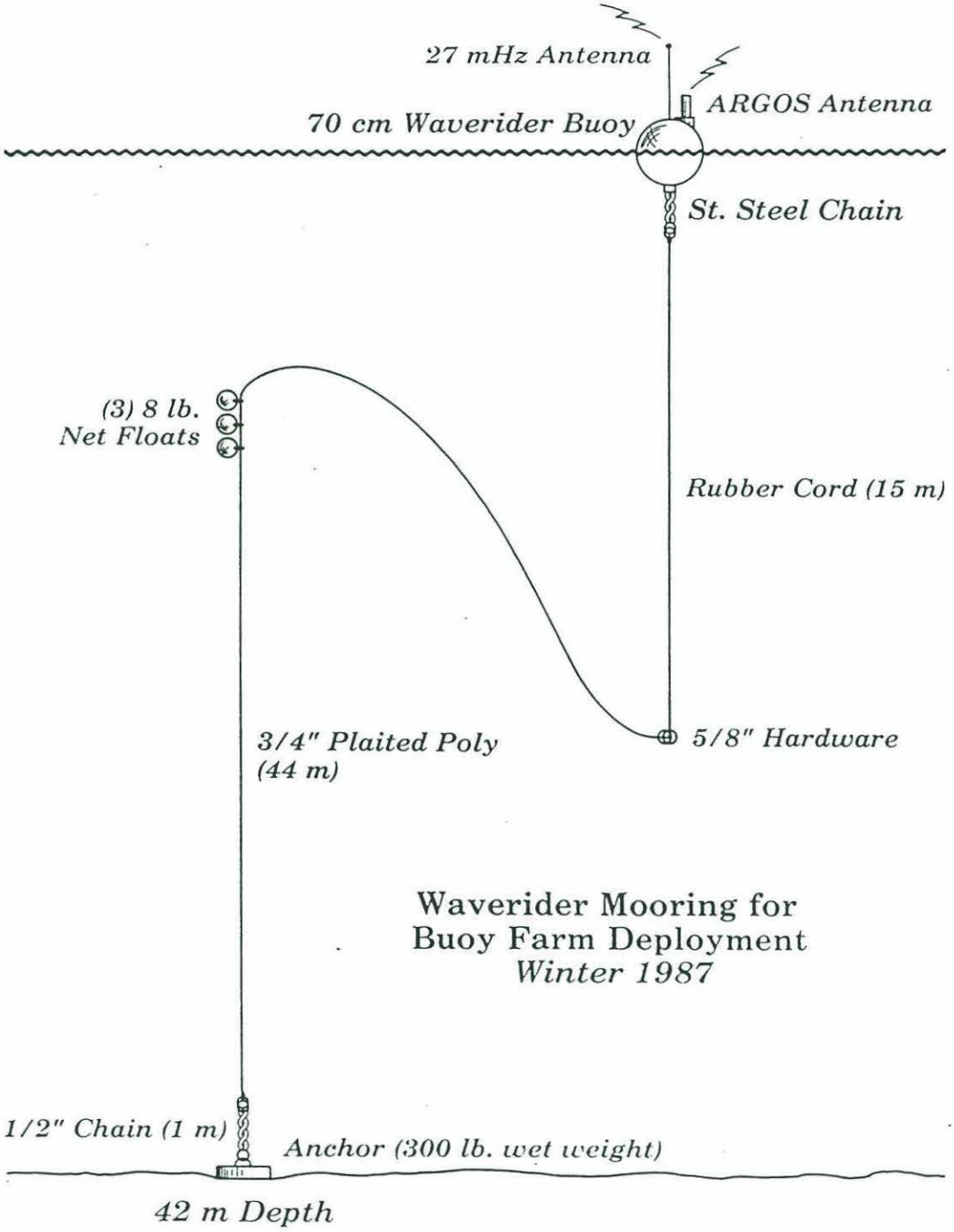

Figure 3-2: Waverider mooring schematic for Buoy Farm deployment. From Briscoe et al. (1988).

3.2 Finding Wave Heights and Periods from Sea Surface Elevation Data

It is necessary to find wave height and period pairs from the Waverider's records of sea surface elevation. This process would appear to consist of the following simple steps:

- Determine the times at which the sea surface rises through the mean level. These are the zero-up-crossing times.
- Record the differences between successive zero-up-crossing times as wave periods.
- Measure the range of elevation for each wave and record as wave height.

These steps, however, may not be performed until the time series has been properly interpolated, as described below.

3.2.1 The Need for Upsampling

The Waverider time series of sea surface elevations must be recognized as a set of discrete time samples of an underlying continuous time process. Wave heights and periods of the continuous time process are of interest. Zero-up-crossings of the underlying process will likely fall between samples, with one sample below the mean level and the following sample above. A method must be chosen to assign appropriate times to these events. The maximum and minimum elevations in a wave interval are also difficult to determine. The maximum sample is not likely to fall exactly at the wave crest of the underlying process. The actual crest height will be slightly higher than the highest sample, and the actual trough height slightly lower than the lowest sample. These actual elevations must be estimated from the discrete time samples.

One method used to overcome these difficulties is to resample the continuous time process at a higher rate so that the samples present a more complete picture of the process. Once this is done, there will be a sample value close enough to each zero-up-crossing that the sample time may be taken as the zero-crossing time. Similarly, the sample nearest to each crest or trough will be close enough so that the sample value may be taken as the extreme elevation.

Figure 3-3 demonstrates these effects for the simple case of a sine wave of constant amplitude and frequency. In the first plot, a 0.5 Hz sine wave has been sampled at a rate of 2 Hz. The continuous time process is shown as a dotted line and the samples are shown as small circles. Note how no sample adequately represents a zero-crossing nor an extreme. The second plot shows the same signal sampled at a rate of 10 Hz. Note how samples may be found which fall quite close to the features of interest.

3.2.2 Band-limited Interpolation

Ideally, one would generate the new time series by measuring the original process again at the new, higher sampling rate. For the sea surface elevations used here, that is, of course, not possible since the available data are sampled at 2 Hz. If the original measurements were made at a rate high enough to capture all the frequencies present in the continuous process, the discrete samples may be used to reproduce the original process exactly. The reconstructed process may be resampled at the desired rate. The critical sampling rate is called the Nyquist rate and it equals twice the highest frequency component present in the continuous time process. Since the Waverider samples sea surface elevation at a rate of 2 Hz, the samples carry a full description of the sea surface elevation if no appreciable energy is present at frequencies above 1 Hz (periods of less than 1 s). This is a reasonable assumption. Based on the buoy's frequency sensitivity (given in Section 3.1.1) and a knowledge of the periods of the wind waves of interest, it is reasonable to make the more restrictive assumption that wave energy is limited to frequencies below 0.5 Hz (periods greater than 2 s). This is consistent with the WHOI Telemetry Project's truncation of the power density spectral estimates for frequencies above 63/128 Hz. Under this assumption, the original sampling rate of 2 Hz exceeds the Nyquist rate by a factor of two and provides slight oversampling.

The method by which samples of a process are used to create a new sequence of more closely spaced samples is called band-limited or lowpass interpolation. Oppenheim and Schafer (1989, pp. 105–111) develop the theory of low-pass interpolation of discrete-time signals. An original sequence of length N that is resampled to length M is said to have been upsampled by a factor of M/N. This is carried out in two steps.

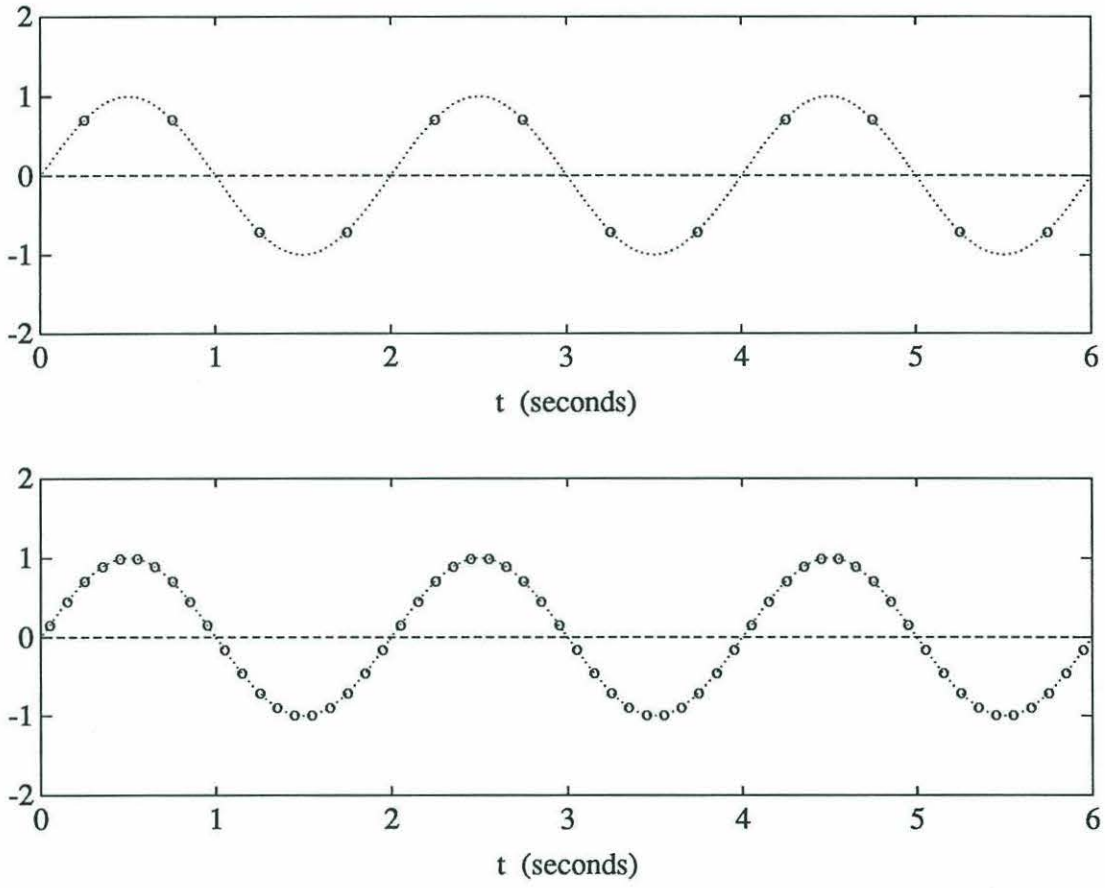

Figure 3-3: One-half Hz sine wave sampled at two rates. The continuous time process is shown as a dotted curve. The samples are shown as circles. First plot shows samples at twice the Nyquist rate. Note how zero-crossings, maxima and minima of the underlying process are poorly represented by the samples. The second plot shows the same process sampled at ten times the Nyquist rate. The samples are now dense enough to show the sine wave's shape clearly.

First, $M/N - 1$ zero values are inserted between each pair of original samples. The result is filtered using a discrete time finite impulse response (FIR) filter. The filter has a cutoff frequency appropriate for the bandwidth of the data and is designed to leave the original sample values unchanged and to assign the appropriate interpolated values to the new samples. Details of the Matlab algorithm used to perform the interpolation are found in Little and Shure (1988, pp. 2–73,74).

The Waverider sea surface heights, originally sampled at 0.5 s intervals were upsampled by a factor of five to get 0.1 s spacing. The FIR filter used had a cutoff frequency of 0.5 Hz. A sample segment is shown in Figure 3-4. The first plot shows the original samples. The second plot shows the result after upsampling. The original samples are unchanged but the new samples help to fill in and better depict the continuous process.

3.2.3 Other Interpolation Methods

Some studies of wave statistics have upsampled using linear interpolation (Chakrabarti and Cooley 1977). This is a simpler computation but the interpolated values are distorted samples of the underlying process, even when the process is band limited. The distortion is acceptably small only if the original process is sampled at many times the Nyquist rate (Oppenheim and Schafer 1989).

Most spectra observed in the present study show negligible energy at the highest frequencies and are effectively oversampled. Linear interpolation would adequately reproduce the sea surface for all but the shortest period waves. The computational feasibility of band-limited interpolation makes it unnecessary to accept even this limited amount of distortion. Linear interpolation is not used here.

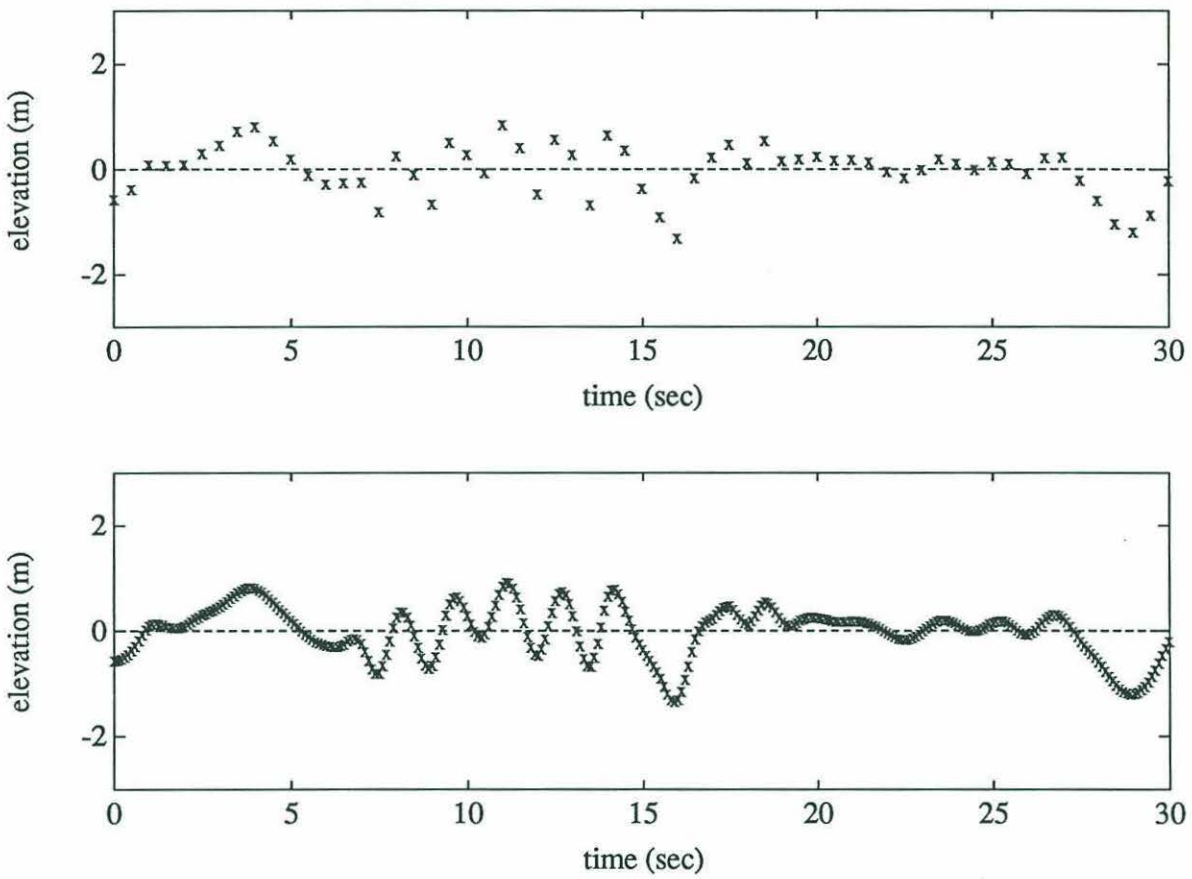

Figure 3-4: Thirty second segment of Waverider sea surface height record. Upper plot shows samples at original sampling rate of 2 Hz. Lower plot shows sequence interpolated to a rate of 10 Hz.

3.3 Characterizing the Power Density Spectra

A six parameter formulation has been developed that expresses a spectrum as the sum of a low frequency component and a high frequency component. This spectrum is fit to each power density spectrum computed from its Waverider sea surface height record. The result is used to classify each spectrum as unimodal or bimodal. Bimodal spectra are further classified by the relative sizes and locations of the two peaks.

3.3.1 Development of the Six Parameter Spectrum

Traditional mathematical descriptions of wave spectra have a single peak and a tail that decreases exponentially with frequency. Many observed spectra show multiple peaks or have a plateau of nearly constant energy at high frequencies. The traditional spectral formulations may fit the low frequency part of these observed spectra reasonably well but cannot express the high frequency peak nor plateau.

To develop a formulation with wider applicability to observed spectral shapes, Ochi and Hubble (1976) developed a six parameter spectrum

$$S(\sigma) = \frac{1}{4}\sum_{j=1}^{2} \frac{[(4\lambda_j+1)\sigma_{mj}^4/4]^{\lambda_j}}{\Gamma(\lambda_j)} \frac{\zeta_j^2}{\sigma^{4\lambda_j+1}} \exp[-(\frac{4\lambda_j+1}{4})(\frac{\sigma_{mj}}{\sigma})^4] \tag{3.1}$$

with σ in radians per second, or

$$S(f) = \frac{\pi}{2}\sum_{j=1}^{2} \frac{[(4\lambda_j+1)(2\pi f_{mj})^4/4]^{\lambda_j}}{\Gamma(\lambda_j)} \frac{\zeta_j^2}{f^{4\lambda_j+1}} \exp[-(\frac{4\lambda_j+1}{4})(\frac{f_{mj}}{f})^4] \tag{3.2}$$

with f in cycles per second. The spectrum decomposes into two parts, each with three parameters. The two parts have identical algebraic expressions and differ only in the values taken by the parameters.

The parameter ζ_j determines the size (energy) of each part. This energy, the moment m_{0j} of the appropriate part of (3.2), is found to satisfy

$$\zeta_j = 4\sqrt{m_{0j}} \tag{3.3}$$

and for this reason ζ_j is referred to as significant wave height. This terminology is unfortunate because ζ_j does not equal the original definition of significant wave height H_s given

in section 2.2.10. The different notation will serve to keep the two quantities distinct. For the combined spectrum, (3.2), one finds

$$4\sqrt{m_0} = \sqrt{\zeta_1^2 + \zeta_2^2} \tag{3.4}$$

The modal frequency, σ_m or f_m, is a location parameter. It positions the spectrum by fixing the position of its maximum value.

The parameter λ controls the spectral shape. Large values of λ generate a sharply peaked shape with a rapidly decaying tail. Small values give a flat shape with considerable energy in the tail. The tail decays as $\sigma^{-(4\lambda+1)}$.

Figure 3-5 shows the effect of varying each of the parameters with the others held constant.

3.3.2 Fitting the Six Parameter Spectrum to Data

The six parameter spectrum is fit to each observed power density spectrum by finding the appropriate values for the parameters. This is a non-linear minimization problem in six dimensions. The parameters are selected to minimize the sum of the squared errors between the 60 spectral estimates and the spectrum evaluated at the estimates' frequencies.

The minimization is carried out using the Nelder-Mead simplex algorithm. This method is chosen because it is simple and requires function evaluations only, not evaluations of derivatives. Details of multi-dimensional minimization using this method are found in Press et al. (1986).

3.3.3 Identifying Unimodal and Bimodal Spectra

Once the six parameter formulation is fit to a power density spectrum, it is used to place the spectrum into one of two categories, unimodal or bimodal. A unimodal power density spectrum has a single peak. The six parameter spectrum has one peak and no local minimum. A bimodal power density spectrum has energy distributed between two distinct peaks. The six parameter spectrum has a local minimum, dividing the low frequency

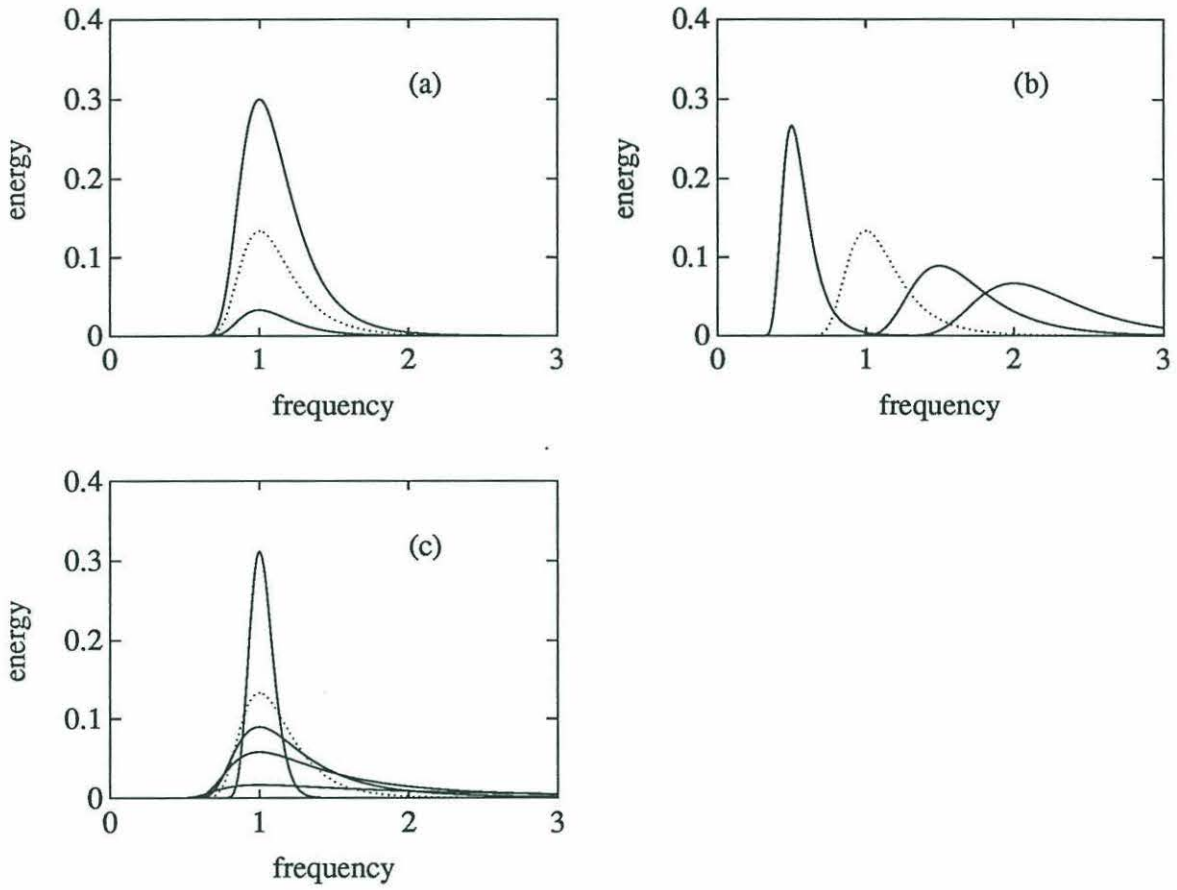

Figure 3-5: Effect of varying parameters on the three parameter shape $S(\sigma)$. When they are held constant, parameters take the following values: $\zeta = 1$ m, $\sigma_m = 1$ rad/s, $\lambda = 2.0$. (a) $\zeta = 0.5, 1.0, 1.5$ m; (b) $\sigma_m = 0.5, 1.0, 1.5, 2.0$ rad/s; (c) $\lambda = 0.1, 0.5, 1.0, 2.0, 10.0$.

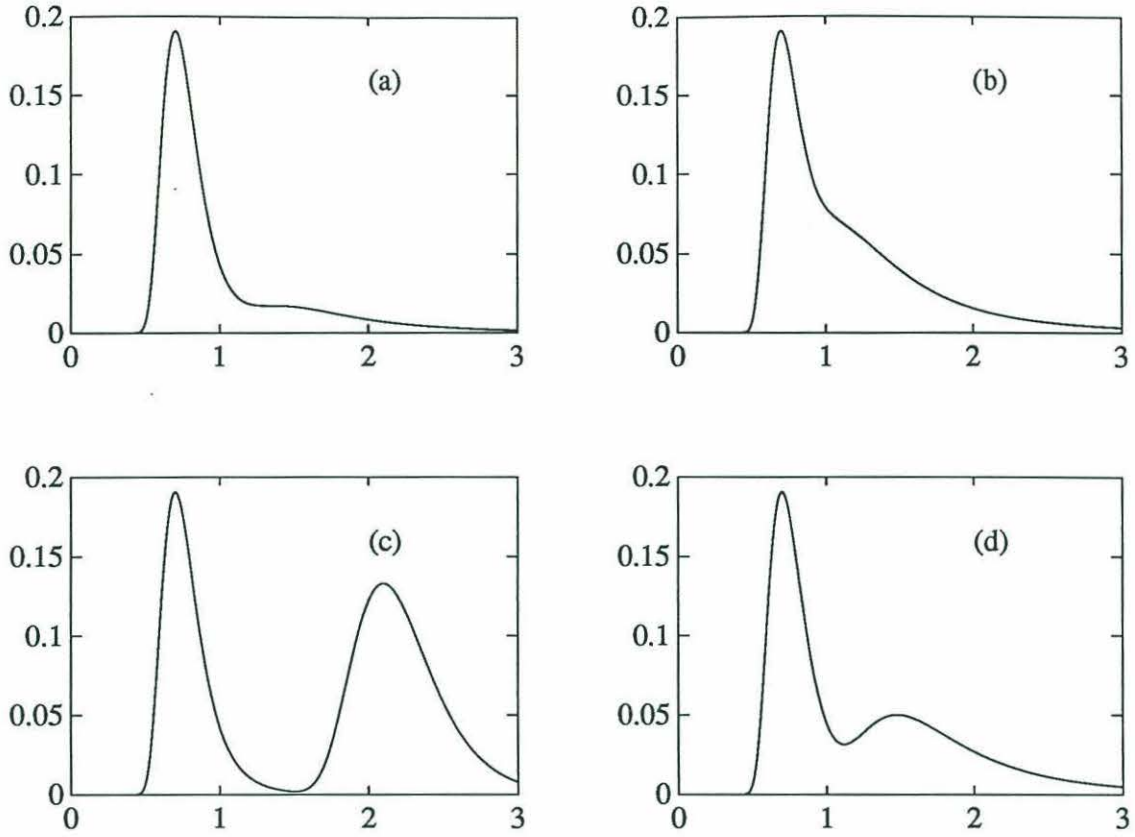

Figure 3-6: Typical six parameter spectral shapes. (a,b) Unimodal. (c,d) Bimodal.

region from the high frequency region. Figure 3-6 shows examples of six parameter spectra for unimodal and bimodal cases.

Power density spectra which are designated as bimodal are further characterized by the energy and position of the low and high frequency regions. If the local minimum in the six parameter spectrum is located at a frequency $f = f_{min}$, then the power density spectral estimates are broken into two groups:

$$\begin{aligned} &\text{Low frequency} \quad f < f_{min} \\ &\text{High frequency} \quad f > f_{min} \end{aligned}$$

The moments m_0 and m_1 are found from the spectral estimates for each section independently. For each section, an energy, $e = m_0$, and mean frequency, $\bar{f} = m_1/(2\pi m_0)$, are

found. From these, energy and frequency ratios

$$e_r = e_2/e_1 \tag{3.5}$$

$$f_r = \bar{f}_2/\bar{f}_1 \tag{3.6}$$

are found, with the subscript 1 referring to the low-frequency domain and the subscript 2 referring to the high-frequency domain.

The energy ratio, e_r, is a measure of the relative strengths of the two peaks. A small e_r means the low frequency peak dominates. A high e_r means the high frequency peak is larger.

The frequency ratio, f_r, gives a measure of the separation of the peaks. A large f_r indicates the peaks are widely separated. As f_r decreases, the peaks move closer together. Values of $f_r < 1.5$ are not observed in data because peaks that are sufficiently close together have no local minimum and are classified as unimodal.

It should be emphasized that the energy and frequency ratios are computed from the power density spectral estimates. The six parameter spectrum is used only to identify the spectrum as unimodal or bimodal and to divide the bimodal spectra into two sections. Moments are not calculated from the six parameter spectra.

3.4 Examples of Unimodal and Bimodal Seas

The figures which follow show sea surface elevation time series and spectral information from seas typical of four spectral classifications. The first two figures show seas with spectra classified as unimodal. The last two figures show bimodal seas. The following plots are provided for each sea condition:

- Power density spectral estimates (60 values). The six parameter spectrum is superimposed.
- Thirty second segment of sea surface elevation time series.
- Three minute segment of sea surface elevation time series.

Figure 3-7 represents seas with a unimodal spectrum and a small spectral width. For the example shown,

$$\nu = 0.2658.$$

The time series clearly shows the behavior of a carrier wave modulated by a slowly varying envelope function.

Figure 3-8 represents seas with a unimodal spectrum and a large spectral width. For the example shown,

$$\nu = 0.5769.$$

Figure 3-9 represents seas with a bimodal spectrum dominated by low frequency swell. For the example shown,

$$\nu = 0.5496,$$

$$e_r = 0.4014.$$

Figure 3-10 represents seas with a bimodal spectrum dominated by high frequency wind sea. For the example shown,

$$\nu = 0.4004,$$

$$e_r = 3.206.$$

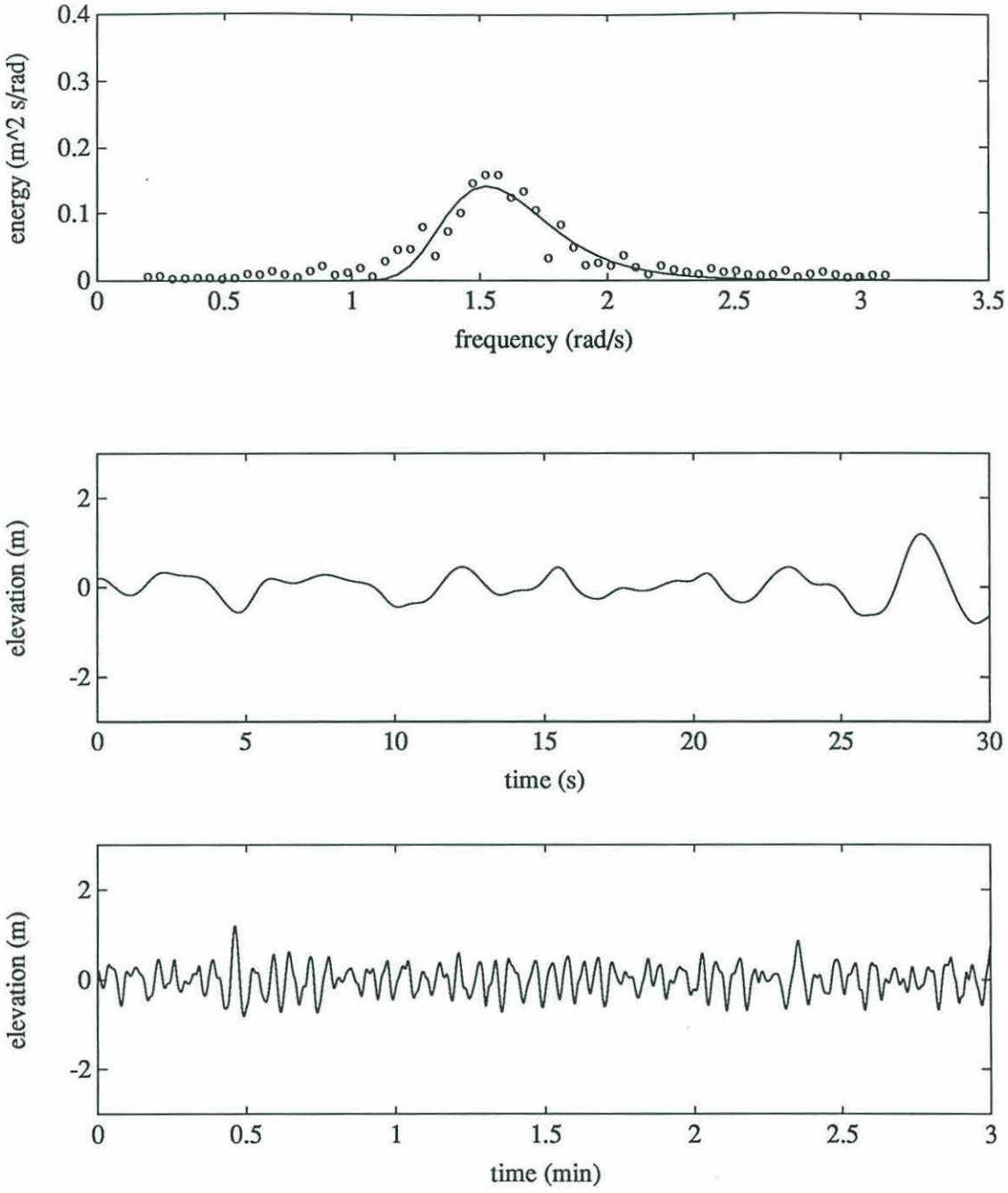

Figure 3-7: Time and frequency domain behavior of a sea with a unimodal spectrum and narrow bandwidth. (a) Power density spectral estimates and the best fit six parameter spectrum. The estimates are shown as circles and the six parameter spectrum as a solid curve. Spectra are in units of meters squared per radian per second. (b) Thirty second segment of sea surface elevation record. Elevation is in meters. (c) Three minute segment of the record.

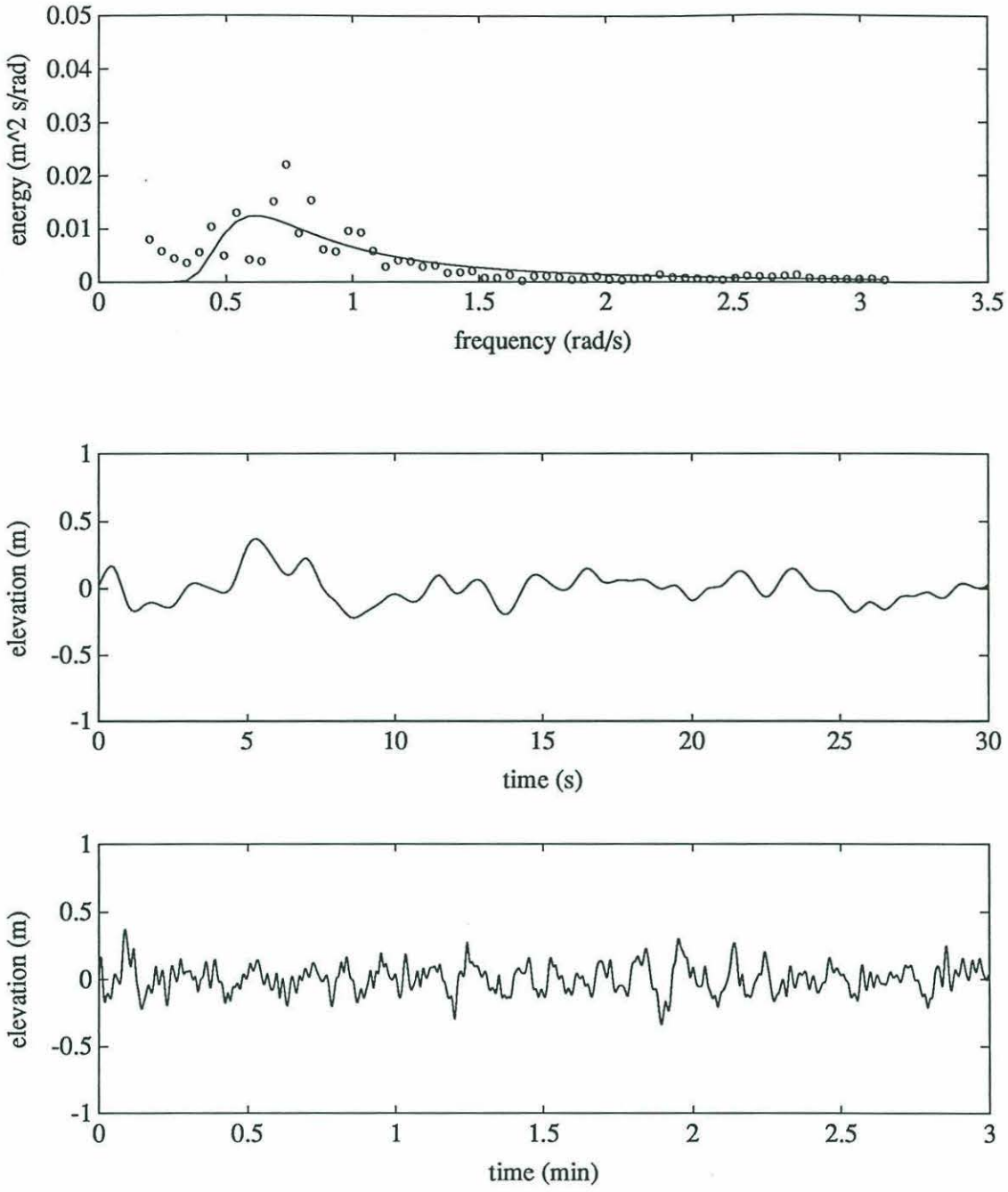

Figure 3-8: Time and frequency domain behavior of a sea with a unimodal spectrum and wide bandwidth. (a) Power density spectral estimates and the best fit six parameter spectrum. The estimates are shown as circles and the six parameter spectrum as a solid curve. Spectra are in units of meters squared per radian per second. (b) Thirty second segment of sea surface elevation record. Elevation is in meters. (c) Three minute segment of the record.

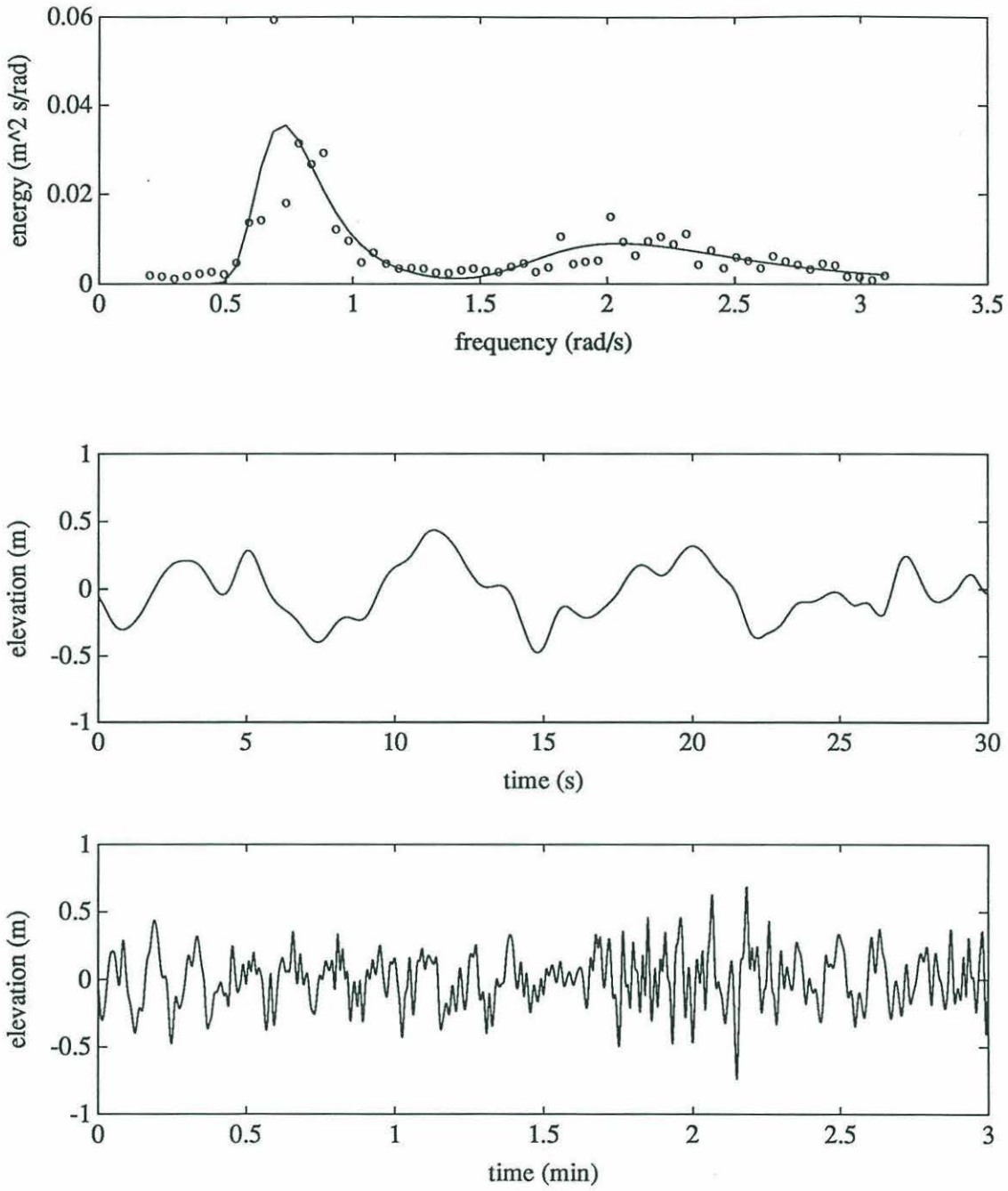

Figure 3-9: Time and frequency domain behavior of a swell-dominated sea with a bimodal spectrum. (a) Power density spectral estimates and the best fit six parameter spectrum. The estimates are shown as circles and the six parameter spectrum as a solid curve. Spectra are in units of meters squared per radian per second. (b) Thirty second segment of sea surface elevation record. Elevation is in meters. (c) Three minute segment of the record.

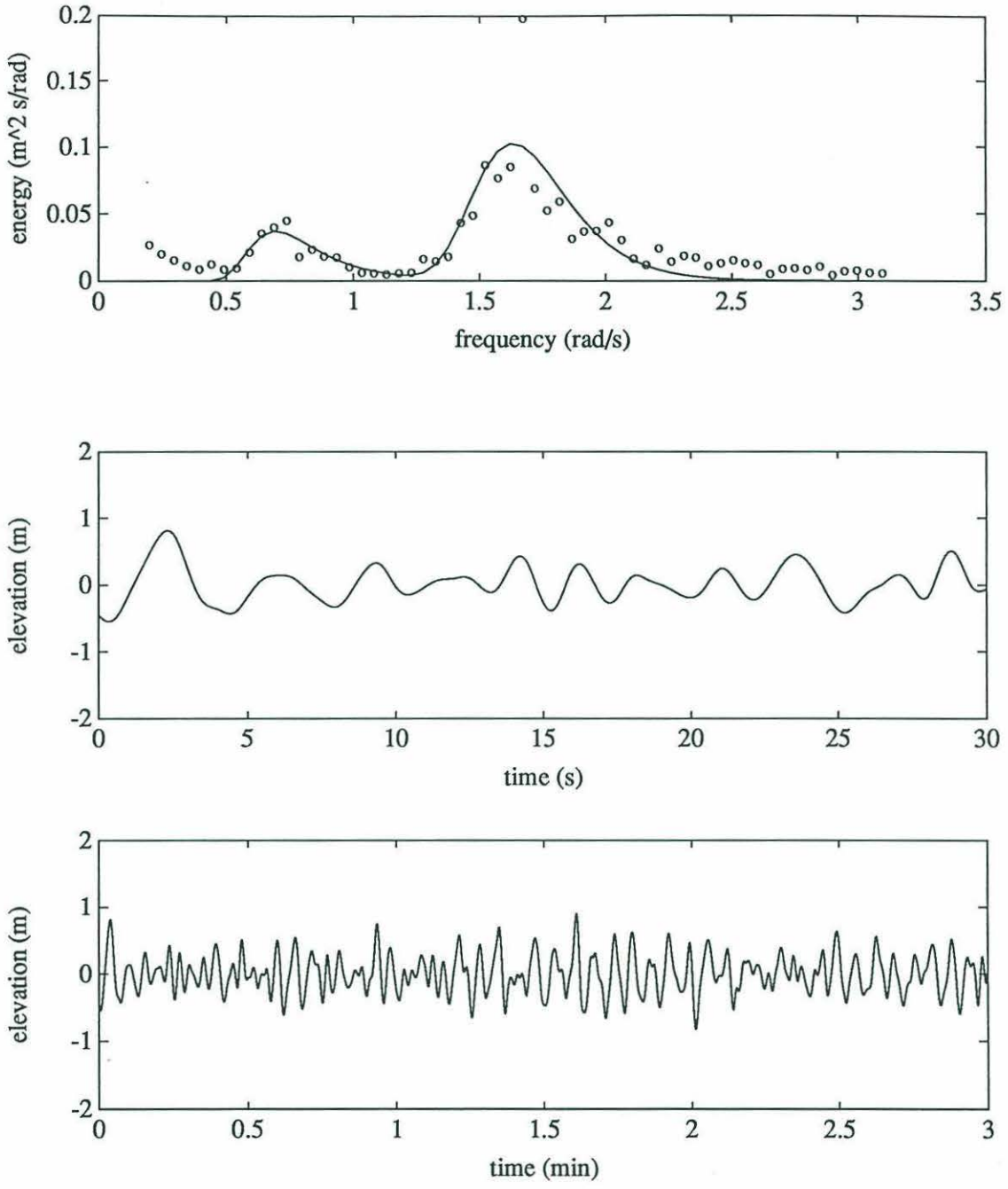

Figure 3-10: Time and frequency domain behavior of a sea with a bimodal spectrum. The swell energy is smaller than the high frequency wind sea energy. (a) Power density spectral estimates and the best fit six parameter spectrum. The estimates are shown as circles and the six parameter spectrum as a solid curve. Spectra are in units of meters squared per radian per second. (b) Thirty second segment of sea surface elevation record. Elevation is in meters. (c) Three minute segment of the record.

Chapter 4

Comparison of Wave Data to Theoretical Distributions

4.1 Overview of the Data Analyses

Narrow-band theory proposes a joint distribution for wave height and period for seas with narrow spectra. Twelve months of sea surface monitoring by WHOI's Martha's Vineyard Waverider buoy provide several thousand 17 minute sea surface elevation time series. The availability of these time series and their power density spectra allows comparison of the observed wave heights and periods to those predicted by narrow-band theory.

4.1.1 Questions to be Investigated

The theoretical joint density of normalized wave height and period, $p(R,T)$, is a function of the single parameter, ν, the spectral width. Given the three lowest spectral moments, m_0, m_1, m_2, the joint distribution may be transformed to one involving dimensional height and period, $p(H,\tau)$.

While the description of waves of all heights and periods is important, the behavior of the highest waves is of particular interest to ocean engineering and marine operations. One would like to know the accuracy of narrow-band theory in describing the significant wave height and the height and period of the highest wave in a given time period.

In the analyses which follow, observed wave heights and periods are compared to those

predicted by narrow-band theory from spectral information. This is done for unimodal seas with narrow spectra, where the theory is expected to work well, and for wide unimodal and bimodal seas, where narrow-band theory is no longer valid but may still provide useful information.

Analyses are performed to support the following inquiries.

- Is the applicability of narrow-band theory to describe the distribution of wave heights and periods a function of the spectral width?
- Is the accuracy different for unimodal and bimodal seas of the same spectral width?
- Where observed values fall outside the range predicted by narrow-band theory, how large are the errors?

4.1.2 Selecting Time Series for Analysis

Time series representing the spectral shapes and widths of interest are selected from among the 10,928 available time series. The series are grouped as unimodal or bimodal using the procedure described in section 3.3. There are 5,021 unimodal and 5,907 bimodal series. Within the two major groups, subgroups with 25 time series each are built such that the seas represented in each subgroup cover a narrow range of spectral widths.

The frequency of occurrence of spectral widths for twelve months of records is shown in Figure 4-1 for unimodal and bimodal seas. The records are densely spaced in spectral width such that the 25 seas in each subgroup have nearly equal width.

Selecting 25 as the number of seas in each subgroup represents a compromise between conflicting objectives. It is small enough to allow each subgroup to cover a small range of spectral width but large enough to allow statistical conclusions to be drawn.

Table 4.1 shows the mean spectral width, $\bar{\nu}$, and the range of widths covered by each subgroup.

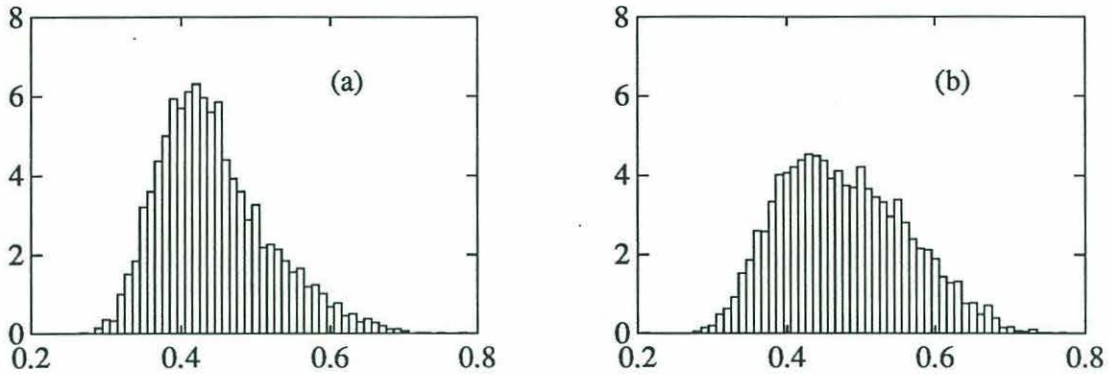

Figure 4-1: Histograms showing the density of spectral width for (a) unimodal seas, and (b) bimodal seas. Spectral width, ν, is shown on the horizontal axis. The vertical axis scale is adjusted so the total area under the histogram is unity.

Unimodal Group

Subgroup	ν_{min}	$\bar{\nu}$	ν_{max}
1	0.2903	0.2999	0.3087
2	0.3493	0.3500	0.3509
3	0.3993	0.3999	0.4004
4	0.4488	0.4491	0.4495
5	0.4991	0.5000	0.5011
6	0.5479	0.5499	0.5528
7	0.5968	0.5997	0.6046
8	0.6423	0.6499	0.6617

Bimodal Group

Subgroup	ν_{min}	$\bar{\nu}$	ν_{max}
1	0.2910	0.3003	0.3085
2	0.3485	0.3500	0.3511
3	0.3995	0.4000	0.4004
4	0.4495	0.4500	0.4506
5	0.4995	0.5000	0.5008
6	0.5495	0.5500	0.5507
7	0.5991	0.6000	0.6011
8	0.6389	0.6424	0.6455
9	0.6848	0.6991	0.7224

Table 4.1: Range of spectral width ν covered by the 25 time series in each subgroup.

4.2 Analysis Results – Unimodal Seas

The following graphs and tables present the results obtained by analyzing eight subgroups of 25 time series from seas characterized as unimodal. The analyses are grouped into three subject areas:

- Joint distribution of wave heights and periods.
- Marginal distribution of wave heights.
- Distribution of extreme wave heights.

A narrative describing the analysis methods and plot features accompanies each set of results.

In describing use of the Waverider data, the distinction between dimensional wave height and period and their normalized counterparts must be kept clear. The dimensional heights and periods have units of meters and seconds and are represented by H and τ respectively. Heights from each time series are normalized based on the energy of that time series' spectrum,

$$R = \frac{H}{\sqrt{8m_0}} \tag{4.1}$$

where R is the non-dimensional, normalized height. Periods are normalized by the mean period of the spectrum,

$$T = \tau \frac{m_1}{2\pi m_0} \tag{4.2}$$

where T is the non-dimensional, normalized period. These normalizations are carried out for each time series individually. This allows time series with different energies and mean periods to be compared using the same theoretical distributions of normalized wave height and period.

Wave heights and periods described in the text are normalized unless otherwise noted.

4.2.1 Joint Distribution of Wave Heights and Periods

Description of Analyses

Three plots are shown for each subgroup. In the first of these plots, the height and period of each wave are plotted as a point in the T, R plane. The domain of this plot is

restricted to $T \in (0, 2.5)$, $R \in (0, 3)$ to provide uniformity and to allow for comparison of different plots. Most waves will fall inside this domain but some may fall outside and would not be shown here.

The other two panels show the contours of the observed and theoretical joint distributions of wave heights and periods, $p(R, T)$. The theoretical density is shown using the six contour values

$$(0.99, 0.9, 0.7, 0.5, 0.3, 0.1) \times p_{t,max}$$

where $p_{t,max}$ is the value of the theoretical density at its mode

$$p_{t,max} = 0.415(\nu + 1/\nu)L(\nu) \tag{4.3}$$

$$L(\nu) = \frac{2\sqrt{1+\nu^2}}{1+\sqrt{1+\nu^2}} \tag{4.4}$$

using the spectral width appropriate for the subgroup under consideration. The mode is always located near $(R, T) = (1, 1)$. Its density, $p_{t,max}$, is shown.

The observed distribution is determined by dividing the domain into bins of width $\delta T = \delta R = 0.1$ and counting the number of waves, N_i, in each bin. This is converted to an estimate of the probability density using

$$\tilde{p}(R_i, T_i) = \frac{N_i}{M\,\delta T\,\delta R} \tag{4.5}$$

where

$$M = \sum_i N_i \tag{4.6}$$

is the total number of waves.

Contours are plotted for the values of probability density

$$(0.99, 0.9, 0.7, 0.5, 0.3, 0.1) \times p_{o,max}$$

where $p_{o,max}$ is the value of the observed density at its mode. The value of $p_{o,max}$ and the location of the mode are shown.

It is seen that the mode of the observed density is located much closer to the origin than is the mode of the theoretical density. To allow the theoretical and observed densities to be compared in the region of the theoretical mode, the largest value of the observed density in the vicinity of $(R, T) = (1, 1)$ is shown.

The theoretical density decreases monotonically moving outward from the mode so the sequence of the contour lines is unambiguous. The observed density may have local maxima and minima other than the mode. To eliminate confusion, a cross (+) is placed inside any closed contour which encloses a local maximum.

Discussion of Results

The scatter plot is useful for displaying the general shape of the observed density. In regions of high probability, density gradients and extrema are difficult to interpret, but the outline of the distribution, i.e., the contour outside which few waves fall, is readily apparent.

The outline of the theoretical distribution shows two features common to all spectral widths. The smallest waves have the shortest periods and the largest waves have normalized periods near unity.

At the smaller spectral widths, the scatter plots in Figure 4-2 do show this general shape. This agreement becomes worse with increasing spectral width. The concentration near unity of periods of the highest waves is practically nonexistent for $\bar{\nu}$ of 0.4500 and above, with the highest waves having a broad range of periods. For all but the narrowest spectra, there are more short period waves of all heights than expected. Only the minimum wave height for each period, the lower edge of the outline of the distribution, remains in close agreement with theory for all spectral widths.

The contour plot provides information about the mode and gradients of the observed density. The theoretical density predicts a mode near $(R,T) = (1,1)$ for all spectral widths. The density value at the mode, $p_{t,max}$, decreases with increasing ν.

The modes of the observed densities are not located near $(R,T) = (1,1)$, but are much closer to the origin. This indicates an excess of small amplitude, short period waves not predicted by narrow-band theory. The value of the density at the mode, $p_{o,max}$, shows an increasing trend with spectral width, unlike the behavior of the theoretical mode.

The observed density of the subgroup with $\nu = 0.2999$, shown in Figure 4-2 (a2), does show a local maximum near the location of the theoretical mode. The value of the density $p = 1.69$ at this local maximum is within 10% of the density of the theoretical mode,

$p_{t,max} = 1.54$. To investigate the behavior of the observed densities in the vicinity of their theoretical modes, the largest value of each of the observed densities in the vicinity of $(R,T) = (1,1)$ is shown. This value decreases as width increases and remains within 10% of the theoretical value (except for the subgroup in Figure 4-2 (h2) with $\nu = 0.6499$ where the difference is 16%).

This indicates that the density of waves with heights and periods near $(R,T) = (1,1)$ agrees with that given by narrow-band theory. This is not the mode of the observed density because of the large number of short, small amplitude waves observed.

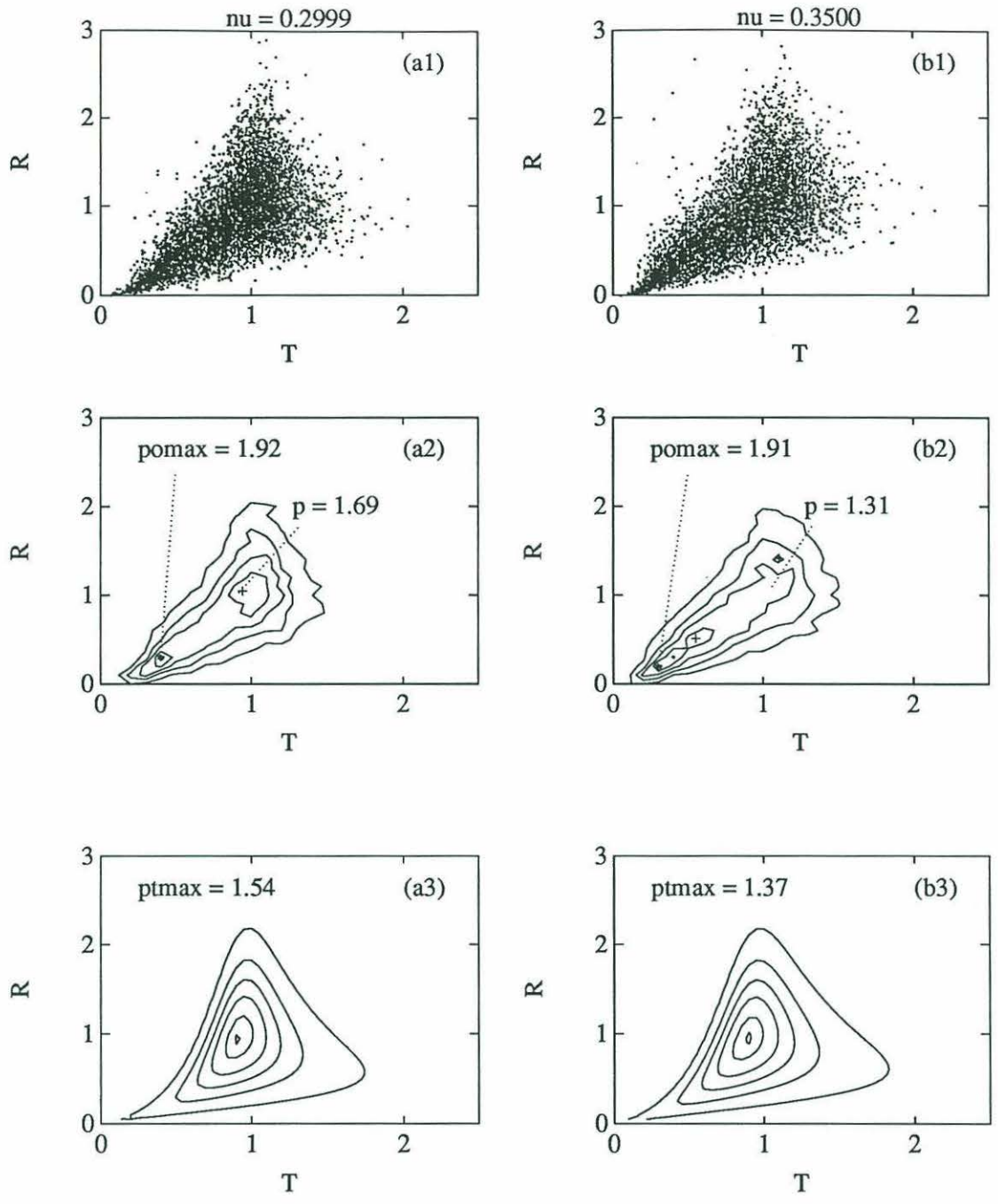

Figure 4-2: Unimodal Seas: Joint Distribution of Wave Heights and Periods. In the scatter plot, each point represents the normalized height and period of one wave. The contour plots show contours of the theoretical and observed joint density, $p(R,T)$. Contours are shown for values of $(0.99, 0.9, 0.7, 0.5, 0.3, 0.1) \times p_{max}$. Local maxima are identified by crosses (+). The value of p_{max} is given for the theoretical and observed densities and the location of the mode of the observed density is shown. The largest value of the observed density in the vicinity of $(R,T) = (1,1)$ is also shown. (a) $\bar{\nu} = 0.2999$, (b) $\bar{\nu} = 0.3500$.

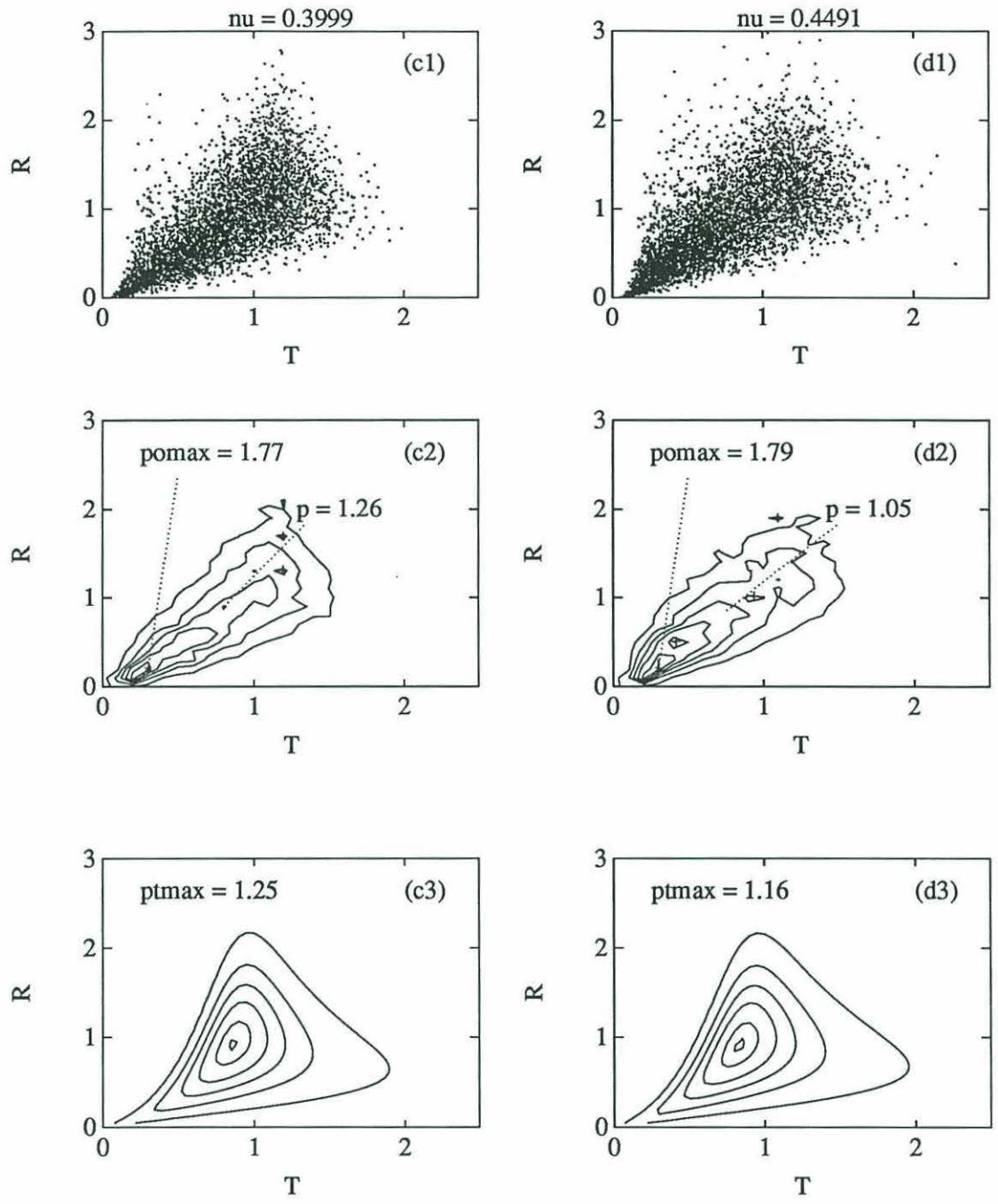

Figure 4-2: (continued). (c) $\bar{\nu} = 0.3999$, (d) $\bar{\nu} = 0.4491$.

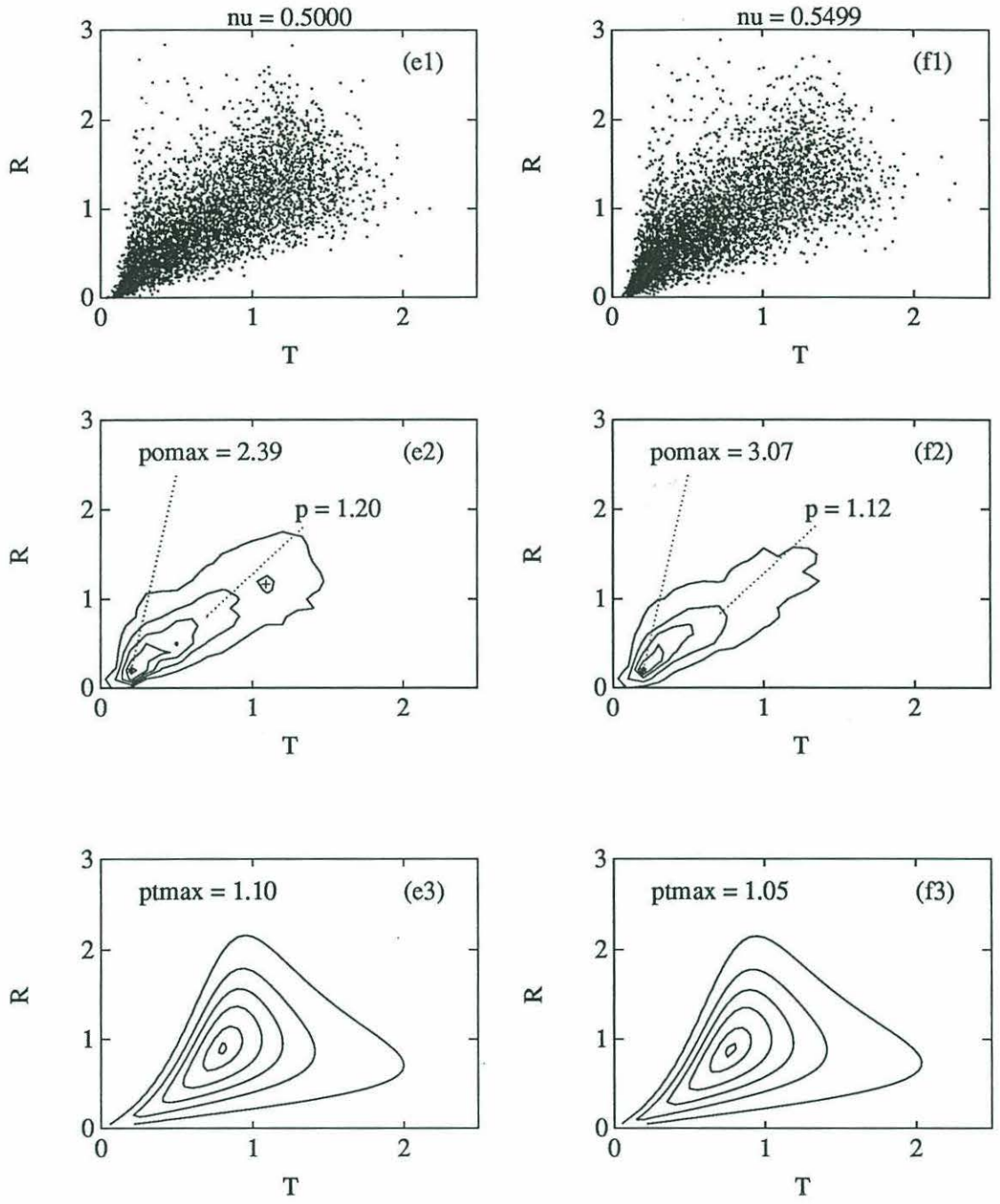

Figure 4-2: (continued). (e) $\bar{\nu} = 0.5000$, (f) $\bar{\nu} = 0.5499$.

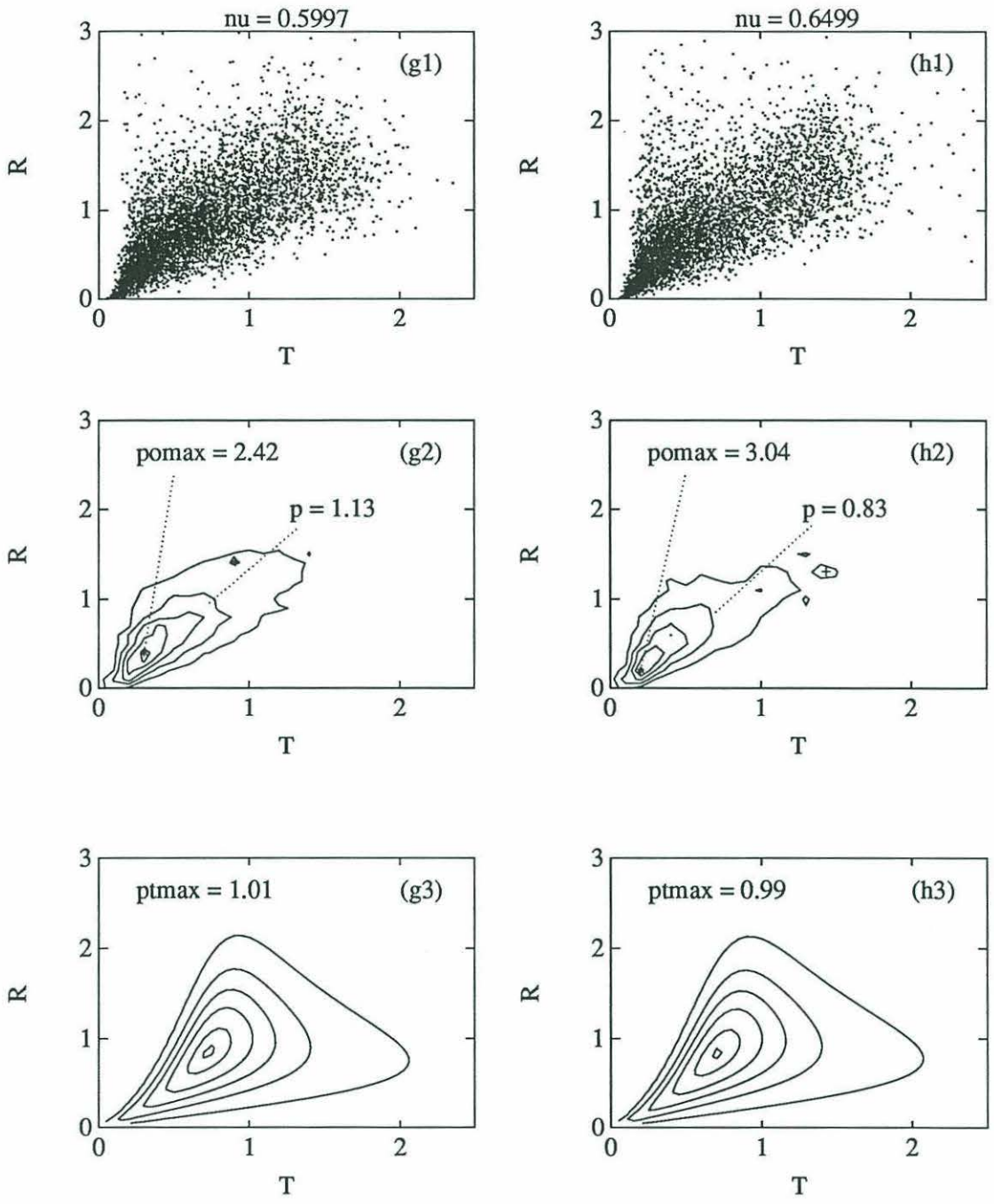

Figure 4-2: (continued). (g) $\bar{\nu} = 0.5997$, (h) $\bar{\nu} = 0.6499$.

4.2.2 Marginal Distribution of Wave Heights

Description of Analyses

The observed density of wave heights for each subgroup is plotted as a histogram. The density is determined by dividing the domain into bins of width $\delta R = 0.2$, counting the number of waves, N_i, in each bin, and converting to a probability density

$$\tilde{p}(R_i) = \frac{N_i}{M\,\delta R} \tag{4.7}$$

where M is the total number of waves. The marginal density predicted by narrow-band theory, $p(R)$, is shown as a solid curve. The Rayleigh density is shown as a dotted curve.

The second figure for each subgroup involves the ratio of measured significant wave height to the square root of the spectral energy. This ratio, $H_s/\sqrt{m_0}$, is shown in section 2.2.10 to have an expected value approximately equal to 4.0 and to be weakly dependent on spectral width. One value of this ratio is observed for each of the 25 time series in a subgroup. Each histogram which follows shows the distribution of the observed ratios for a subgroup. The vertical scale is adjusted so the area under the histogram is unity.

The third plot for each subgroup compares the number of waves observed in each time series, N_O, to the expected number of waves, N_E, a function of the moments of the spectrum. The slope of the line passing through the origin which best fits the data points is listed and this line is superimposed.

Discussion of Results

Each histogram in Figure 4-3 has a shape which is similar to that given by narrow-band theory and by the Rayleigh distribution. The agreement is not perfect, however, and it is useful to examine the plots to determine how and where the observations differ from theory.

The smallest amplitude waves are always underpredicted. For narrow spectra, only the bin with $R_i = 0.1$ is affected. As spectral width increases, more bins are affected and the number of small amplitude waves observed increases significantly. For $\bar{\nu} = 0.6499$, normalized wave heights up to $R = 0.6$ are underpredicted. This observation is consistent

with the abnormally high probability values near the origin of the joint density of wave heights and periods.

The significant wave height is controlled by the region of the marginal density where $R > 1.4$. The observed and theoretical densities agree well in this region for the narrow spectra. For wider spectra, $\bar{\nu} \geq 0.5499$, there are fewer waves here than expected. This agrees with the observation that there are too many small amplitude waves.

The extreme tail of the distribution describes the largest amplitude waves and is of interest. Waves with amplitudes $R > 2.6$ are overpredicted for $\bar{\nu} \leq 0.5000$ and underpredicted for $\bar{\nu} \geq 0.5499$.

In summary, the agreement between the observed and theoretical distributions becomes worse with increasing spectral width. For the widest spectra, there are more small and large amplitude waves and fewer medium amplitude waves than expected.

The preceding discussion has been qualitative. A rigorous chi-square test can be used to quantify the goodness-of-fit of the theoretical distributions to the data. It provides two important results. First, the Rayleigh distribution provides a better fit to the data than does the density $p(R)$ given by narrow-band theory. This holds true for every spectral width. Yet this fit is seldom good enough to satisfy the chi-square test at the 0.00001 level of significance. This level of significance means that the chi-square test would reject the correct distribution in only 0.001% of all realizations. This broad acceptance of correct hypotheses causes the test to be more likely to accept an incorrect distribution as well. The low level of significance indicates a reduced ability to discriminate among competing distributions. Despite this insensitivity, at the level given, the test would reject the density given by narrow-band theory for all spectral widths. The fit of the Rayleigh density would be acceptable (at this level) only for the subgroup with $\bar{\nu} = 0.3500$ shown in Figure 4-3 (b1).

A detailed discussion of using chi-square statistics to evaluate goodness-of-fit is given in Hald (1952, pp. 739–755).

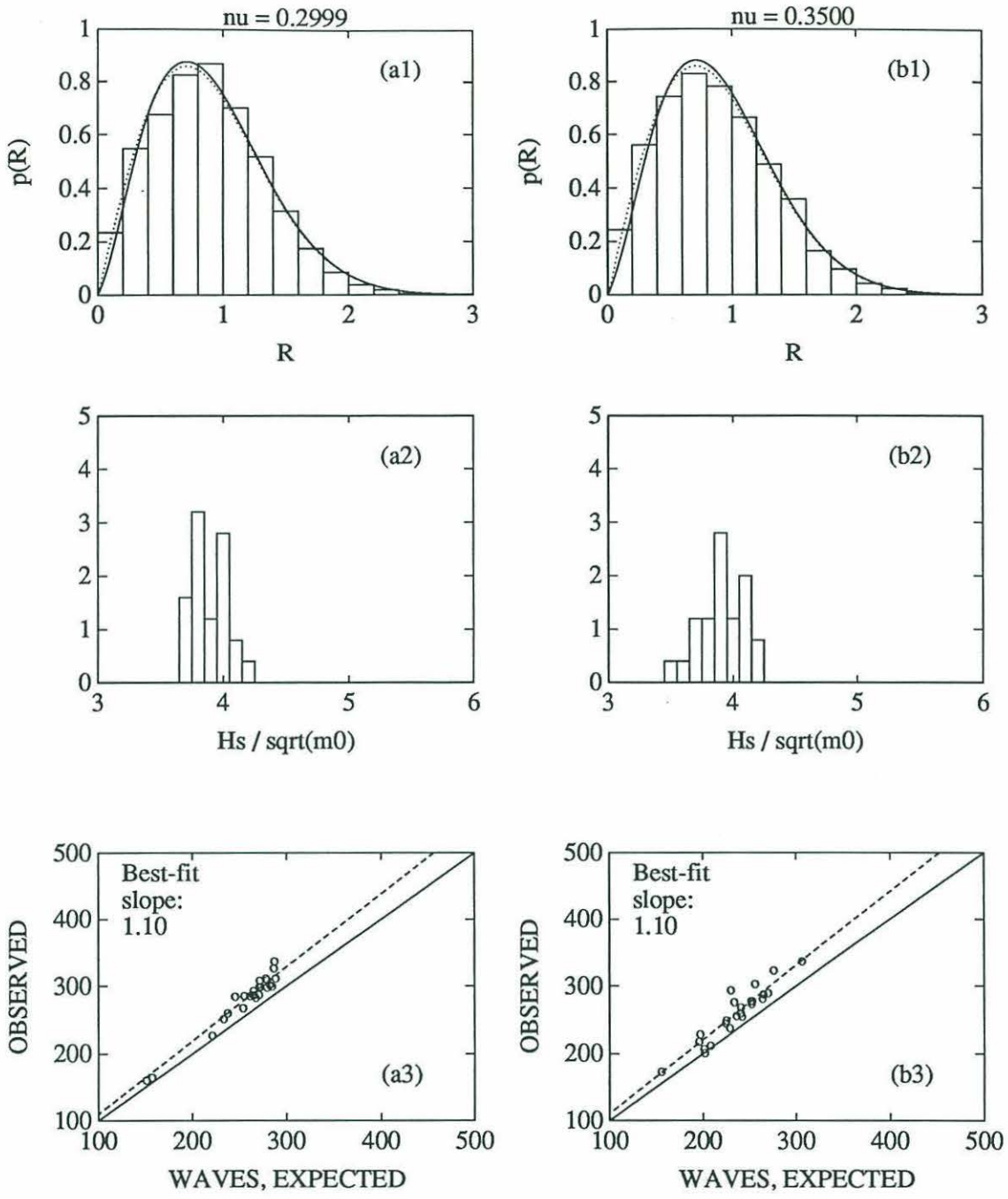

Figure 4-3: Unimodal Seas: Distribution of Wave Heights. Upper histogram shows the observed density of wave heights. The distribution given by narrow-band theory is shown as a solid curve. The Rayleigh distribution is the dotted curve. Middle histogram shows the distribution of the ratio $H_s/\sqrt{m_0}$. This ratio is displayed on the horizontal axis and its frequency of occurrence on the vertical axis. Each circle in the lower plot shows the expected and observed number of waves during one time series. The slope is given for the line passing through the origin that best fits the data. (a) $\bar{\nu} = 0.2999$, (b) $\bar{\nu} = 0.3500$.

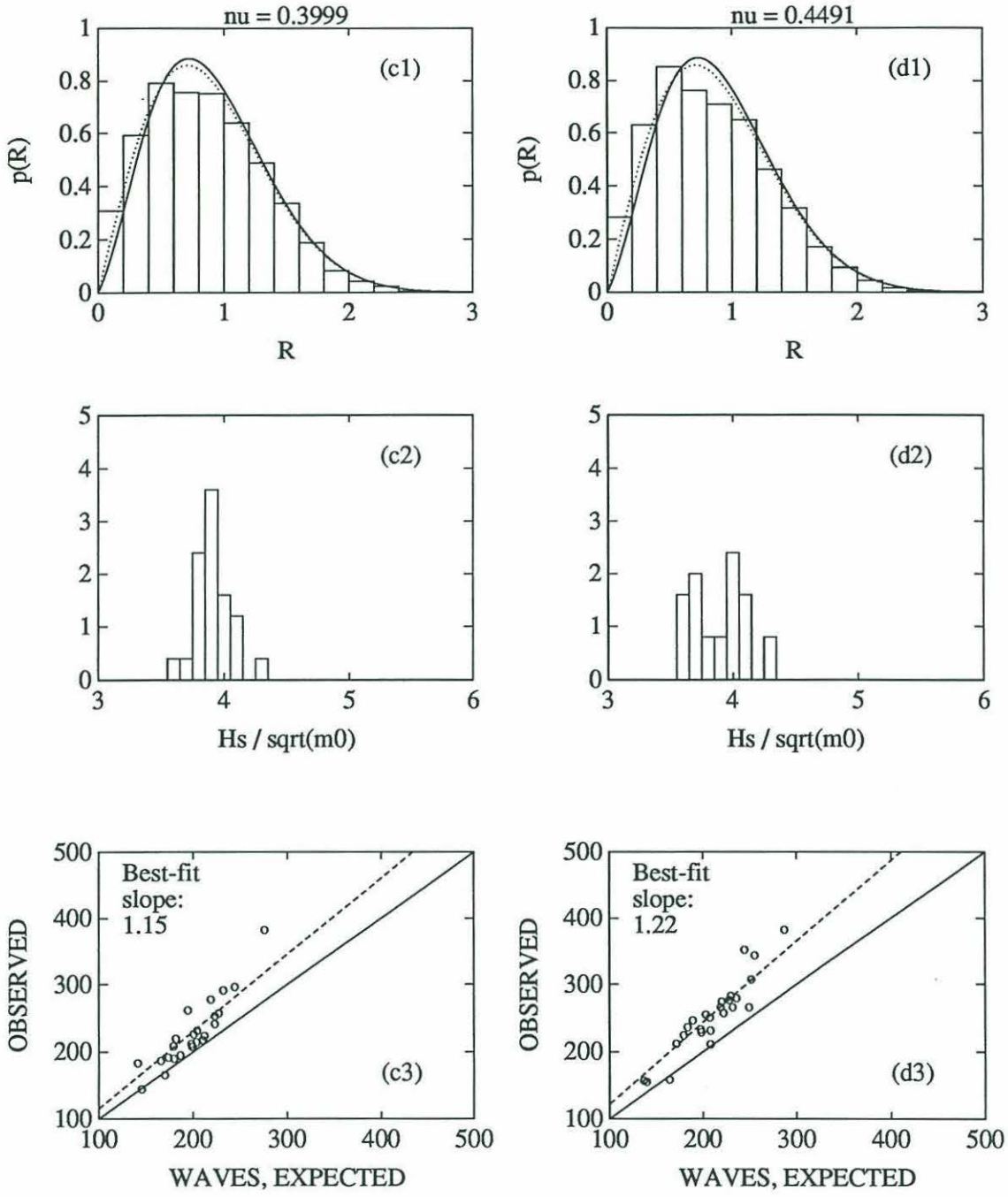

Figure 4-3: (continued). (c) $\bar{\nu} = 0.3999$, (d) $\bar{\nu} = 0.4491$.

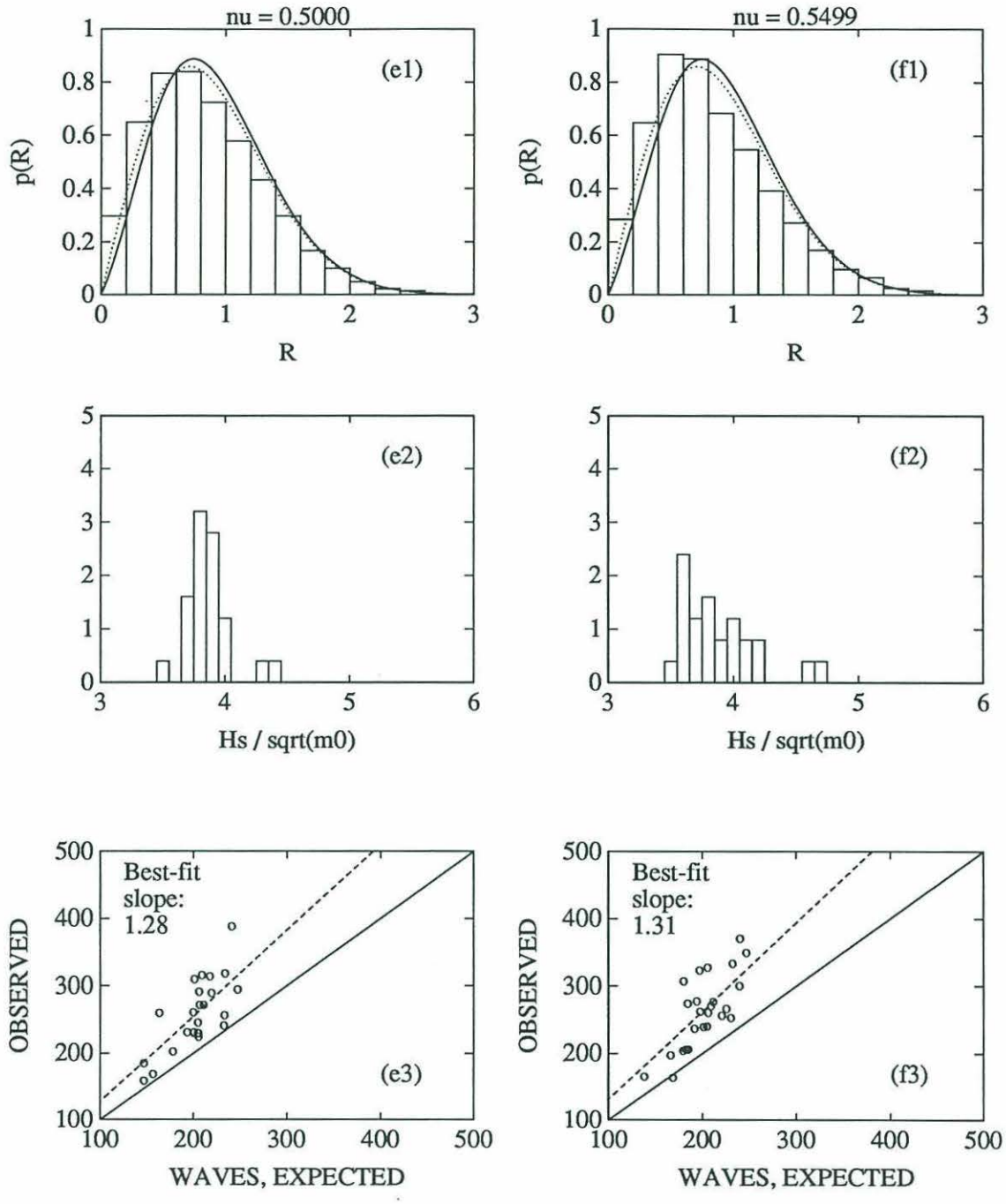

Figure 4-3: (continued). (e) $\bar{\nu} = 0.5000$, (f) $\bar{\nu} = 0.5499$.

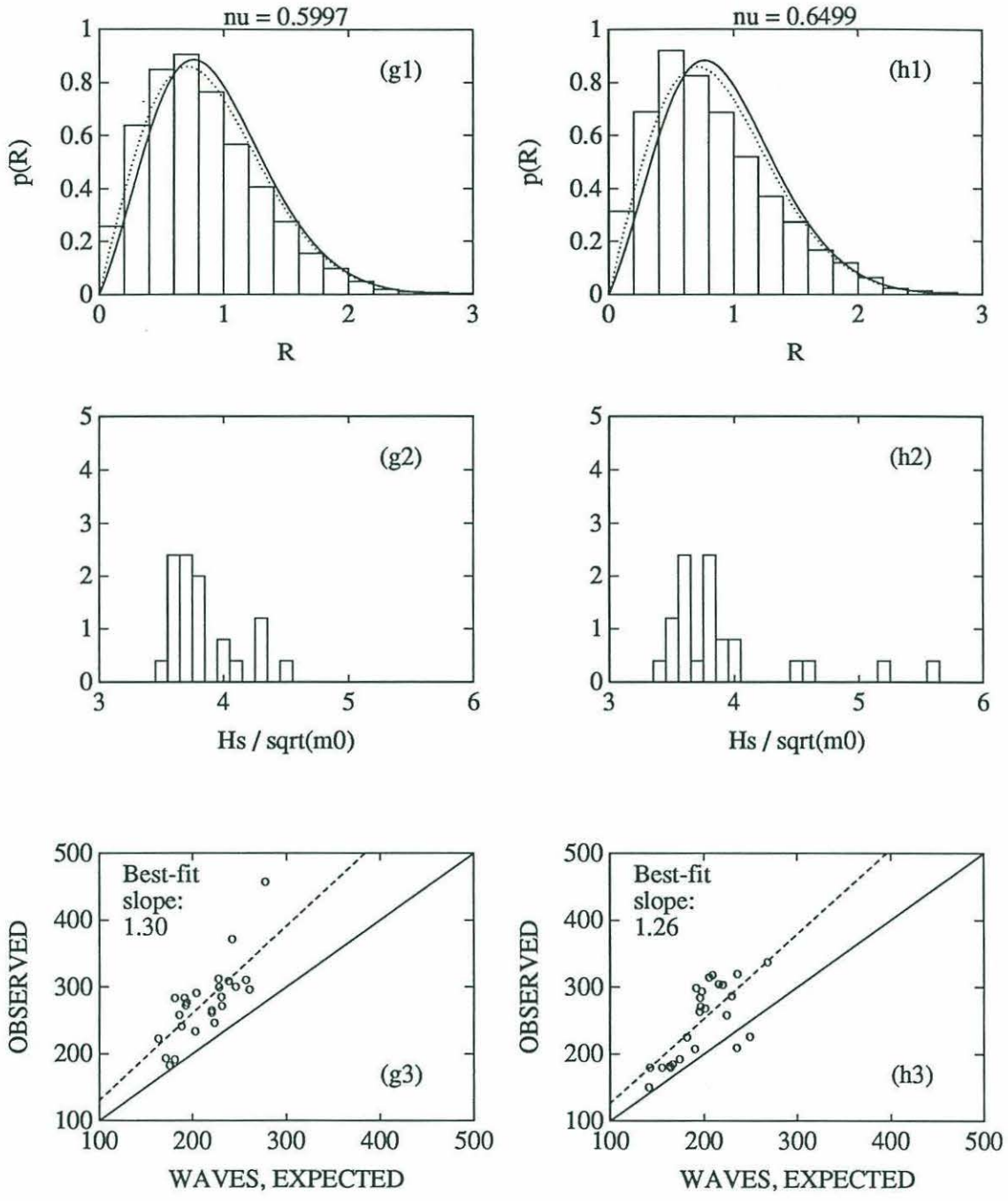

Figure 4-3: (continued). (g) $\bar{\nu} = 0.5997$, (h) $\bar{\nu} = 0.6499$.

Unimodal Seas

$\bar{\nu}$	Mean of $(H_s/\sqrt{m_0})$	Standard Deviation of $(H_s/\sqrt{m_0})$	Mean of (N_O/N_E)	Standard Deviation of (N_O/N_E)
0.2999	3.887	0.130	1.09	0.036
0.3500	3.916	0.177	1.10	0.060
0.3999	3.911	0.130	1.14	0.110
0.4491	3.885	0.223	1.20	0.104
0.5000	3.877	0.186	1.27	0.171
0.5499	3.891	0.298	1.30	0.188
0.5997	3.836	0.271	1.30	0.164
0.6499	3.912	0.529	1.26	0.187

Table 4.2: Unimodal Seas: Statistics of Significant Wave Height and Number of Waves. Statistics of the ratios $H_s/\sqrt{m_0}$ and N_O/N_E.

The significant wave height histograms provide additional insight into the behavior of the largest one-third wave heights. Table 4.2 gives the mean and standard deviation of the ratio $H_s/\sqrt{m_0}$ for each subgroup. For narrow spectra, the significant wave height ratios are approximately equal for all time series. As spectral width increases, the mean of the ratio rises slightly but the dominant trend is the increase in standard deviation. For the wide spectra, most of the ratios fall below 4.0 but some take values considerably higher.

At narrow spectral widths, the 25 time series in a subgroup all have significant wave heights close to that predicted by narrow-band theory. For wide spectra, the significant wave heights for seas with the same spectral width may differ markedly.

Several observations may be made about the number of waves in a time series. There are almost always more waves than expected. This may be expressed as the ratio of the number of waves observed, N_O, to the number expected, N_E. The mean and standard deviation of this ratio are listed in Table 4.2. The mean of this ratio increases from 1.1 at $\bar{\nu} = 0.2999$ to approximately 1.3 at $\bar{\nu} = 0.6499$. This trend is consistent with the earlier observation that the number of short period waves is greater than expected and increases with spectral width.

The scatter about the mean also varies with width. For narrow spectra, the ratios for the individual time series are all near the mean. The ratios for time series with wider spectra show considerable variation about the mean.

4.2.3 Distribution of Extreme Wave Heights

Description of Analyses

These plots provide information about the height and period of the highest wave from each time series. Three plots are shown for each subgroup.

The first plot is a scatter plot of wave height and period. Its domain is limited to wave heights $R > 1.517$, the region where the highest 10% of the waves are expected. Quartiles of the conditional distribution of wave periods, $p(T|R)$, are shown. Half of the waves are expected to have periods which fall between the two outer quartiles, Q_1 and Q_3. The fraction of the waves which do fall in the interquartile range is shown as a percentage in the corner of the plot. The point representing the extreme wave in each time series is circled.

In the second plot, each circle represents the normalized height of the highest wave in one time series, plotted against the observed number of waves in the series. The expected value of the extreme wave and the $\pm 2\sigma$ bounds (from Table 2.1) are superimposed. They are functions of the number of waves in the time series.

The third plot shows the normalized period of the highest wave in each time series, plotted against the wave height. The quartiles of $p(T|R)$ are superimposed.

Discussion of Results

The upper plate in Figure 4-4 shows the distribution of the heights and periods of the largest waves. For narrow spectra, the periods are concentrated near $T = 1$ and approximately half fall in the interquartile range, as expected. As width increases, more wave periods fall above and below this range.

The mean value of the extreme wave height is slightly less than expected for spectral widths up to $\bar{\nu} = 0.5499$. Seas from subgroups with wider spectra have mean values slightly greater than expected. This behavior is consistent with the observed excess of very large waves at high widths.

More pronounced is the variance about the mean. The extreme wave heights for the narrow spectra are well contained by the $\pm 2\sigma$ bounds but the variation increases with

spectral width.

The periods of extreme waves show similar trends. The mean is just slightly higher than its expected value for narrow spectra and increases to approximately 1.3 times its expected value for the widest spectra. The scatter also increases with spectral width.

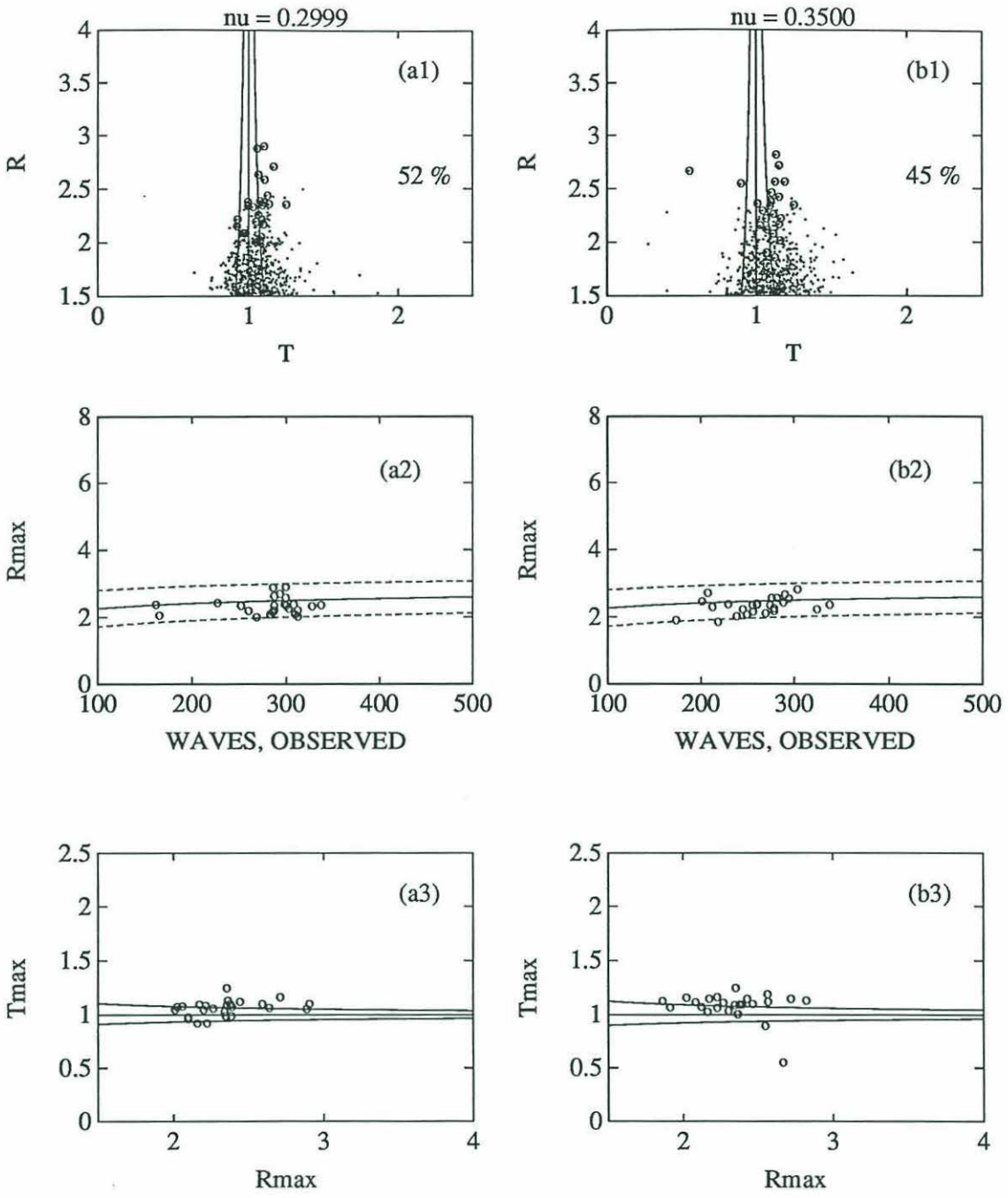

Figure 4-4: Unimodal Seas: Extreme Wave Heights and Periods. Scatter plot for the region where the highest ten percent waves are expected. Quartiles of $p(T|R)$ are superimposed; half the waves should fall between the two outermost quartiles. The number observed in this region is shown as a percentage. The extreme wave from each time series is circled. In the middle plot, the extreme wave height from each time series is plotted as a function of the observed number of waves. The expected value and $\pm 2\sigma$ bounds are shown. The lower plot shows periods of the extreme waves and quartiles of $p(T|R)$. (a) $\bar{\nu} = 0.2999$, (b) $\bar{\nu} = 0.3500$.

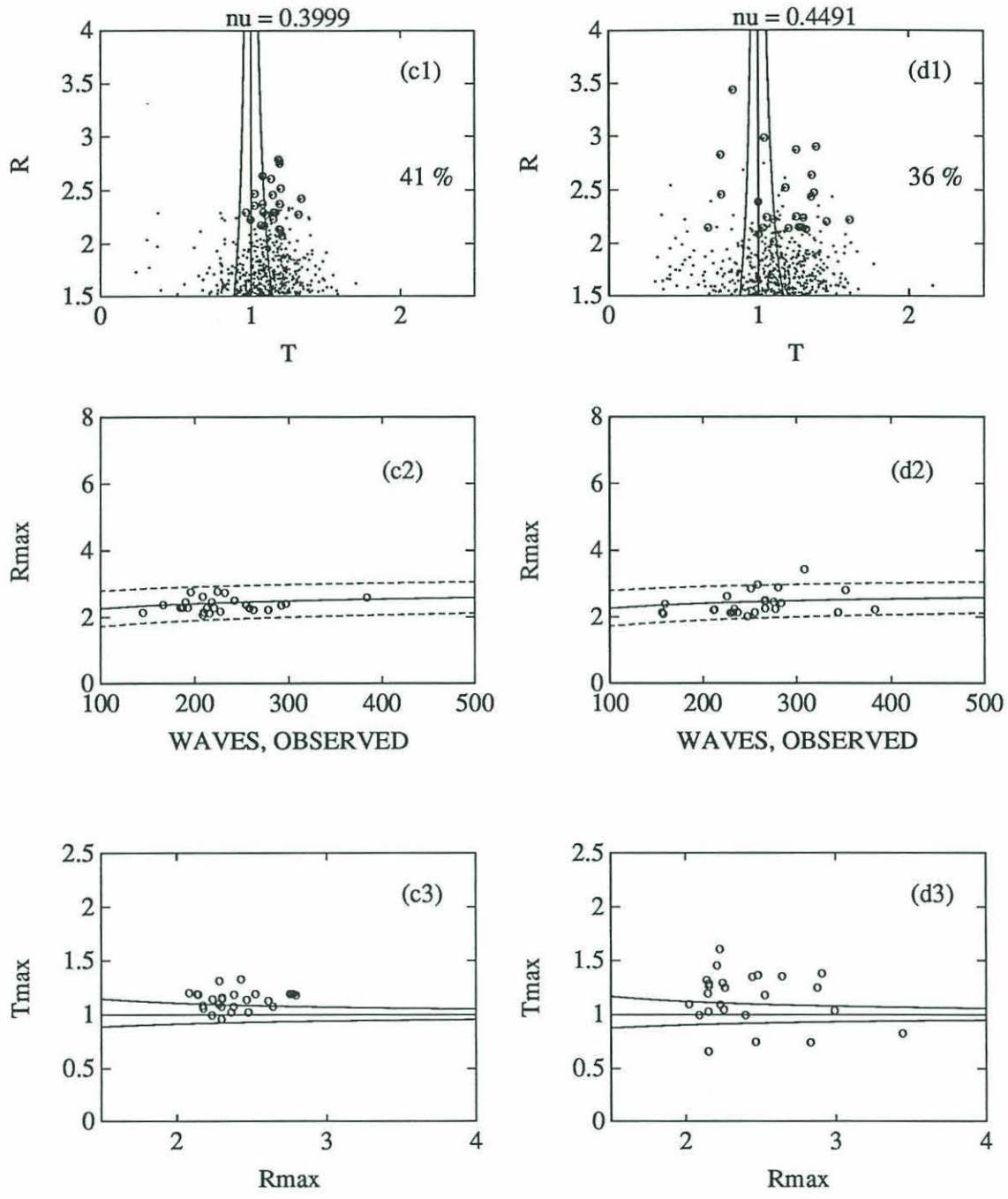

Figure 4-4: (continued). (c) $\bar{\nu} = 0.3999$, (d) $\bar{\nu} = 0.4491$.

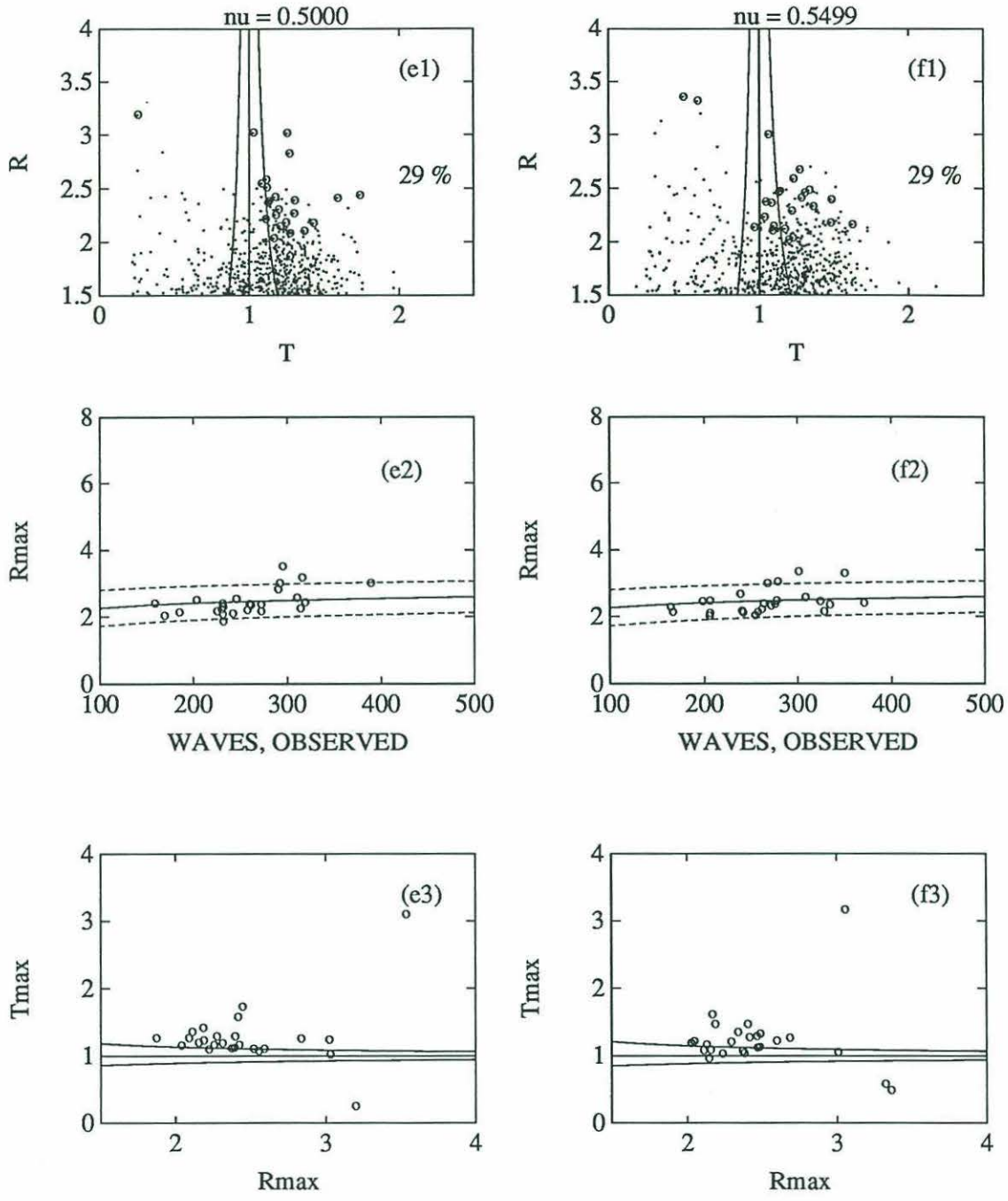

Figure 4-4: (continued). (e) $\bar{\nu} = 0.5000$, (f) $\bar{\nu} = 0.5499$.

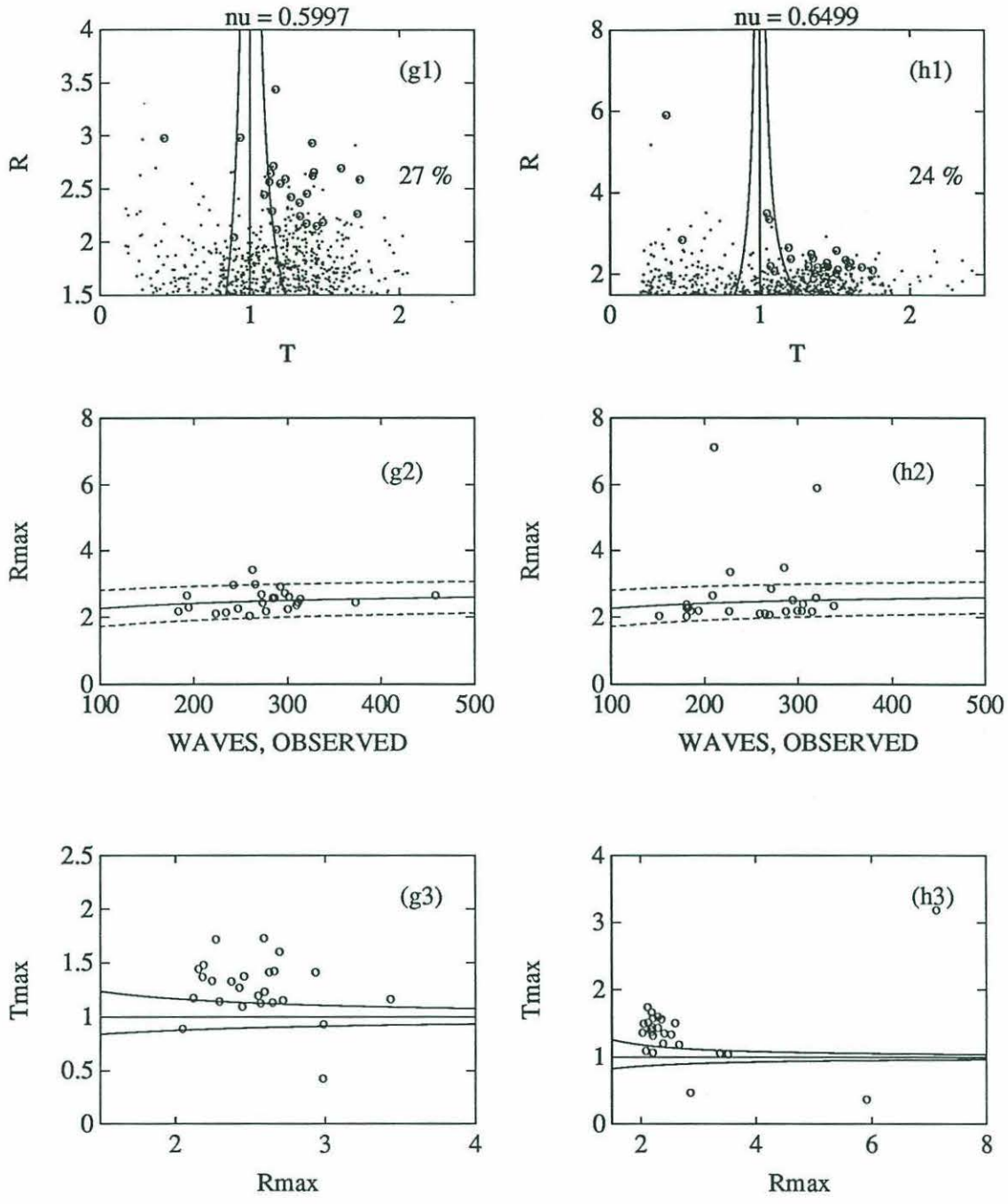

Figure 4-4: (continued). (g) $\bar{\nu} = 0.5997$, (h) $\bar{\nu} = 0.6499$.

Unimodal Seas

$\bar{\nu}$	Mean of $R_{max}/E(R_{max})$	Standard Deviation of $R_{max}/E(R_{max})$	Mean of T_{max}	Standard Deviation of T_{max}
0.2999	0.939	0.097	1.063	0.073
0.3500	0.941	0.094	1.079	0.130
0.3999	0.971	0.082	1.135	0.089
0.4491	0.977	0.136	1.154	0.236
0.5000	0.992	0.149	1.280	0.456
0.5499	0.988	0.143	1.242	0.469
0.5997	1.015	0.129	1.264	0.273
0.6499	1.101	0.491	1.380	0.500

Table 4.3: Unimodal Seas: Extreme Wave Height and Period Statistics. Statistics of the ratio of extreme wave height to its expected value, $R_{max}/E(R_{max})$, and the period, T_{max}, of the extreme wave.

Table 4.3 is provided to supplement the graphical presentation of Figure 4-4. For each subgroup, the table lists the mean and standard deviation of two quantities, the ratio of extreme wave height to its expected value, and the period of the extreme wave.

4.3 Analysis Results – Bimodal Seas

The following graphs and tables present the results obtained from analyzing nine subgroups of 25 time series from seas characterized as bimodal. Narratives describing the analysis methods and plot features are found in the previous section.

Discussions will focus on differences between the behaviors of unimodal and bimodal seas.

4.3.1 Joint Distribution of Wave Heights and Periods

Discussion of Results

The scatter plots in Figure 4-5 show some characteristics similar to those for unimodal seas. For narrow spectra, the outline of the scatter plot matches the shape of the theoretical density. As spectral width increases, periods of the highest waves become scattered and deviate from unity. These features are also observed for unimodal seas.

As the contour plots show, the theoretical mode near $(R,T) = (1,1)$ is not observed

in the data, although local maxima are visible there in Figure 4-5 (a2, c2, and e2). The observed mode is located closer to the origin, but not as close as for the unimodal seas. The density value at the observed mode increases with ν, but the increase is not as pronounced as for unimodal seas.

The maximum observed density in the vicinity of $(R,T) = (1,1)$ does not track the value of the theoretical mode, as it did for unimodal seas. Bimodal seas with $0.4000 \leq \nu \leq 0.5500$ show more waves with heights and periods near $(R,T) = (1,1)$ than theory predicts and more than were observed for unimodal seas.

The most probable wave for bimodal seas of all widths has a smaller height and shorter period than the most probable wave given by theory. It is slightly larger and has a longer period than its unimodal counterpart.

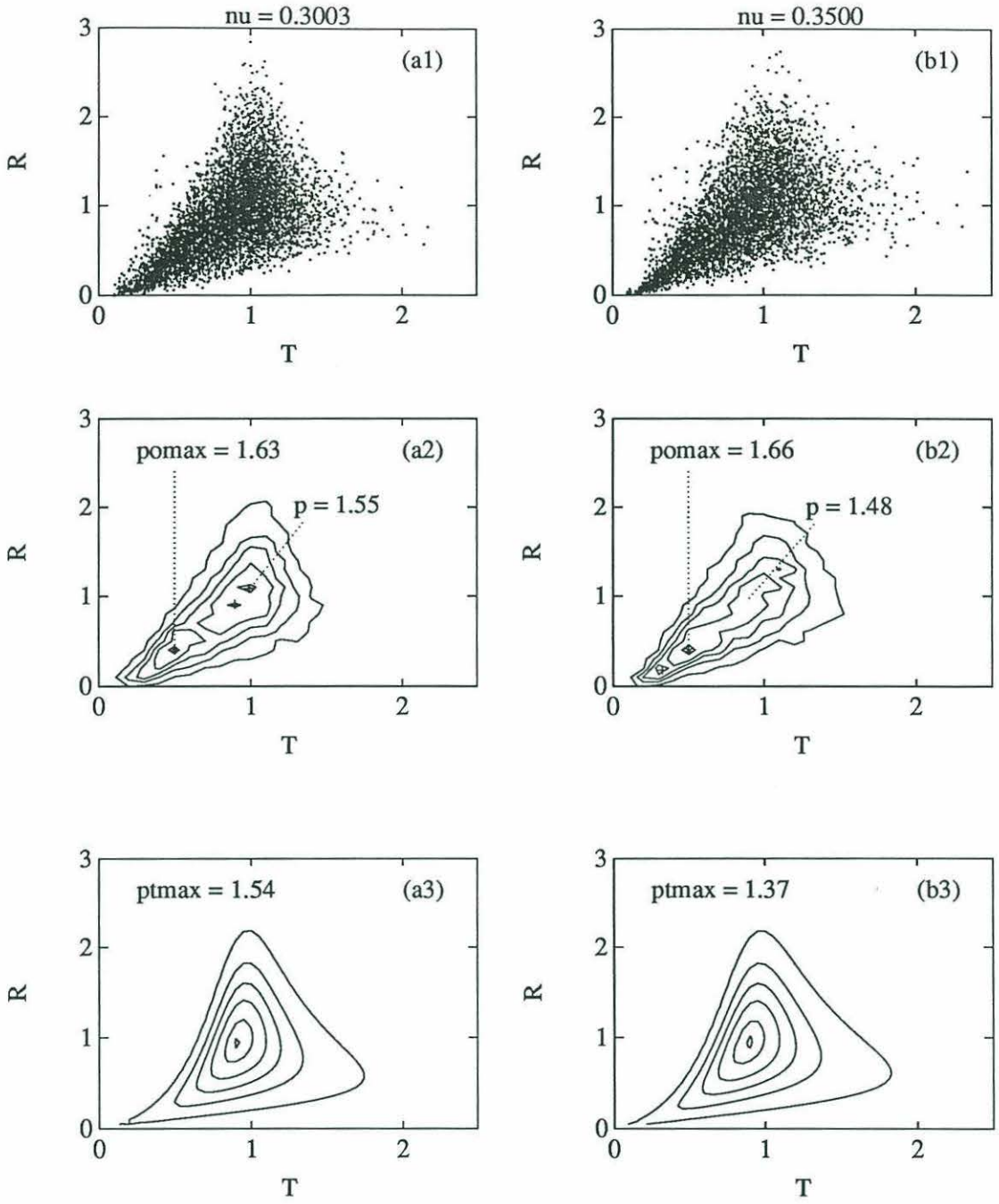

Figure 4-5: Bimodal Seas: Joint Distribution of Wave Heights and Periods. In the scatter plot, each point represents the normalized height and period of one wave. The contour plots show contours of the theoretical and observed joint density, $p(R,T)$. Contours are shown for values of $(0.99, 0.9, 0.7, 0.5, 0.3, 0.1) \times p_{max}$. Local maxima are identified by crosses (+). The value of p_{max} is given for the theoretical and observed densities and the location of the mode of the observed density is shown. The largest value of the observed density in the vicinity of $(R,T) = (1,1)$ is also shown. (a) $\bar{\nu} = 0.3003$, (b) $\bar{\nu} = 0.3500$.

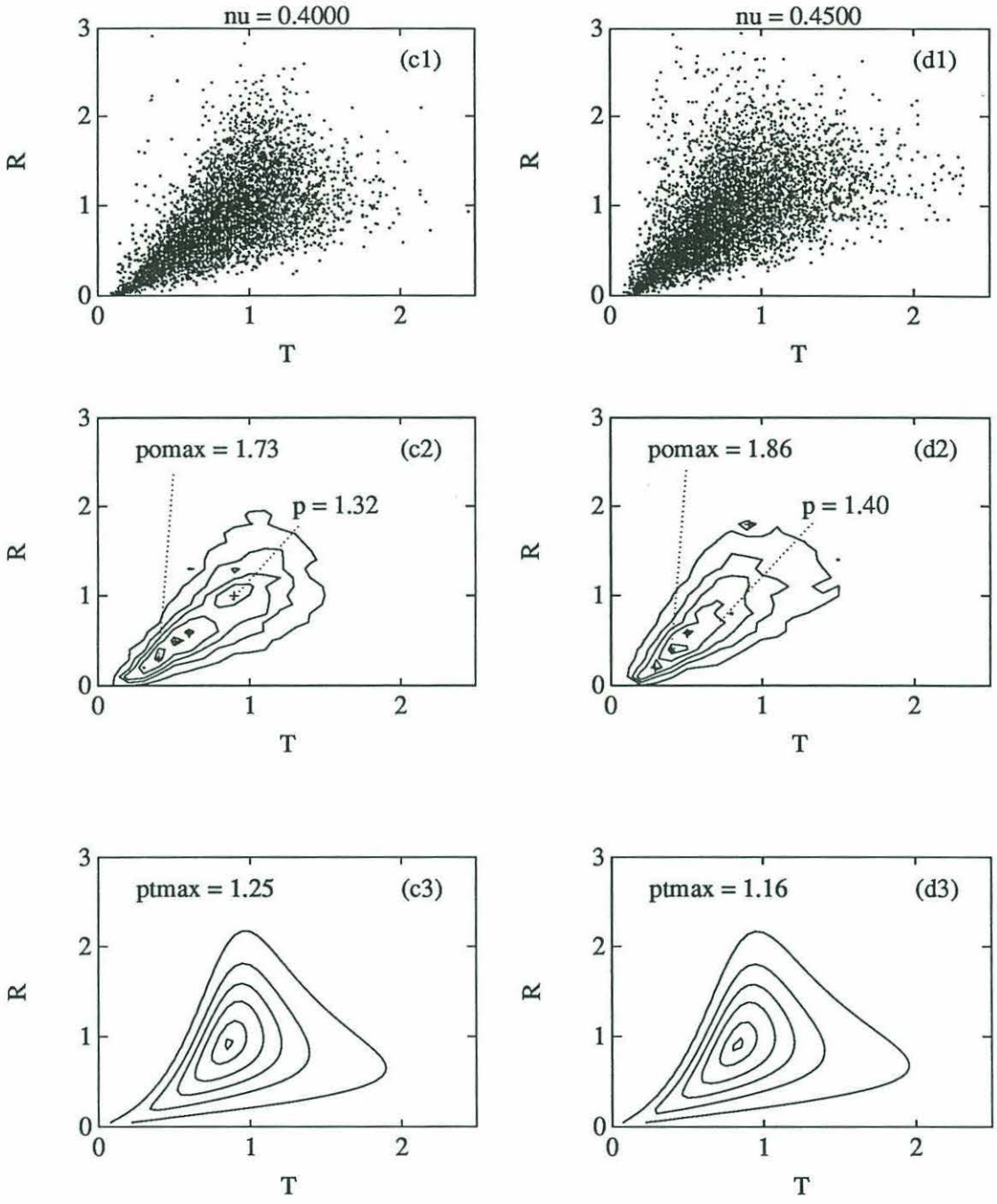

Figure 4-5: (continued). (c) $\bar{\nu} = 0.4000$, (d) $\bar{\nu} = 0.4500$.

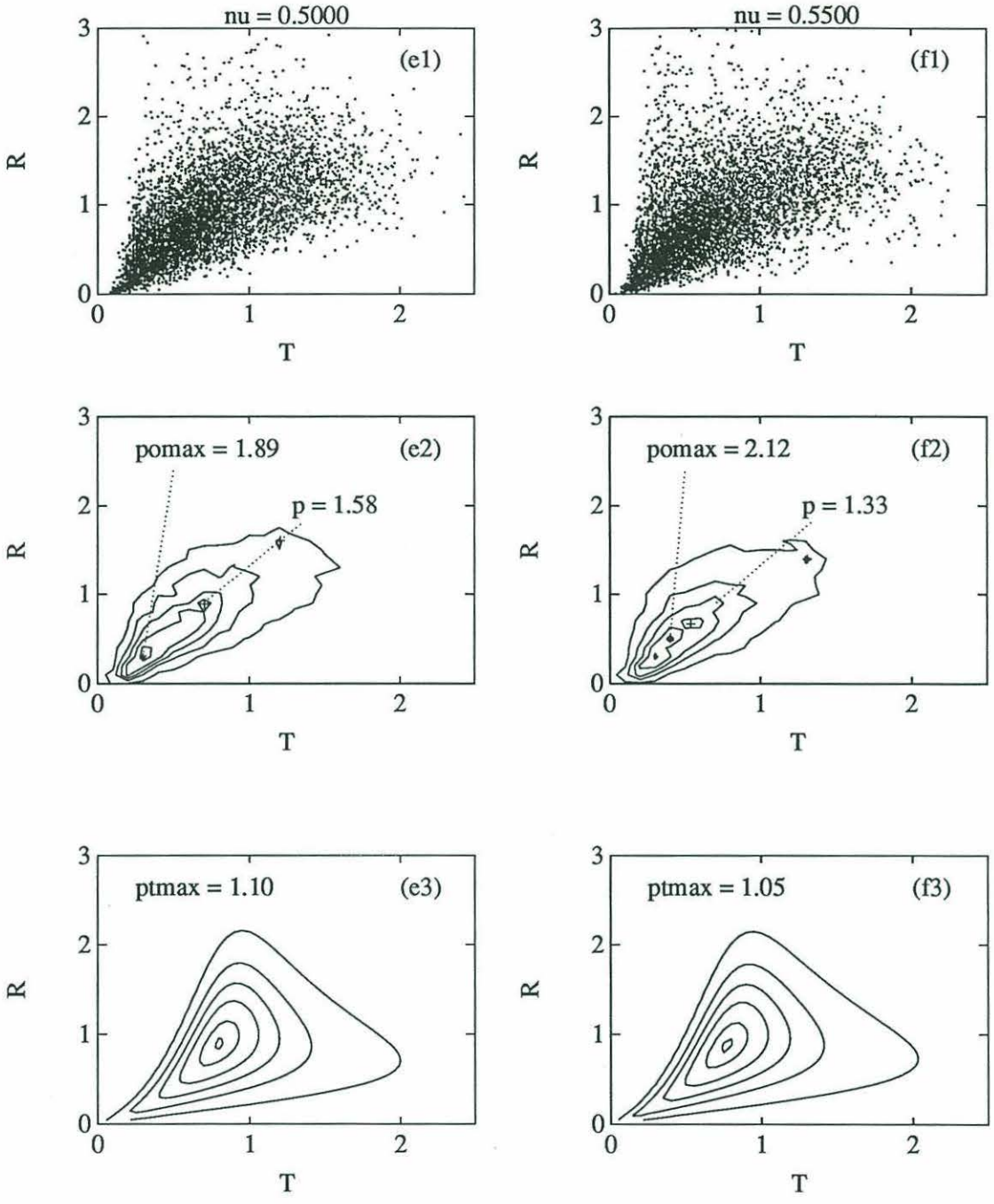

Figure 4-5: (continued). (e) $\bar{\nu} = 0.5000$, (f) $\bar{\nu} = 0.5500$.

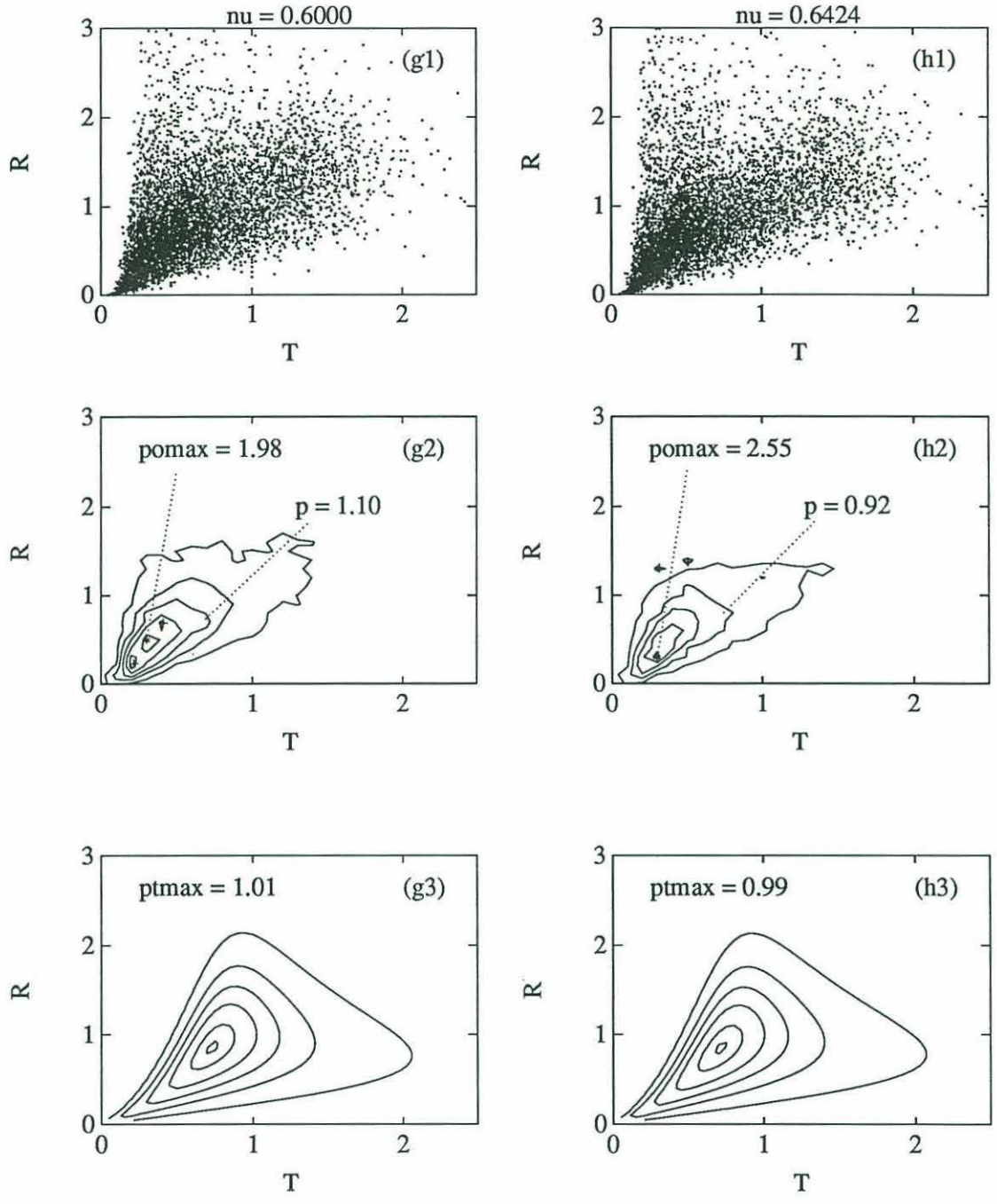

Figure 4-5: (continued). (g) $\bar{\nu} = 0.6000$, (h) $\bar{\nu} = 0.6424$.

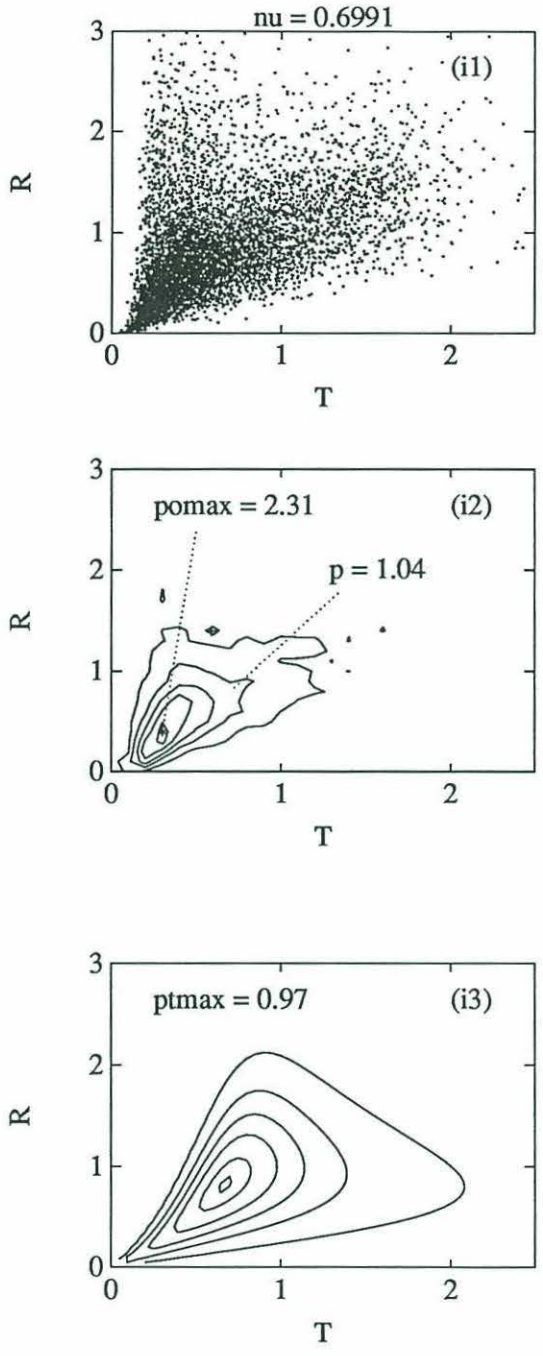

Figure 4-5: (continued). (i) $\bar{\nu} = 0.6991$.

4.3.2 Marginal Distribution of Wave Heights

Discussion of Results

The observed number of small amplitude waves always exceeds the expected number predicted by narrow-band theory. For bimodal seas, more histogram bins in Figure 4-6 show this excess than for unimodal seas of the same spectral width. In the subgroup with $\bar{\nu} = 0.3500$, there are more waves with heights up to $R = 0.4$ than expected. In the subgroups with $\bar{\nu}$ from 0.4000 to 0.5500, wave heights up to $R = 0.6$ are affected, and for $\bar{\nu} \geq 0.6000$, this extends to $R = 0.8$.

The excess number of waves of small amplitude is balanced by a net deficit at moderate to large amplitudes. For small spectral widths, there are fewer waves than expected from the mode through the tail of the distribution. For $\bar{\nu} \geq 0.4500$, this deficit continues except for a surplus of the largest amplitude waves. For these subgroups, the smallest and largest waves are underpredicted and those with amplitudes in between are overpredicted.

A chi-square analysis shows that the Rayleigh distribution always provides a better fit to the observed wave height density than does the marginal wave height density given by narrow-band theory. This fit is seldom good enough to satisfy the chi-square test at the 0.00001 level of significance. At this level, the test would reject the density given by narrow-band theory for all spectral widths. At the same level, the fit of the Rayleigh density would be acceptable only for the subgroups with $\bar{\nu} = 0.4000$ and 0.4500.

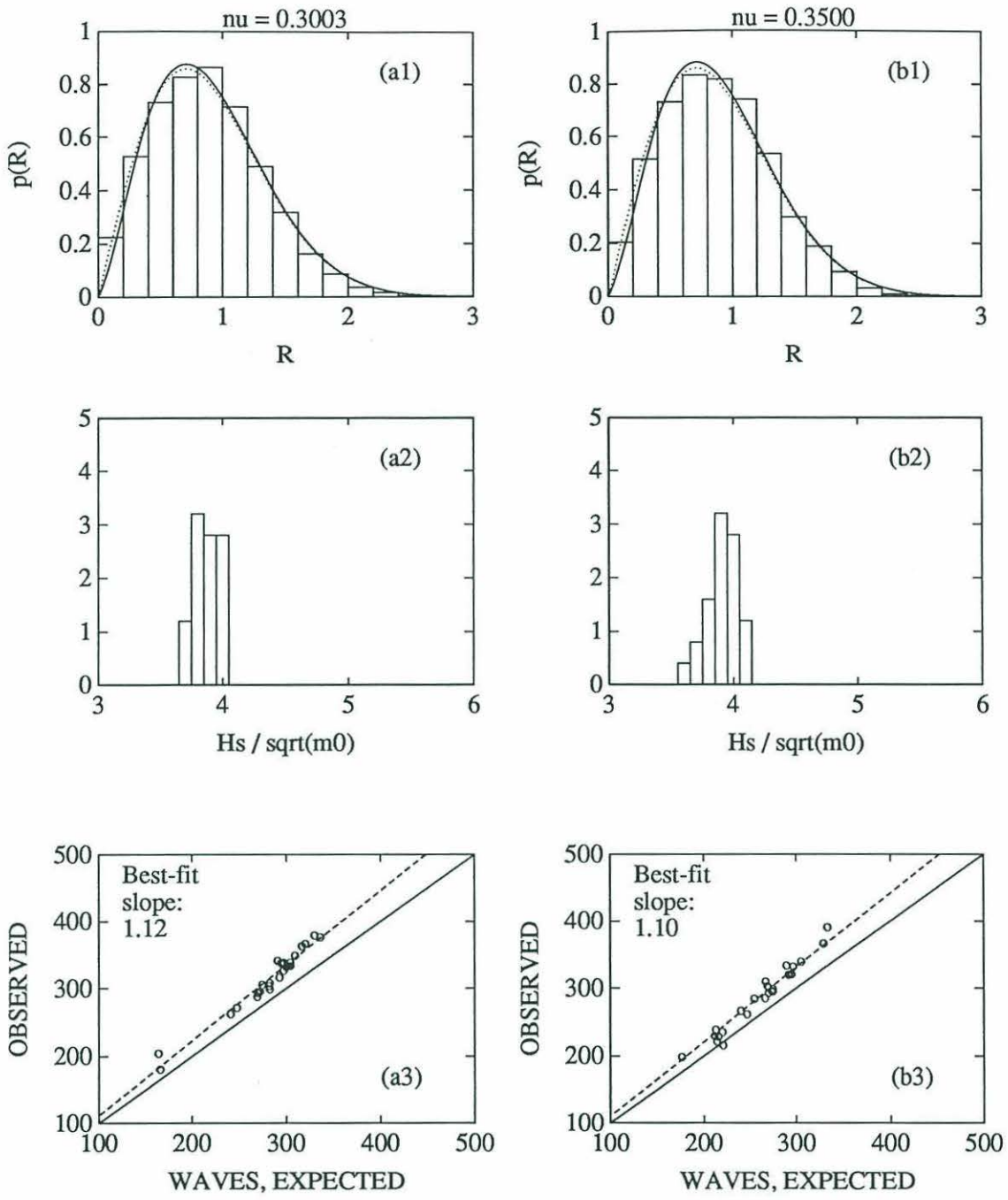

Figure 4-6: Bimodal Seas: Distribution of Wave Heights. Upper histogram shows the observed density of wave heights. The distribution given by narrow-band theory is shown as a solid curve. The Rayleigh distribution is the dotted curve. Middle histogram shows the distribution of the ratio $H_s/\sqrt{m_0}$. This ratio is displayed on the horizontal axis and its frequency of occurrence on the vertical axis. Each circle in the lower plot shows the expected and observed number of waves during one time series. The slope is given for the line passing through the origin that best fits the data. (a) $\bar{\nu} = 0.3003$, (b) $\bar{\nu} = 0.3500$.

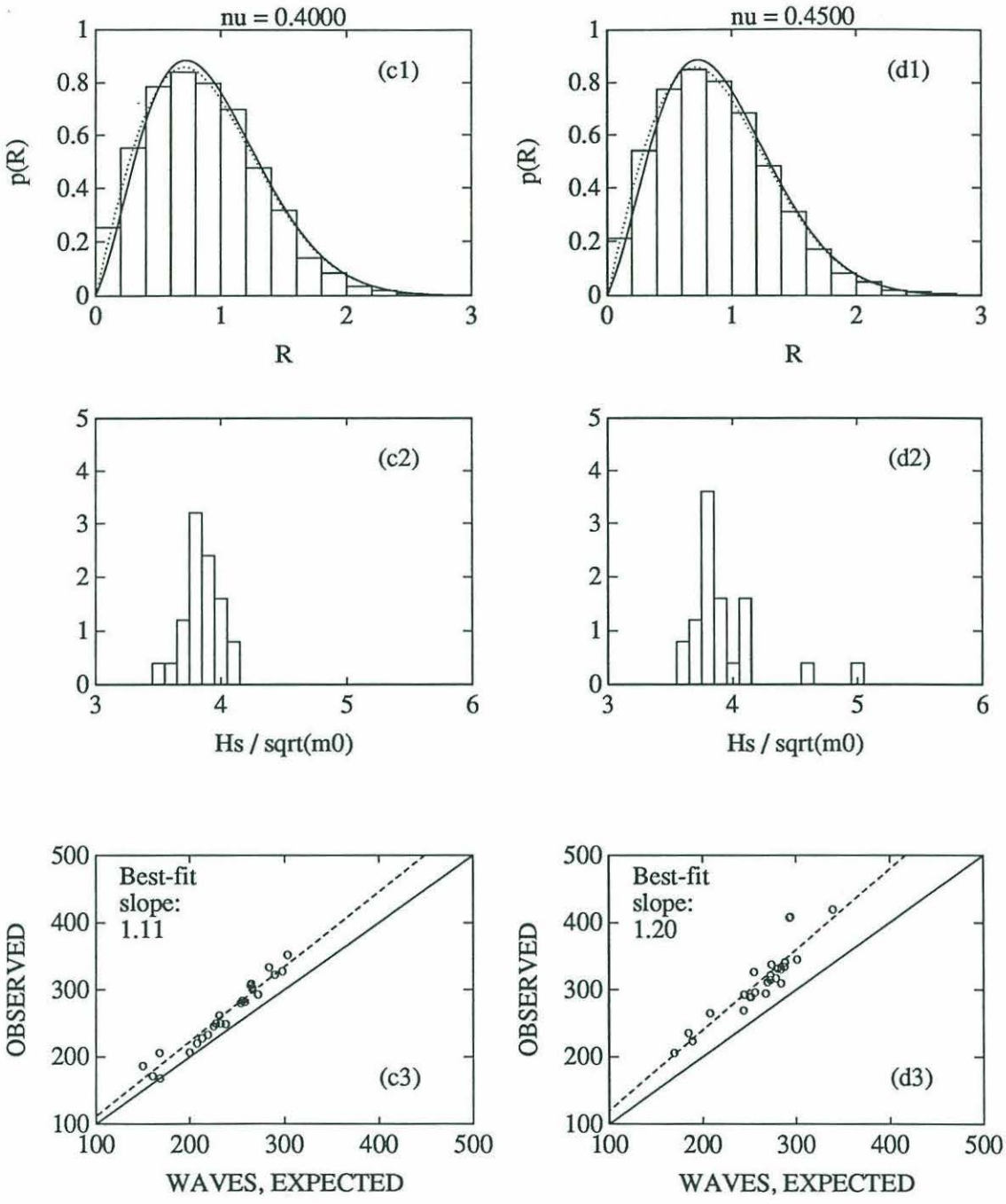

Figure 4-6: (continued). (c) $\bar{\nu} = 0.4000$, (d) $\bar{\nu} = 0.4500$.

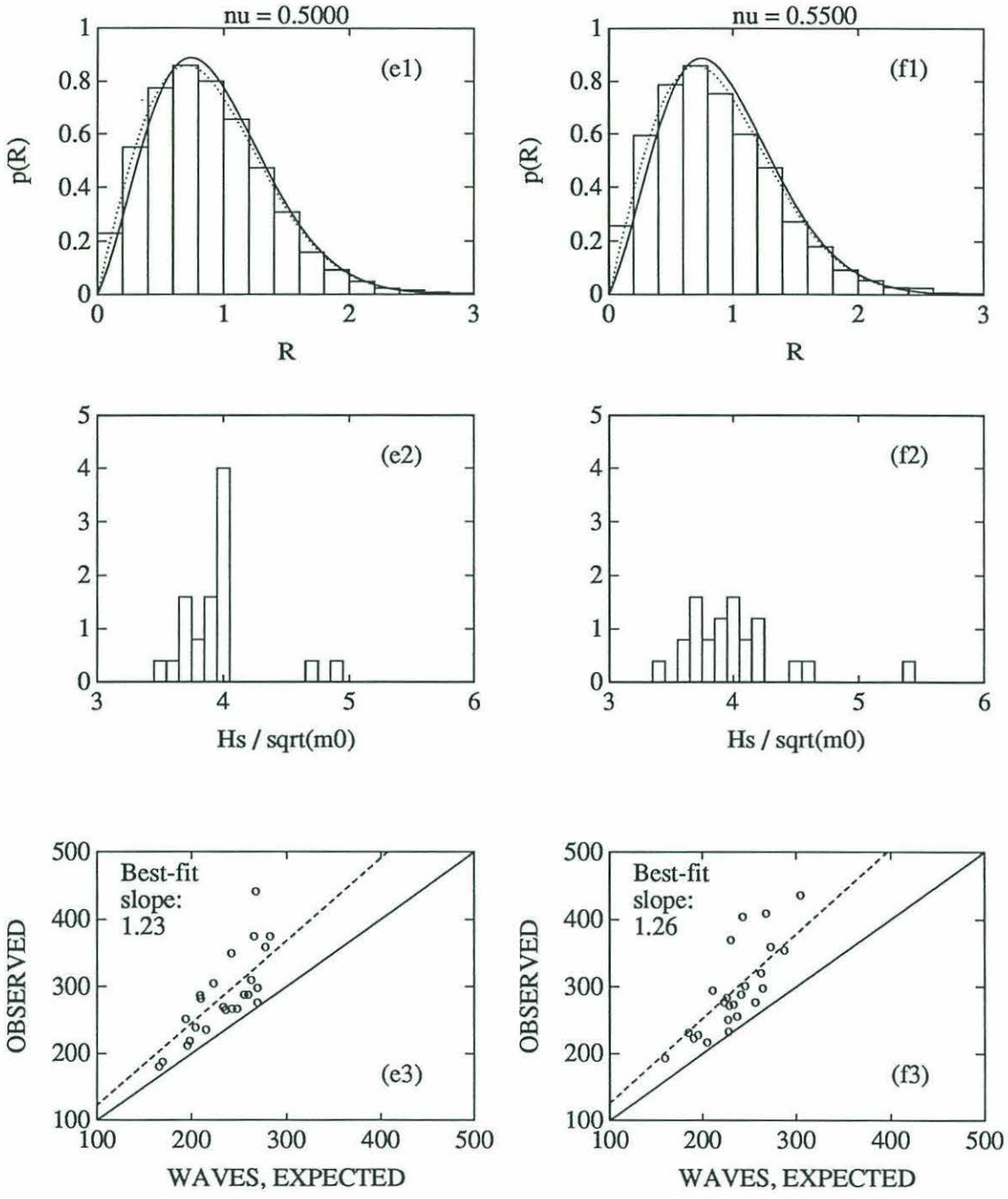

Figure 4-6: (continued). (e) $\bar{\nu} = 0.5000$, (f) $\bar{\nu} = 0.5500$.

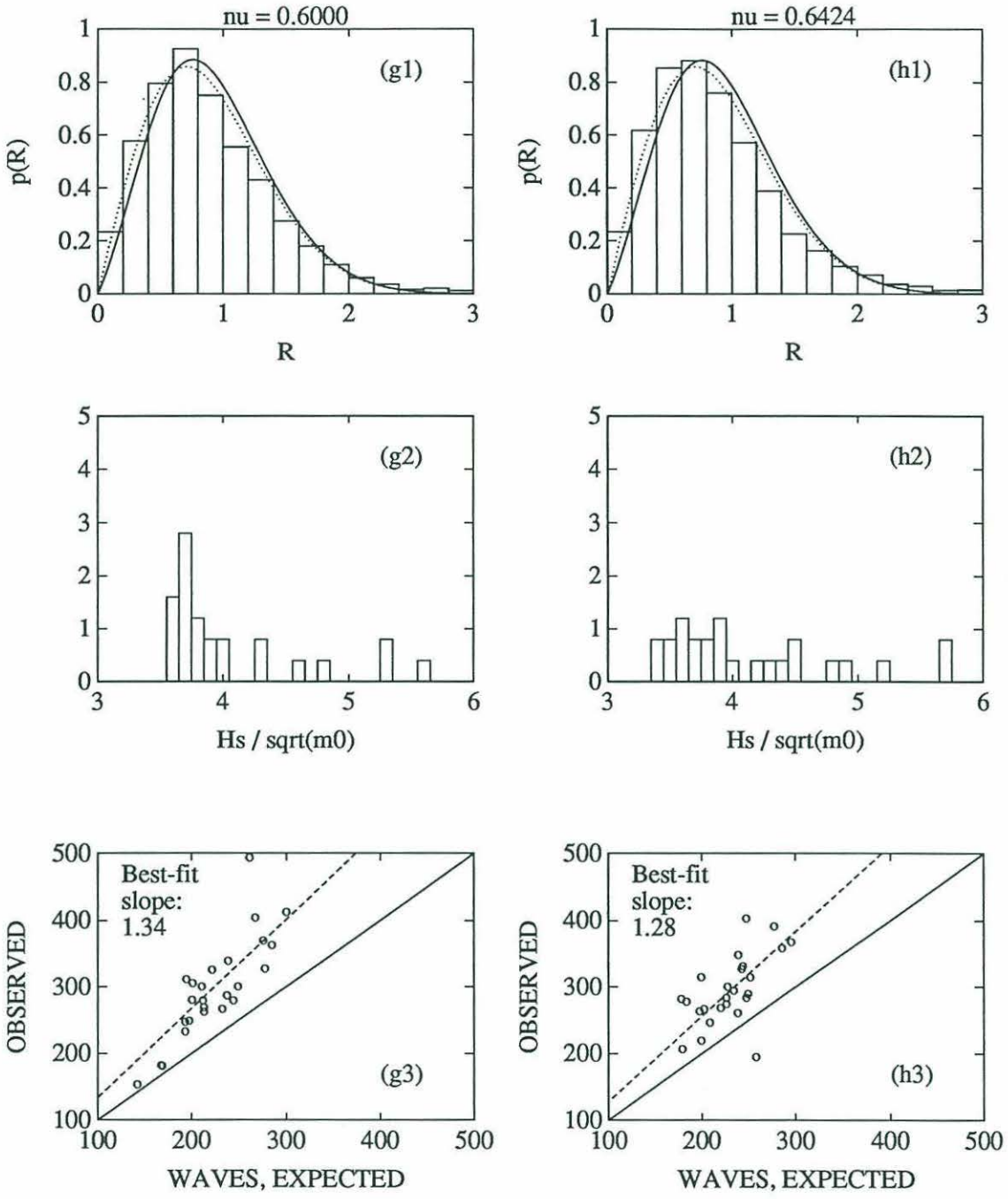

Figure 4-6: (continued). (g) $\bar{\nu} = 0.6000$, (h) $\bar{\nu} = 0.6424$.

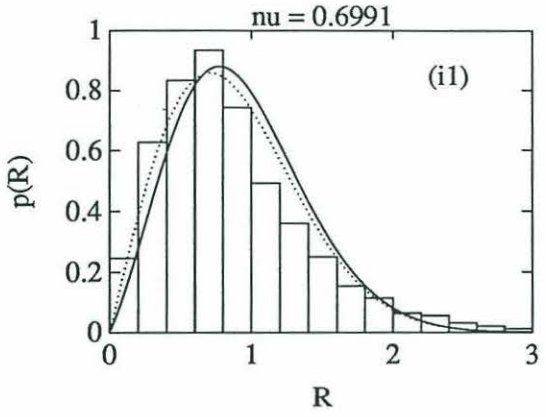

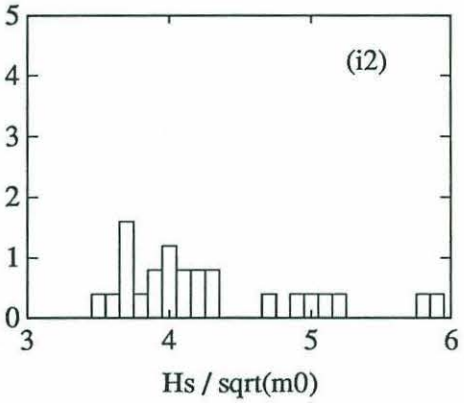

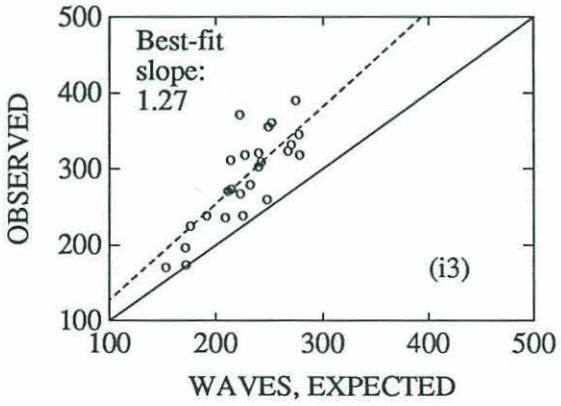

Figure 4-6: (continued). (i) $\bar{\nu} = 0.6991$.

Bimodal Seas

$\bar{\nu}$	Mean of $(H_s/\sqrt{m_0})$	Standard Deviation of $(H_s/\sqrt{m_0})$	Mean of (N_O/N_E)	Standard Deviation of (N_O/N_E)
0.3003	3.870	0.107	1.12	0.040
0.3500	3.903	0.124	1.10	0.041
0.4000	3.840	0.145	1.11	0.057
0.4500	3.926	0.319	1.20	0.077
0.5000	3.942	0.298	1.22	0.155
0.5500	4.003	0.413	1.25	0.168
0.6000	4.067	0.586	1.32	0.188
0.6424	4.141	0.671	1.29	0.187
0.6991	4.287	0.667	1.26	0.150

Table 4.4: Bimodal Seas: Statistics of Significant Wave Height and Number of Waves. Statistics of the ratios $H_s/\sqrt{m_0}$ and N_O/N_E.

Table 4.4 is provided to supplement the significant wave height histograms and plots of N_O versus N_E. It shows the mean of $H_s/\sqrt{m_0}$ increasing with spectral width, a trend predicted by narrow-band theory but not seen in Table 4.2 for unimodal seas. The variance of this ratio also increases with spectral width. For the widest spectra, these ratios are distributed nearly uniformly from 3.5 to 6.0 (see Figure 4-6 [f2–i2]).

Figure 4-7 depicts these trends. The increase in the mean of $H_s/\sqrt{m_0}$ with increasing ν is clearly evident for bimodal seas. This mean remains less than the expected value of $H_s/\sqrt{m_0}$ given by theory for all subgroups except bimodal seas with $\nu \geq 0.6424$.

There are nearly always more waves than expected in a time series. This is consistent with the excess of short period waves. Figure 4-8 shows the mean and standard deviation of the ratio N_O/N_E for unimodal and bimodal seas. The statistics for the two types of seas are nearly identical.

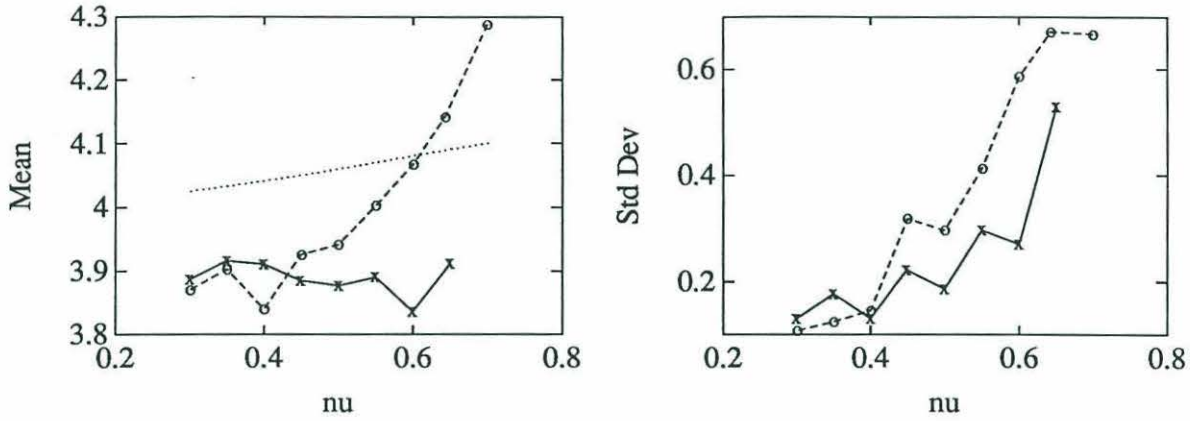

Figure 4-7: Mean and Standard Deviation of $H_s/\sqrt{m_0}$ for Unimodal and Bimodal Seas. Values for unimodal seas are shown by crosses and a solid line. Values for bimodal seas are shown by circles and a dashed line. The expected value of $H_s/\sqrt{m_0}$ is given by the dotted line.

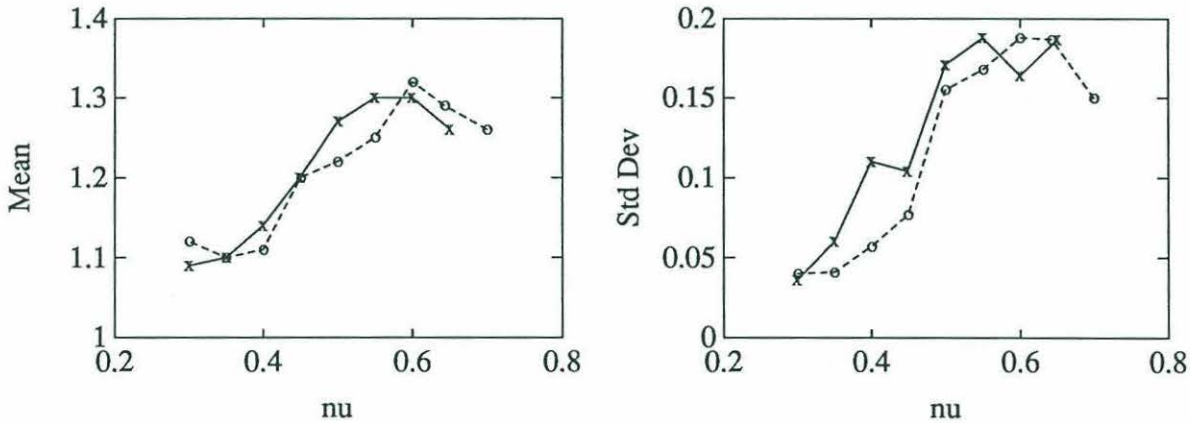

Figure 4-8: Mean and Standard Deviation of N_O/N_E for Unimodal and Bimodal Seas. Values for unimodal seas are shown by crosses and a solid line. Values for bimodal seas are shown by circles and a dashed line.

4.3.3 Distribution of Extreme Wave Heights

Discussion of Results

The plots of Figure 4-9 (a3–i3) show a trend not observed for unimodal seas. For $\nu \geq 0.5500$, the periods of the highest of the extreme waves are considerably less than unity and many are below the lower quartile. The energy ratios, e_r, were checked for a correlation between the dominant peak (the spectral peak with the largest energy) and the period of the extreme wave. As defined by (3.5), e_r gives the ratio of the energy of the high frequency peak to the energy of the low frequency peak. Since a sea with energy only at low frequencies has waves with long periods and a sea with energy only at high frequencies has waves with short periods, it was suspected that a spectrum dominated by a large high-frequency peak would produce an extreme wave with $T_{max} < 1$. The opposite was suspected for spectra where the low-frequency swell peak dominates.

No such correlation is found between the energy ratio and the period of the extreme wave. Forty-two percent of all bimodal seas studied have $T_{max} < 1$. Considering only spectra with $e_r > 1$, 41% of the extreme waves have $T_{max} < 1$. In the subset of bimodal seas with $e_r < 1$, 42% of the extreme waves have $T_{max} < 1$. The period of the extreme wave appears to be independent of e_r.

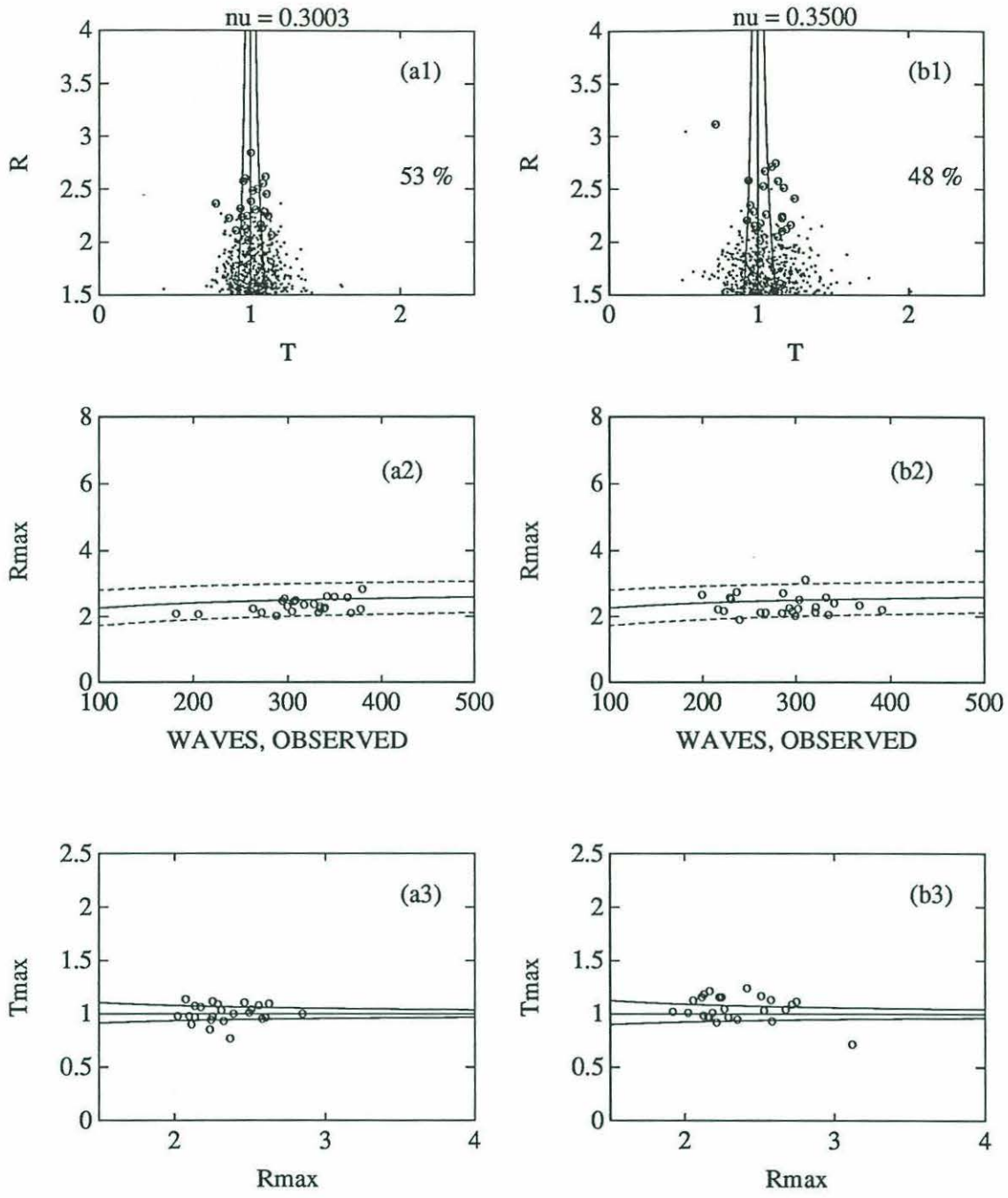

Figure 4-9: Bimodal Seas: Extreme Wave Heights and Periods. Scatter plot for the region where the highest ten percent waves are expected. Quartiles of $p(T|R)$ are superimposed; half the waves should fall between the two outermost quartiles. The number observed in this region is shown as a percentage. The extreme wave from each time series is circled. In the middle plot, the extreme wave height from each time series is plotted as a function of the observed number of waves. The expected value and $\pm 2\sigma$ bounds are shown. The lower plot shows periods of the extreme waves and quartiles of $p(T|R)$. (a) $\bar{\nu} = 0.3003$, (b) $\bar{\nu} = 0.3500$.

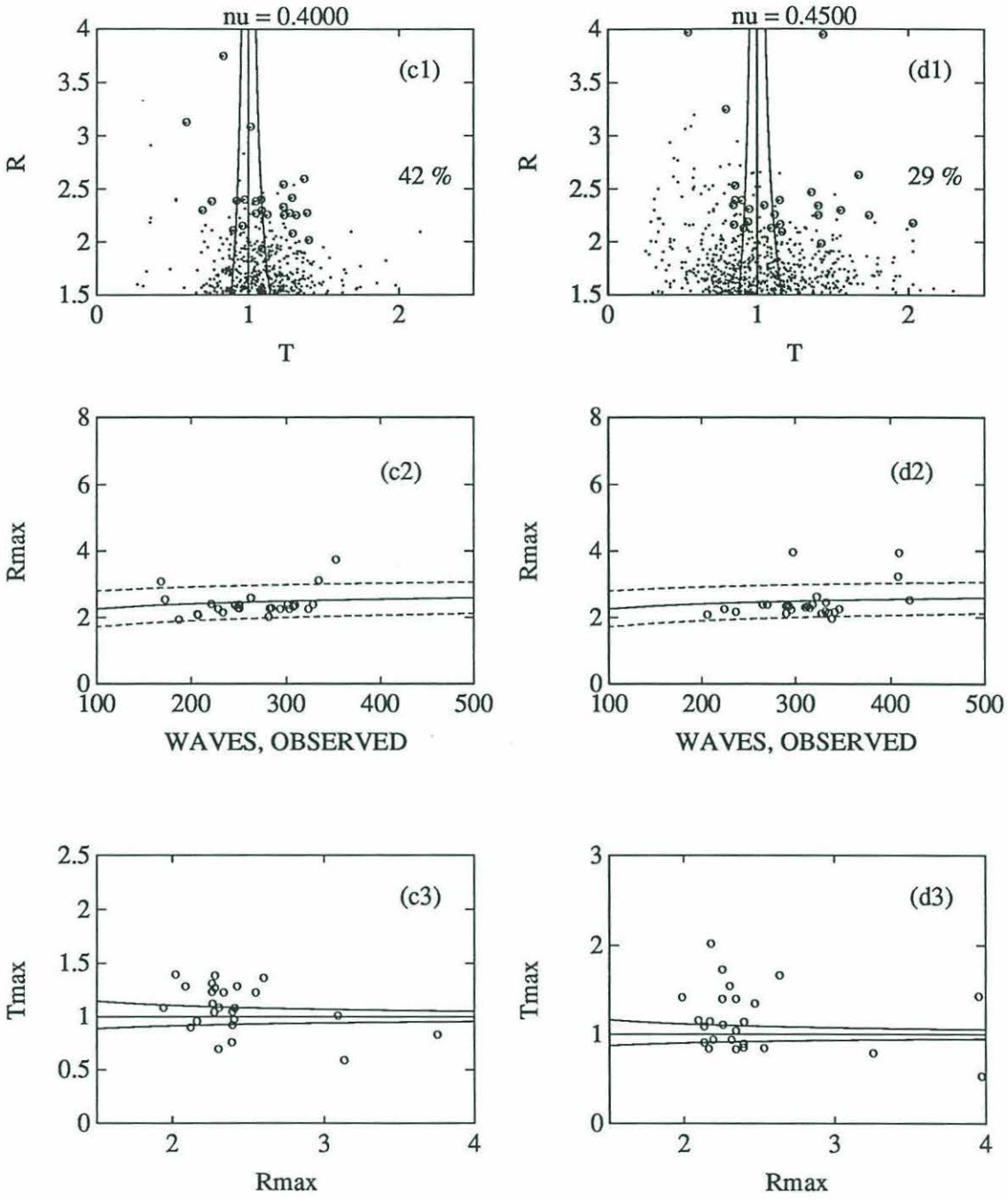

Figure 4-9: (continued). (c) $\bar{\nu} = 0.4000$, (d) $\bar{\nu} = 0.4500$.

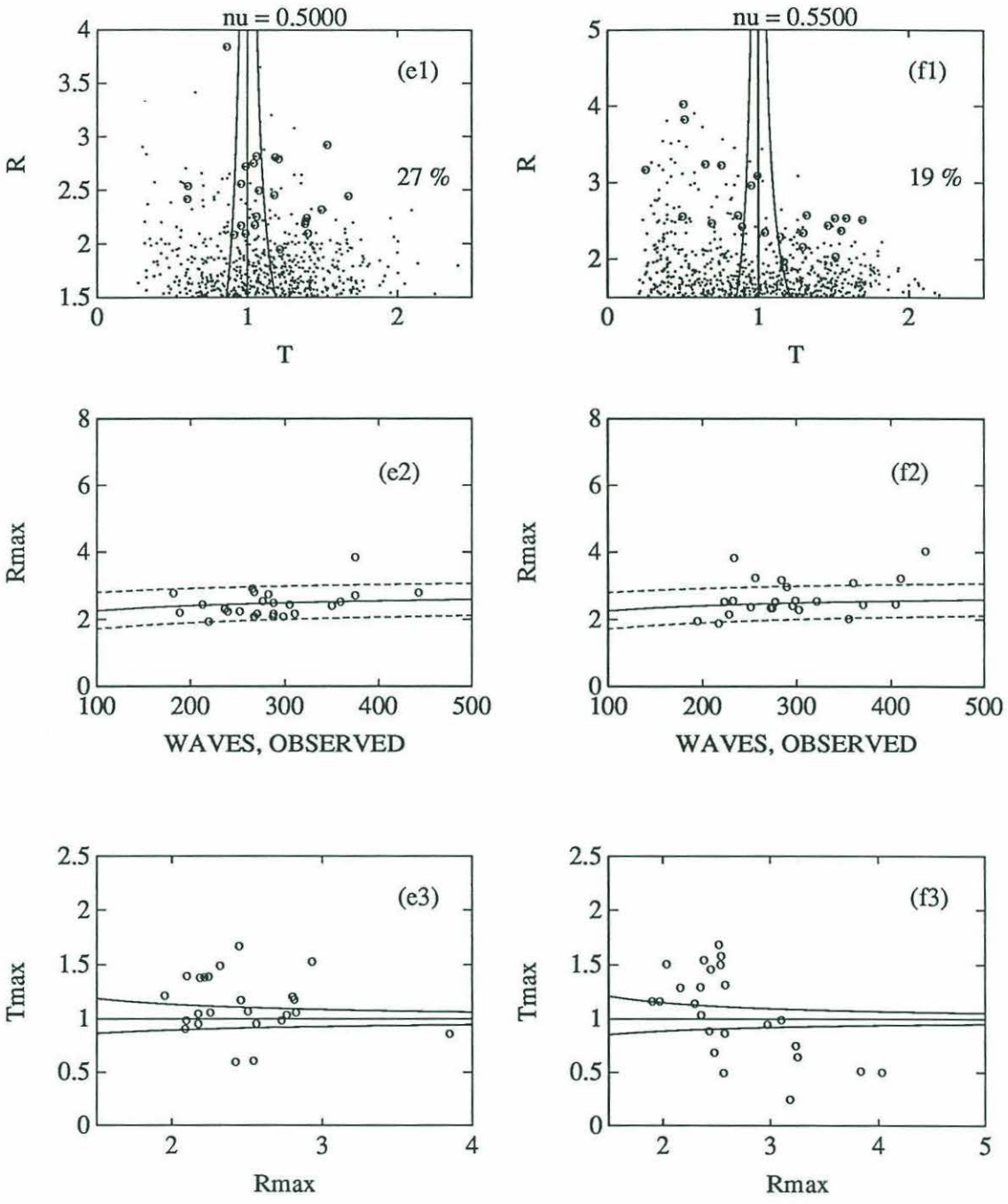

Figure 4-9: (continued). (e) $\bar{\nu} = 0.5000$, (f) $\bar{\nu} = 0.5500$.

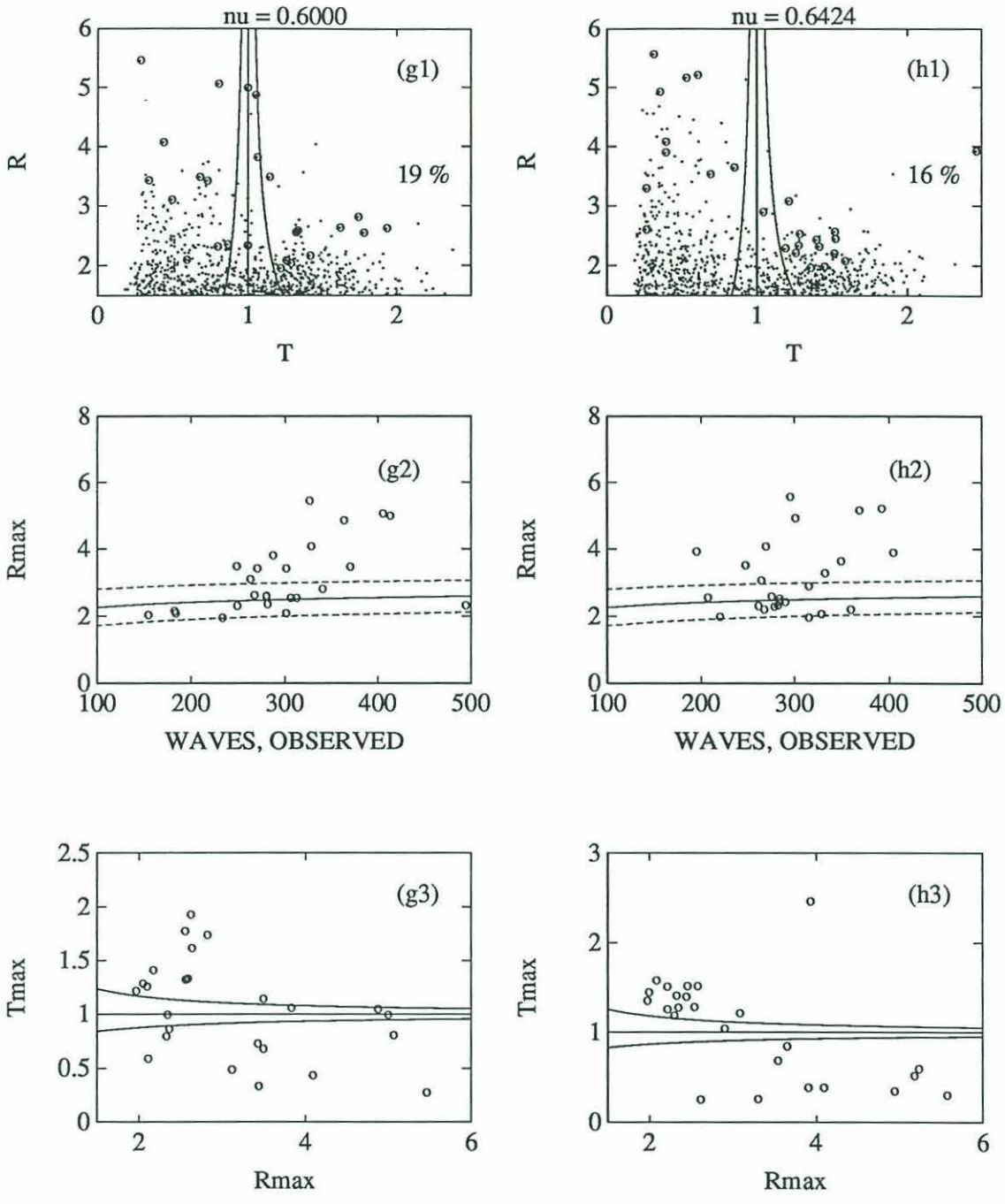

Figure 4-9: (continued). (g) $\bar{\nu} = 0.6000$, (h) $\bar{\nu} = 0.6424$.

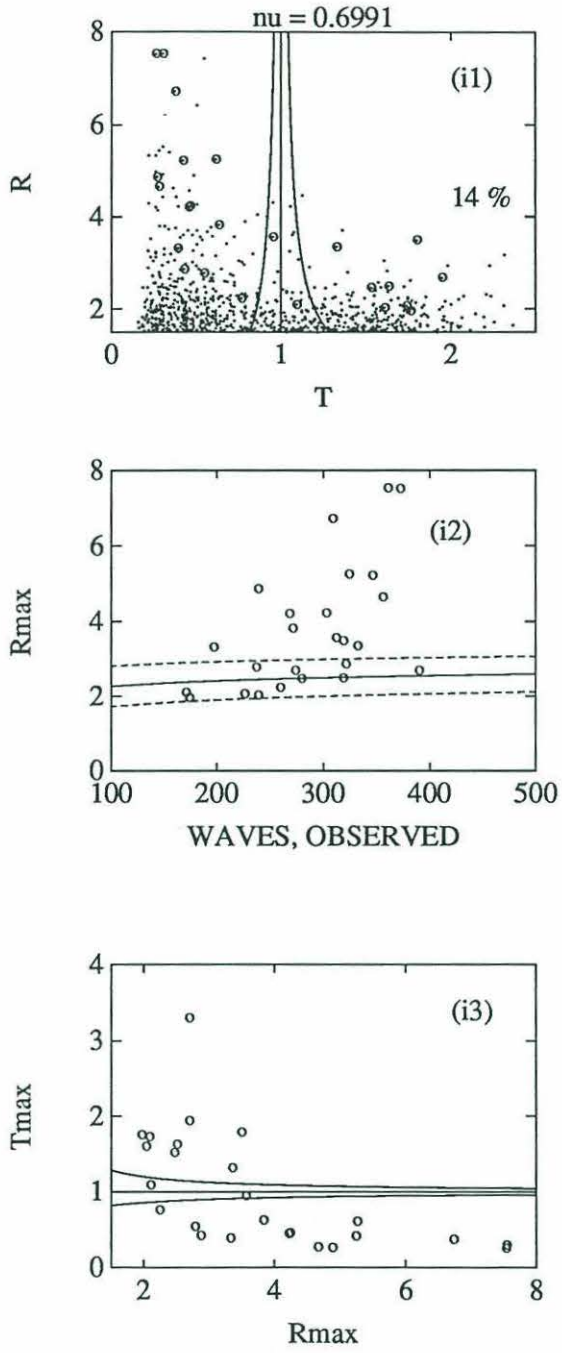

Figure 4-9: (continued). (i) $\bar{\nu} = 0.6991$.

Bimodal Seas

$\bar{\nu}$	Mean of $R_{max}/E(R_{max})$	Standard Deviation of $R_{max}/E(R_{max})$	Mean of T_{max}	Standard Deviation of T_{max}
0.3003	0.927	0.077	1.007	0.087
0.3500	0.937	0.115	1.055	0.118
0.4000	0.974	0.153	1.086	0.220
0.4500	0.978	0.197	1.165	0.352
0.5000	0.992	0.155	1.132	0.271
0.5500	1.059	0.211	1.052	0.404
0.6000	1.250	0.404	1.047	0.454
0.6424	1.266	0.437	1.045	0.556
0.6991	1.508	0.646	0.999	0.757

Table 4.5: Bimodal Seas: Extreme Wave Height and Period Statistics. Statistics of the ratio of extreme wave height to its expected value, $R_{max}/E(R_{max})$, and the period, T_{max}, of the extreme wave.

Table 4.5 is provided to supplement the graphical presentation of extreme wave statistics in Figure 4-9. For each subgroup, the table lists the mean and standard deviation of two quantities, the ratio of extreme wave height to its expected value, and the period of the extreme wave.

The mean value of the extreme wave height is slightly less than expected for spectral widths up to $\bar{\nu} = 0.5000$ as was the case for unimodal seas. Seas from subgroups with wider spectra have larger mean values than expected. The increase in the mean is slightly greater than for unimodal seas. This behavior is consistent with the observed excess of very large waves at high widths.

More pronounced is the variance about the mean. The extreme wave heights for the narrow spectra are well contained by the $\pm 2\sigma$ bounds but the variation increases with spectral width. Figure 4-10 shows this trend for unimodal and bimodal seas. The mean values of $R_{max}/E(R_{max})$ are nearly identical for $\nu \leq 0.5000$. For wider seas, this ratio is greater for bimodal than unimodal seas. The standard deviation of $R_{max}/E(R_{max})$ increases with spectral width and behaves similarly for unimodal and bimodal seas.

The periods of extreme waves behave differently for bimodal seas than for unimodal. The mean of T_{max} does not show an increase with spectral width, as it did for unimodal seas. This results from the appearance of extreme waves with short periods for some bimodal seas with wide spectra. The variation of T_{max} about the mean does increase with

spectral width. This is shown in Figure 4-11.

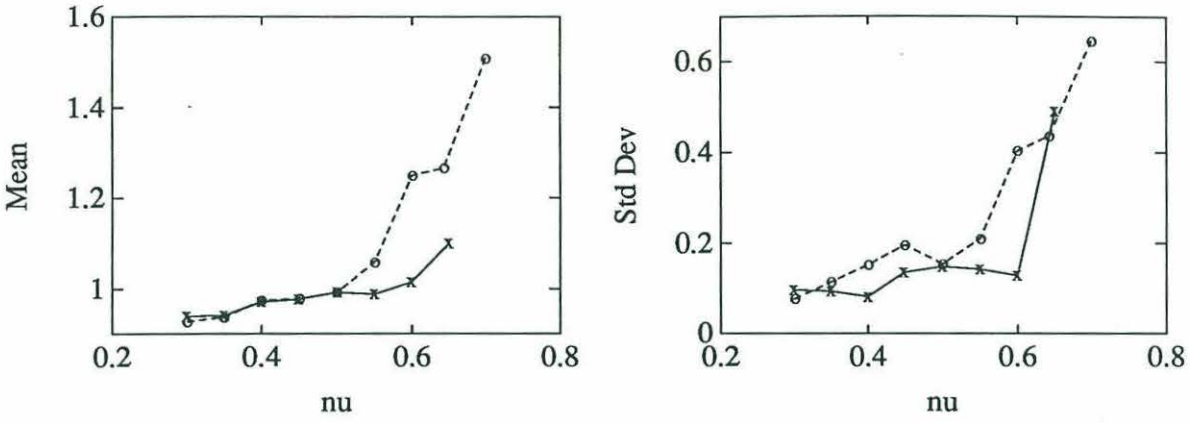

Figure 4-10: Mean and Standard Deviation of $R_{max}/E(R_{max})$ for Unimodal and Bimodal Seas. Values for unimodal seas are shown by crosses and a solid line. Values for bimodal seas are shown by circles and a dashed line.

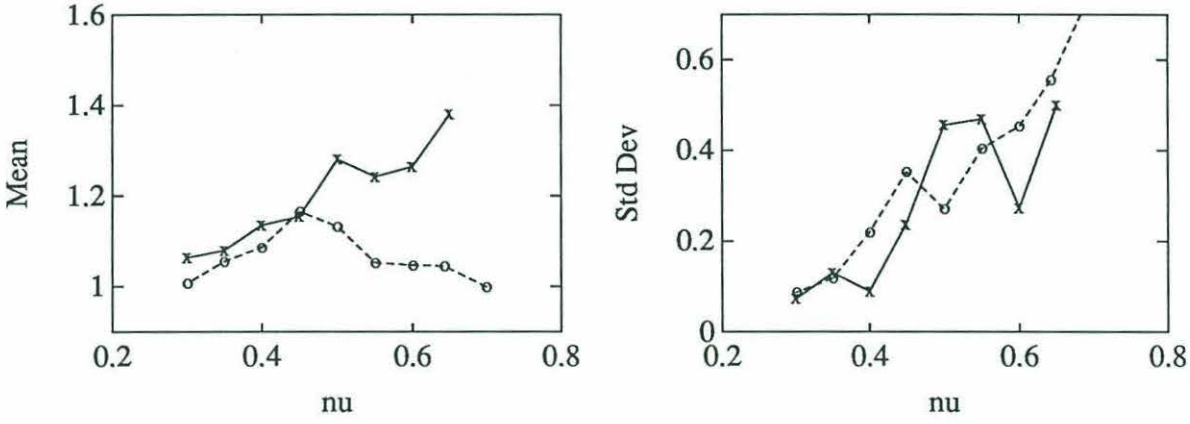

Figure 4-11: Mean and Standard Deviation of T_{max} for Unimodal and Bimodal Seas. Values for unimodal seas are shown by crosses and a solid line. Values for bimodal seas are shown by circles and a dashed line.

Chapter 5

Summary and Conclusions

5.1 Application of Results

The previous chapter compared observed distributions of wave heights and periods to those given by narrow-band theory. The agreement between the theory and data depends strongly on spectral width. Some differences between unimodal and bimodal seas were also noted.

Most of the previous work involved normalized wave heights. Spectra were considered without regard to their energies. One issue to be investigated here is the dependence of spectral shape and width on sea state.

Another issue is the distinction among spectra of different shapes and widths. What do these categorizations allow one to conclude about wave heights and periods?

5.1.1 Spectral Shapes of Storm Seas

The importance of understanding the behavior of seas of different spectral types and widths depends on the application. In one situation, it may be necessary to know the distribution of wave heights and periods associated with the spectrum of any sea condition. In this case, all observed spectral shapes are important.

Alternatively, one may need to know only the distributions for the highest sea states to be encountered during a long period. If the highest seas are always of one spectral shape, understanding the other sea conditions becomes less important.

To investigate the spectral shapes observed during high sea states, spectra are sorted by spectral energy, m_0. The five most severe storms from the twelve month period are listed in Table 5.1. The storms lasted from hours to days and many twenty minute time series were recorded during each one. Each storm is ranked by the highest energy observed during its duration. The spectral shapes and widths associated with each storm are listed. The sea state, spectral type and width, energy ratio and frequency ratio are given for the time series with the greatest energy during each storm.

The highest sea state from the twelve month period has a bimodal spectrum. Both unimodal and bimodal spectra of various widths are observed during each of the five storms. This would seem to indicate that no single shape nor width is uniquely identified with high sea states, however, not all bimodal spectral shapes are equally significant.

The energy and frequency ratios give additional information about the shapes of bimodal spectra associated with the highest sea states. None of the four sets of ratios indicates a bimodal spectrum with peaks that are well separated in frequency and approximately equal in energy. (Spectra with peaks which are sufficiently separated in frequency to remain distinct are observed to have frequency ratios of approximately 3.0 and greater.) The spectra from the highest sea states in storms one and two have peaks which are spaced close together and overlap each other. There are local minima between the peaks, resulting in bimodal classifications, but the overall shapes are very similar to unimodal spectra. The spectra from the highest sea states in storms three and five have high frequency peaks which are much smaller than the low frequency peaks. Again, the resulting spectra are very similar in shape to unimodal spectra.

These observations would indicate that a high sea state is likely to have a unimodal spectrum or a spectrum which is classified as bimodal but is shaped much like a unimodal spectrum, with one peak that is much larger than the other or two overlapping peaks. The storm sea spectrum may be narrow-banded, as in storm 5 where the widest spectrum observed has $\nu = 0.4040$. Narrow-band theory may work well for analysis of this sea. The storm may also have a wide spectrum, as in storm two with widths up to $\nu = 0.5962$. The results from applying narrow-band theory to these seas may not be acceptable.

Storm 1	12–13 February 1988
$4\sqrt{m_0}$	2.55 to 3.75 m
Unimodal Spectral Widths:	$0.3516 \leq \nu \leq 0.5735$
Bimodal Spectral Widths:	$0.3979 \leq \nu \leq 0.5869$
Highest sea state during storm:	$4\sqrt{m_0} = 3.75$m
Spectral type: Bimodal	$\nu = 0.4081$
$e_r = 0.5221$	$f_r = 1.800$

Storm 2	16–17 December 1987
$4\sqrt{m_0}$	2.62 to 3.50 m
Unimodal Spectral Widths:	$0.4451 \leq \nu \leq 0.5848$
Bimodal Spectral Widths:	$0.4971 \leq \nu \leq 0.5962$
Highest sea state during storm:	$4\sqrt{m_0} = 3.50$m
Spectral type: Bimodal	$\nu = 0.5572$
$e_r = 0.5669$	$f_r = 2.276$

Storm 3	18–19 November 1987
$4\sqrt{m_0}$	2.56 to 3.32 m
Unimodal Spectral Widths:	$0.4362 \leq \nu \leq 0.5588$
Bimodal Spectral Widths:	$0.4864 \leq \nu \leq 0.5546$
Highest sea state during storm:	$4\sqrt{m_0} = 3.32$m
Spectral type: Bimodal	$\nu = 0.4864$
$e_r = 0.0741$	$f_r = 2.663$

Storm 4	23 February 1988
$4\sqrt{m_0}$	2.59 to 3.31 m
Unimodal Spectral Widths:	$0.3959 \leq \nu \leq 0.4295$
Bimodal Spectral Widths:	$0.3909 \leq \nu \leq 0.4353$
Highest sea state during storm:	$4\sqrt{m_0} = 3.31$m
Spectral type: Unimodal	$\nu = 0.4155$

Storm 5	28 October 1987
$4\sqrt{m_0}$	2.56 to 3.10 m
Unimodal Spectral Widths:	$0.3515 \leq \nu \leq 0.3820$
Bimodal Spectral Widths:	$0.3345 \leq \nu \leq 0.4040$
Highest sea state during storm:	$4\sqrt{m_0} = 3.10$m
Spectral type: Bimodal	$\nu = 0.3345$
$e_r = 0.0091$	$f_r = 2.711$

Table 5.1: Storm Seas: Wave heights and spectral shapes observed during the five highest sea states during the period September 1987 – August 1988.

5.1.2 Using Spectral Type and Width

Given a sea's energy spectrum, one may need to estimate the significant wave height and the height and period of the extreme wave during a known time interval. It is also necessary to place bounds on the estimates. These estimates and their confidence limits, may be obtained using theoretical distributions given by narrow-band theory.

How should the spectral width be used in this process? As seen in the previous chapter, the simple Rayleigh distribution provides a better description of the marginal distribution of wave heights than does the distribution derived from narrow-band theory which includes a dependence on spectral width. The theoretical distribution of extreme wave heights is nearly independent of spectral width.

A knowledge of width seems most useful not for its inclusion in the theoretical formulations, but for identifying confidence limits for the estimates obtained from narrow-band theory. The information in Tables 4.2, 4.3, 4.4, and 4.5 may be used to correct the expected values of $H_s/\sqrt{m_0}$, R_{max}, and T_{max} and to assign confidence limits. These confidence limits are strongly dependent on spectral type and width. The narrow-band theory is not valid for wide spectra, but if it is used for these spectra, the results tabulated here indicate the errors which may be expected. The following procedure is an example of the way in which these results may be applied.

One may estimate the significant wave height from information in the energy spectrum. The energy of the spectrum can be multiplied by the mean value of $H_s/\sqrt{m_0}$ from Table 4.2 or 4.4 giving an expected H_s appropriate for the spectral type and width used to enter the table. Confidence limits may be placed on the result using the standard deviation of $H_s/\sqrt{m_0}$ from the same table.

Estimating the height of the extreme wave from spectral information is a three step process. First, narrow-band theory (2.135) gives the number of waves to be expected during the time interval of interest. This number is modified using the mean value of the ratio N_O/N_E from Table 4.2 or 4.4. Then, once the number of waves is known, the expected extreme wave height is found from (2.132) then modified and bounded using the mean and standard deviation of $R_{max}/E(R_{max})$ from Table 4.3 or 4.5. Finally, this normalized wave height is converted to a dimensional height using (2.97).

The normalized period of the extreme wave is estimated as the mean of T_{max} from Table 4.3 or 4.5 and confidence limits are based on the standard deviation. The normalized period is converted to a dimensional period using (2.98).

A caution is in order about using the resulting estimates of R_{max} and T_{max} to obtain orbital velocities. These velocities are shown by (2.40) and (2.41) to be fully specified by wave height and period. A designer may wish to know the orbital velocities associated with the extreme wave. Once the expected values and confidence bounds are known for the height and period of the extreme wave, finding the possible velocities seems easy. This will not be the case for bimodal or wide spectra. The orbital velocity equations are derived for a sinusoidal wave and they may not be accurate when the wave height and period are taken from a complicated sea surface.

The procedure outlined above is one possible application suggested by the results of this study. Responsible engineering application of this procedure would require the analysis a much more comprehensive data set than has been examined here.

Bibliography

[1] Briscoe, M. et al. 1988. *Surface-wave data acquisition and dissemination by VHF packet radio and computer networking.* Woods Hole Oceanog. Inst. Tech. Rept. WHOI–88–15. Woods Hole.

[2] Cartwright, D. E. and Longuet-Higgins, M. S. 1956. The statistical distribution of the maxima of a random function. *Proc. Roy. Soc.* A 237 : 212–232.

[3] Chakrabarti, S. K. and Cooley, R. P. 1977. Statistical distributions of periods and heights of ocean waves. *J. Geophys. Res.* 82 : 1363–1368.

[4] Forristall, G. Z. 1978. On the statistical distribution of wave heights in a storm. *J. Geophys. Res.* 80 : 2688–2694.

[5] Hald, A. 1952. *Statistical theory with engineering applications.* New York : John Wiley and Sons.

[6] Little, J. and Shure, L. 1988. *Signal processing toolbox for use with MATLAB.* South Natick : The MathWorks, Inc.

[7] Longuet-Higgins, M. S. 1952. On the statistical distribution of the heights of sea waves. *J. Mar. Res.* 9 : 245–266.

[8] ——. 1975. On the joint distribution of the periods and amplitudes of sea waves. *J. Geophys. Res.* 80 : 2688–2694.

[9] ——. 1983. On the joint distribution of the periods and amplitudes in a random wave field. *Proc. R. Soc. Lond.* A 389 : 241–258.

[10] Nath, J. H. and Yeh, R. 1987. Some time and frequency relations in random waves. *Journal of Waterway, Port, Coastal, and Ocean Engineering.* 113 : 672–683.

[11] Ochi, M. K. and Hubble, E. N. 1976. Six-parameter wave spectra. *Proceedings of the Coastal Engineering Conference.* 1 : 301–328.

[12] Oppenheim, A. V. and Schafer, R. W. 1989. *Discrete-time signal processing.* Englewood Cliffs : Prentice Hall.

[13] Pierson, W. J.; Neuman, G.; and James, R. W. 1955. *Practical methods for observing and forecasting ocean waves by means of wave spectra and statistics.* H.O. Pub. No. 603. U. S. Navy Hydrographic Office.

[14] Press, W. H. et al. 1986. *Numerical recipes.* Cambridge: Cambridge University Press.

[15] Rice, S. O. 1944. Mathematical analysis of random noise. *Bell Syst. Tech. J.* 23 : 282–332.

[16] ——. 1945. Mathematical analysis of random noise. *Bell Syst. Tech. J.* 24 : 46–156.

[17] Sharpe, M. M. and Graber, H. C. 1990. *Wind and wave climatology on the New England shelf, May 1987 – August 1988.* Woods Hole Oceanog. Inst. Tech. Rept. WHOI–90–14. Woods Hole.